Implementation of a Separated Flow Panel Method for Wall Effects on Finite Swept Wings

by

Donald Edwin Robinson

B.S. Aeronautical and Astronautical Engineering
University of Illinois at Urbana-Champaign, 1986

SUBMITTED IN PARTIAL FULFILLMENT OF THE
REQUIREMENTS FOR THE DEGREE OF

Master of Science
in
Aeronautics and Astronautics
at the
Massachusetts Institute of Technology

September 1988

Signature of Author _____
Department of Aeronautics and Astronautics
September 2, 1988

Certified by _____
Professor Judson R. Baron
Thesis Supervisor, Department of Aeronautics and Astronautics

Accepted by _____
Professor Harold Y. Wachman
Chairman, Department Graduate Committee

Implementation of a Separated Flow Panel Method for Wall Effects on Finite Swept Wings

by
Donald Edwin Robinson

Submitted to the Department of Aeronautics and Astronautics, September 2, 1988,
in partial fulfillment of the requirements for the degree of
Master of Science in Aeronautics and Astronautics

ABSTRACT

A separated flow panel method has been implemented for an investigation of wind tunnel wall effects on finite wings. Vortex panels are used to model the wing surface, tunnel surface, and the separated wake region. The solution procedure requires an inner and outer iterative loop. Relaxation of the free vortex sheets comprising the separated wake is conducted during the inner loop. The outer loop is an analysis of the boundary layer to determine separation locations on the wing surface. A wing with $\Lambda_{le} = 45$ degrees, $AR = 3$, $\lambda = 0.25$, and a 64A005 airfoil section was the focus of the investigation because a wind tunnel test of such a wing was also conducted. The wind tunnel test involved acquisition of wing surface pressure distributions for angles of attack between -8 and 14 degrees, and for various leading and trailing edge flap deflections. The experimental wing was relatively large in relation to the tunnel and was expected to have measureable wall effects. The experimental wing had 370 surface pressure taps and, therefore, provided detailed pressure distributions from which separation locations could be determined and lift and drag coefficients calculated. The experiment provided an excellent reference with which to compare results from the panel method and, therefore, most of the cases tested with the panel method were for the wing and approximate tunnel dimensions from the experiment. Comparison of results for the analytical model in free air and in the wind tunnel provide information about the tunnel wall effects present in experimental testing. Additional cases were tested with different tunnel diameters to investigate its effect on wall corrections.

Thesis Supervisor: Dr. Judson R. Baron
Professor of Aeronautics and Astronautics.

To my father,
and to the memory
of my mother

Acknowledgments

This research was carried out as a Center for Aerodynamics Studies project with funding and support provided by the McDonnell Aircraft Company and the Lockheed-Georgia Company.

I would like to thank Frank H. Durgin, the associate director of the Wright Brothers Wind Tunnel, for his guidance in wind tunnel testing techniques as well as his extensive help during the wind tunnel test. I would also like to thank my fellow research assistants at the Wright Brothers Facility for their help; John Burns for providing the base computer program which was implemented for the analytical study of the tunnel wall effects, and Mike DiAngelo for discussions which cleared up confusion about aspects of the analytical model.

I would like to thank Professor E.E. Covert for providing a forum in which I could discuss my research and learn from the discussion of other research topics. His patience while listening to the difficulties I had and for providing insights into possible solutions is appreciated.

I would especially like to thank my advisor, Professor J.R. Baron, for his constant availability and willingness to discuss my work. I appreciate the extent of his time and effort as well as the experimental and theoretical research opportunities he provided for my assistanceship.

Contents

List of Tables

List of Figures

List of Symbols

α	angle of attack
$\alpha_{geometric}$	geometric angle of attack
$\alpha_{corrected}$	angle of attack corrected for $\Delta\alpha_i$
$\Delta\alpha_i$	tunnel wall induced angle of attack
AR	aspect ratio
B	tunnel span
b	wing span
c	local chord
C	tunnel cross-sectional area
C_D	drag coefficient
C_{D_i}	drag coefficient induced by tunnel walls
$C_{D_{fr}}$	friction drag coefficient
C_{D_p}	pressure drag coefficient
$C_{D_{corrected}}$	drag coefficient corrected for wall effects
C_L	lift coefficient
C_{L_f}	lift coefficient in free air
C_{L_t}	lift coefficient in tunnel
C_p	pressure coefficient
$\bar{C}_p$	canonical pressure coefficient
C_{p_i}	pressure coefficient for scanivalve tap i
$(C_{p_i})_c$	corrected pressure coefficient for scanivalve tap i
C_r	wing root chord
δ	tunnel cross-sectional shape factor
δ_{gbf}	ground board flap deflection angle
δ_{le}	wing leading edge flap deflection angle
δ_{te}	wing trailing edge flap deflection angle
E	ground board extension length
η	nondimensionalized span position
F	ground flap length
G	ground board height from tunnel floor
$[I_{\gamma_x}]$	influence matrix for pertubation velocities in x-direction due to vorticity
$[I_{\gamma_y}]$	influence matrix for pertubation velocities in y-direction due to vorticity
$[I_{\gamma_z}]$	influence matrix for pertubation velocities in z-direction due to vorticity
$[I_{\gamma_n}]$	influence matrix for pertubation velocities normal to surface due to vorticity

$[I_{q_x}]$	influence matrix for pertubation velocities in x-direction due to sources
$[I_{q_y}]$	influence matrix for pertubation velocities in y-direction due to sources
$[I_{q_z}]$	influence matrix for pertubation velocities in z-direction due to sources
$[I_{q_n}]$	influence matrix for pertubation velocities normal to surface due to sources
γ	vorticity strength
H	WBF tunnel minor axis
k	pressure tap row number
L	reference length for Re
L_e	extended ground board length
L_o	original ground board length
λ	wing taper ratio
λ	Thwaites' dimensionless pressure gradient
Λ	wing sweep angle
Λ_{le}	wing leading edge sweep anlge
$\Lambda_{1/4}$	wing quarter-chord sweep angle
M	Mach number
$\vec{n}$	normal vector to a surface
nc	number of chordwise panels along chord
ns	number of spanwise panels along semi-span
ν	coefficient of dynamic viscosity
P_i	pressure for scanivalve tap i
P_r	reference pressure for transducers
P_s	tunnel piezo static pressure
P_t	tunnel total pressure
P_{zero}	zero offset of transducer
Φ	velocity potential
ϕ	tunnel paneling angle
φ	perturbation velocity potential
q	source strength
q	dynamic pressure
Q_{Bar}	tunnel dynamic pressure measured on Baratron
$q_{incomp.}$	tunnel dynamic pressure assuming incompressible flow
R	tunnel radius
R	Reynolds number based on $\bar{x}$
R_e	distance for extended ground board from wing trailing edge to ground board flap rotation axis
R_o	distance for original ground board from wing trailing edge to ground board flap rotation axis

Re	Reynolds number
Re_θ	Reynolds number based on momentum thickness
Re_x	Reynolds number based on distance x
ρ	density
S	wing planform area
S_w	wake surface
S_b	body surface
$\vec{t}$	tangential vector to surface
θ	momentum thickness
$\Delta\theta$	rotation angle for panel in wake relaxation
$\vec{u}$	velocity vector
u	velocity in x-direction
u_e	effective two-dimensional velocity
U_∞	freestream velocity
u_m	velocity at peak C_p
v	velocity in y-direction
V_n	velocity normal to surface
ΔV_n	velocity to paneling discontinuity
w	velocity in z-direction
W	WBF tunnel major axis
$\bar{x}$	Stratford's equivalent distance
X_P	distance from wing leading edge to wing pivot
X_A	distance from wing leading edge to aerodynamic center

Subscripts

t	tunnel
f	free air
te	trailing edge
u	upper surface
l	lower surface
sep	separation node

Chapter 1

Introduction

Recently, there has been considerable interest in the analysis of the aerodynamic characteristics of low aspect ratio wings with thin airfoil sections at high lift conditions. Such conditions exist during landing, take-off and maneuver and can be characterized by separation both from trailing edge breakdown and from leading-edge, tip-edge and part-span separation. Advanced theoretical methods have been and are being developed to model the complex flow fields associated with the several types of separation. There is, however, a limited amount of experimental data with which to compare these theoretical methods. Therefore, a wind tunnel test of a half-span wing with an aspect ratio of 3, NACA 64A005 airfoil section, $\Lambda_{le} = 45$ deg., $\lambda = 0.25$, and deflectable leading and trailing edge flaps was conducted to obtain detailed wing surface pressure distributions (370 pressure taps). Unfortunately, due to the thin airfoil section of the wing model and the large number of pressure taps, a relatively large wing model to tunnel size was required. The size of the model thus introduces limits to the angles of attack which may be tested in order to avoid extensive wind tunnel wall effects.

After completing the wind tunnel experiment and analyzing the data, a study of the wind tunnel wall effects on the wing model was conducted with a potential flow/viscous/wake iterative vortex panel method. Because, as expected, extensive separation occurred on the wing model during the wind tunnel test, an accurate analysis of the wall effects required the modeling of separation over a low aspect ratio wing within

a wind tunnel environment. Analysis of the wall effects was performed in order to obtain an estimate of the angle of attack limits to which the wing model could be tested. The wall effects are clearly a function of the relative size of the model to tunnel (b/B), so in addition to modeling the specific wind tunnel test which was performed, effort was directed toward determining the sensitivity of the wall effects to that ratio. The objectives were to provide information on angle of attack and model scale constraints for wing testing with and without separation for relatively large models.

The potential flow/viscous/wake iterative vortex panel method used for this analysis illustrates the increasing ability of panel methods to model complex aerodynamic flows. Since the poineering work of Hess and Smith [9], in the mid 1960's, panel methods have been used to compute the aerodynamic characteristics of aircraft configurations. The early panel methods, however, were limited to the analysis of fully attached flows and thus could not be applied to wings or airfoils at higher angles of attack where separation is a dominant flow characteristic. Dvorak and Maskew [4], in the mid 1970's, developed a two-dimensional panel method that calculated the flow about airfoils up to and beyond stall. Henderson [8] and later Gilmer and Bristow [7] developed similar panel methods with similar capabilities. In order to model separation, these methods model the separated wake and determine the separation location on the airfoil using a viscous boundary analysis. Although finite wings involve three-dimensional boundary layers and more complex separated wakes, Dvorak etal [5] showed the feasibility of the extension of his earlier work [4] to these flow conditions, and was thus the basis for the separated flow model used in this analysis.

Panel methods have also been developed for the evaluation of subsonic wall interference ([11], [15]) by simulating the presence of wind tunnel walls with panels. Burns [1] combined the tunnel and separated flow models and developed a panel method for wall

effects on finite wings with separation. Although the structure of the code was already complete, substantial effort and modification was required to improve its capabilities for the analysis. Since the wind tunnel test was completed prior to the implementation of the analytical model to the study of wall effects, the experimental results provided an excellent data base with which to compare results from the vortex panel method.

Chapter 2

Experiment

2.1 Introduction

A low speed wind tunnel test of a 45 degree leading edge sweep wing with an aspect ratio of 3.0 was conducted at the Wright Brothers Facility (WBF) in early June 1987. The wing was one of three semi-span wings of thin airfoil section (NACA 64A005), different leading edge sweep angles (25, 45, and 65 degrees), and deflectable leading edge and trailing edge flaps. These wing models make up the McDonnell Aircraft Company's (MCAIR) Generic Fighter Research Wing Model system. The test reported here included only the 45 degree leading edge sweep wing. The model semi-span wing, component parts, and support mount were furnished by the McDonnell Aircraft Company. The wing assembly configuration was completed with the addition of a reflecting plane ground board designed and furnished by the WBF.

Acquisition of surface pressure distributions for various wing attitudes and flap deflections was the primary data objective. Pressure coefficients at the wing surface were obtained for the geometric angle of attack range between -8 and 14 degrees. The pressure coefficients were obtained at the following two nominal conditions: a) Reynolds number of 1.0 million/ft and Mach number of 0.15; b) Reynolds number of 1.3 million/ft and Mach number of 0.19. Such conditions correspond to nominal wind tunnel velocities of 160 fps and 213 fps respectively. In addition to pressure coefficient data,

global lift and drag coefficients, spanwise lift coefficient distributions, and local section lift coefficients were obtained from discrete integrations of pressure coefficients over the wing surface.

Before beginning the primary data acquisition, various reflecting plane configurations were tested. Coefficients of pressure on the upper surface of the ground board were determined. From comparisons of the pressure distributions on the ground board for various reflecting plane configurations and wing angles of attack, a ground board configuration for testing the wing was determined. This "best configuration" was then used for all surface pressure data acquisitions.

2.2 Generic Fighter Research Wing Model

Figure 2.1 illustrates the 45 degree sweep wing configuration. The wing model has a NACA 64A005 airfoil section (root to tip) defined in the streamwise direction, a 0.25 taper ratio, 48 in. semi-span, 51.2 in. root chord, 1536 sq.in. half-planform area, and a 3.0 aspect ratio. The model has deflectable 20% chord inboard and outboard leading edge flaps and 25% chord inboard and outboard trailing edge flaps. Both the leading edge flaps and trailing edge flaps extend from the wing root to 75% of the wing semi-span. Flap brackets permit leading edge flap deflections of 0, 10, and 20 degrees and trailing edge flap deflections of 0, 10, and 30 degrees.

The surface of the model has 370 static pressure taps with which to measure surface pressure distributions. Figure 2.2 illustrates the wing axis system used to define wing surface location. Figures 2.3 and 2.4 illustrate the distribution of pressure taps on the wing surface. These taps are arranged in 10 chordwise rows on the upper and lower

surfaces. The spanwise distribution of tap rows is given by

$$\bar{y} = \frac{y}{(b/2)} = 0.05 + 0.95\cos(\frac{10-k}{20}) \qquad (k = 0, 1, \ldots, 9) \tag{2.1}$$

where k (row no. - 1) is defined in Figures 2.3 and 2.4. Each tap row includes a leading edge tap, 24 upper surface taps, and 12 lower surface taps. Chordwise tap numbers 1 through 24 are on the wing upper surface while chordwise tap numbers 25 through 36 are on the wing lower surface. Table 2.1 lists the x'/c locations for the wing surface pressure taps.

2.3 Model Installation In Wind Tunnel

The MIT Wright Brothers Low Speed Wind Tunnel has a closed return circuit. The test section has an elliptic cross section 7.5 x 10.0 feet and is 15 feet long. The tunnel currently is capable of producing wind velocities from 0 - 235 fps for tests at atmospheric pressure. Figure 2.5 is a schematic diagram of the WBF.

The model was mounted vertically from the test section floor and on a turntable which allows for rotation of the wing to various angles of attack. Since the model consists of a semi-span wing, a ground (reflecting plane) board was constructed to simulate the symmetric induced effects that the opposing semi-span would have on the model. Figure 2.6 illustrates the ground board and wing installation. The upper surface of the ground board was located 20.5" (G/H = 0.23) below the centerline of the tunnel and level with the wing root chord. The top of wind tunnel is located 65.5" (B/2H = 0.73) above the upper surface of the ground board. The wing spans 73% (b/B = 0.73) of the vertical distance from the upper surface of the ground board to the top of the wind tunnel. Because the ground board was 4" thick, the most forward 8.5" of the ground board were designed as a half ellipse.

Three 18" ($F/C_r = 0.35$) long ground board flaps were attached at the trailing edge of the ground board. They were capable of deflections upward which induced changes of the air flow and attempted to make the finite ground board appear to the flow as an infinite reflecting plane. The original ground board was designed to be of length $L_o/C_r = 2.56$ with a distance from wing trailing edge to ground board flap rotation axis of $R_o/C_r = 0.62$. Because of concerns that deflection of the ground board flaps would induce a pressure gradient upstream, it was decided to build a downstream extension for the ground board of length $E/C_r = 0.94$. It was argued that positioning the flaps farther downstream, would subject the wing to less of a pressure gradient due to the ground board flap deflections. With the extension, $L_e/C_r = 3.50$ and the rotation axis of the ground board flaps was at a distance of $R_e/C_r = 1.56$ downstream of the wing trailing edge.

The ground board had three rows of static pressure taps along its length. These taps provided data from which the pressure distribution along the test section could be determined. Figure 2.7 shows the distribution of the pressure taps on the ground board and Table 2.2 lists the locations.

2.4 Test Procedure

The test of the wing model was performed in two distinct phases. The first consisted of a test of various ground board configurations. From analysis of the results of these tests, the actual configuration for the second phase was determined. The second phase included the acquisition of surface pressure distributions for various wing attitudes and flap configurations.

During the first phase, the four ground board configurations listed below were tested.

g.b.	$(length/C_r)$	g.b. flap deflection angle (deg)
short	2.56	0
short	2.56	10
long	3.50	0
long	3.50	10

In this first phase, the wing was tested without leading or trailing edge flap deflections. The tests were conducted at a nominal Reynolds number of 1.0 million/ft, a nominal Mach number of 0.15, and at geometric angles of attack of 0, 8, and 14 degrees. The pressure distributions on the ground board for these ground board configurations and wing angles of attack were examined to determine the "optimum" configuration for the purposes of the second phase. Although the primary purpose of the ground board runs was to obtain ground board surface pressure distributions, only 2 scanivalves were required for that objective. Therefore, 75% of the wing surface pressures were also measured.

An ideal reflecting plane would extend upstream and downstream to infinity. This was not possible in the limited confines of the wind tunnel. Therefore, ground board flap deflections were made in an attempt to simulate an infinite reflecting plane. With the short ground board ($L_o/C_r = 2.56$), the deflection of the ground board flaps increased the pressures at the wing trailing edge (see figures 2.8 and 2.9) This would be expected to affect the separation and other flow characteristics of the wing. With the long ground board ($L_e/C_r = 3.50$), the deflection of the flaps did not have an appreciable effect on ground board surface pressures at the wing, but it did produce changes in the ground board surface pressures in the wing wake region (see figures 2.10 and 2.11). Because of the increased pressures upstream caused by ground board flap deflections and the uncertainty of their effect on the flow, the second phase was conducted without ground

board flap deflections.

The ground board extended $0.58C_r$ upstream of the wing leading edge for both the long and short ground board. The trailing edge of the short ground board was $0.97C_r$ downstream of the wing trailing edge. The trailing edge of the long ground board was $1.91C_r$ downstream of the wing trailing edge. Figures 2.12 and 2.13 are plots of pressure coefficient distributions on the ground board surface for the short and long ground boards with the wing at 14 degrees angle of attack. The differences between the distributions prompted the selection of the long ground board for the second phase. The differences between the ground board surface pressures for the two ground board lengths could be due to differences in interactions of the wing wake and the flow from beneath the ground board. The interaction of the wing wake and the flow from beneath the ground board would be expected to vary with the downstream location of the interaction. Because the momentum in the wing wake was small, pressure disturbances due to the interaction could propagate upstream and affect the wing surface pressures, and therefore, it was conjectured that the longer ground board would reduce this effect.

As stated previously, the second phase of the test consisted of the acquisition of surface pressure distributions for various wing attitudes and flap deflections. Wing surface pressure distributions were measured for geometric angles of attack of -8, -4, 0, 2, 4, 6, 8, 10, and 14 degrees for each wing configuration. A wing configuration consisted of a specific leading edge and trailing edge flap deflection combination. The seven different configurations examined are listed below.

l.e. flap deflection (deg)	t.e. flap deflection (deg)
0	0
10	0
10	10
0	10
0	30
20	30
20	0

For the second phase, each configuration was tested at a nominal Reynolds number of 1.0 million/ft and a nominal Mach number of 0.15. A 0.1 in. wide boundary layer trip of No. 120 grit was positioned at the 5% chord location for all configurations.

Additional tests of the 0-0 and 20-30 wing configurations were conducted to examine the effects of Reynolds number and boundary layer trip on the wing surface pressures. Both configurations were tested, with and without boundary layer trips, at a nominal Reynolds number of 1.3 million/ft and a nominal Mach number of 0.19. These two configurations were also tested, without a boundary layer trip, at a nominal Reynolds number of 1.0 million/ft and a nominal Mach number of 0.15.

2.5 Data Acquisition

Quantities measured included tunnel dynamic pressure, tunnel static pressure, tunnel total temperature, and ground board or wing surface pressures. Data acquisition was controlled using a DEC PDP 11/23. Eleven channels of data were used to obtain the measured quantities. Eight channels were required for wing and/or ground board

surface pressures. Total temperature, static pressure, and dynamic pressure each required one channel. Measured data was converted from analog to digital during the data acquisition. Each quantity was determined by averaging 5 seconds of data samples at a sampling rate of 100 samples/second.

A preliminary reduction of data was completed before the acquired data was stored. This consisted of the determination of pressure coefficients from measured differential pressures and the calculation of Reynolds number and Mach number from isentropic flow relations.

Pressure data was acquired using nine differential transducers that measured the difference between an applied pressure and a reference pressure. The reference pressure for all transducers was the average static pressure at the vertical cross plane of the model. This average static pressure was obtained from a piezo static pressure system which averaged the static pressures from two ports which were located in the vertical plane of the model and on opposite tunnel walls. (see figure 2.6)

An MKS 398 series Baratron Differential Pressure Transducer, located outside the wind tunnel, was used to measure the tunnel dynamic pressure.

$$Q_{Bar} = P_t - P_r \tag{2.2}$$

This measurement was made by measuring the difference between the tunnel total pressure (obtained from a total head probe located just upstream of the test section) and the reference piezo static pressure. The other eight pressure transducers were Druck model PDCR 22 differential transducers and were each located in one of the eight scanivalves mounted within the ground board. The reference pressure for these transducers was piezo static pressure. Wing surface pressures and/or ground board surface pressures were applied to the active side of the transducer by the scanivalves. Each scanivalve

unit has 48 input taps for applied pressures. The dynamic pressure, static pressure, and total pressure were measured each time the group of eight scanivalve taps were set to a specific scanivalve tap number.

Tap 48 applied tunnel piezo static pressure to the transducer and thus measured the zero pressure offset of the transducer. An initial transducer pressure offset was read before the pressure data was measured and was used to correct measured pressures during the data acquisition.

$$P_{zero} = P_s - P_r \tag{2.3}$$

Tap 1 applied tunnel total pressure to the transducer and thus measured the tunnel dynamic pressure. The reading of tunnel dynamic pressure on tap 1 served as a check on the gains used to reduce the data. This tap should have a pressure coefficient of unity.

$$C_{p_1} = \frac{(P_t - P_r) - P_{zero}}{Q_{Bar}} \tag{2.4}$$

The remaining 46 taps were used to apply either wing surface pressures or ground board surface pressures to the transducer.

$$C_{p_i} = \frac{(P_i - P_r) - P_{zero}}{Q_{Bar}} \qquad (i = 2, 3, \ldots, 47) \tag{2.5}$$

A final transducer offset was read on tap 48 after the pressure acquisition was completed. A coefficient of pressure for tap 48 was determined and used in the data reduction to correct the coefficients of pressure for shift in the zero offset.

$$C_{p_{48}} = \frac{(P_s - P_r) - P_{zero}}{Q_{Bar}} \tag{2.6}$$

If the zero pressure offset of the transducer did not shift during the time interval for data acquisition, $C_{p_{48}}$ should equal 0.0. This serves as both a check and a basis for corrections.

2.6 Data Reduction

Overall, the reduction of the pressure coefficient data included corrections for zero shifts in the transducers over the duration of each run, for transducer calibration uncertainties, and for compressibility, as well as the removal of bad data points which resulted from leaky and/or plugged pressure taps.

The duration of the data acquisition period for a single run was approximately 15 minutes. During this time, the tunnel temperature tended to increase several degrees. On a few occasions the temperature decreased because the dynamic pressure was lowered from 50 psf to 30 psf from one run to the next. In either case, the transducer zero was sensitive to temperature variations. In fact, the variation of the transducer zero with temperature was approximately linear. At the beginning of each run the zero of the transducer was measured. All subsequent data measured on that transducer was corrected for the zero offset of the transducer. At the end of each data run the shift in the transducer zero was measured. Assuming that each of the 48 scanivalve taps was read an equal increment of time apart, and that the zero shift was linear over the total time period, each of the data points was corrected using a linear variation of transducer zero with time.

$$(C_{p_i})_c'' = C_{p_i} - \frac{i}{48} C_{p_{48}} \qquad (i = 1, 2, \ldots, 47) \tag{2.7}$$

Each transducer was calibrated and a constant was determined which was used to convert voltages to engineering units. Although these calibrations were carefully performed, there are always uncertainties. Since tap 1 reads dynamic pressure and C_{p_1} is calculated by dividing the dynamic pressure determined from tap 1 by the the dynamic pressure determined from the Baratron, minor corrections can be made to the data obtained

from each scanivalve transducer by requiring that the corrected C_{p_1} equals 1.0.

$$(C_{p_i})'_c = \frac{(C_{p_i})''_c}{C_{p_1}} \qquad (i = 1, 2, \ldots, 47) \tag{2.8}$$

The dynamic pressure used to calculate the pressure coefficients was obtained first from the difference between total pressure and static pressure by assuming that the flow in the wind tunnel was incompressible. Although the Mach numbers at which the wing was tested were small, the flow was not incompressible. The actual dynamic pressure was obtained from isentropic flow relations and was used to reduce the coefficients of pressure.

$$q_{incomp.} = Q_{Bar} = P_t - P_s \tag{2.9}$$

$$q = 0.7(P_s)M^2 \tag{2.10}$$

$$(C_{p_i})_c = \frac{q_{incomp.}}{q}(C_{p_i})'_c \qquad (i = 1, 2, \ldots, 47) \tag{2.11}$$

Because of the possibility of blocked tubes or pressure leaks occuring due to model changes, the taps involved in each model change were checked before the new wing configuration was tested. A constant pressure source was used as the applied pressure at the wing surface tap. This allowed for the determination of both incorrect connections and leaky or plugged taps. Because of the difficulties and time required, it was not feasible to make all the pressure taps functional after each model change. An average of 3.6% of the taps were inoperable during the test with 5.7% being the maximum for any one model configuration.

2.7 Results

2.7.1 Tunnel Wall Corrections

A model tested in a wind tunnel will not perform in exactly the same way as a model in free air. Reference [18] discusses the errors and corrections involved in wind tunnel studies. The presence of the tunnel walls constrains the air flow relative to that for free air and therefore induces errors due to buoyancy, solid and wake blockages, and tunnel wall induced angle of attack.

The buoyancy acting on the model is the force due to a pressure gradient along the test section. "Horizontal buoyancy" is usually insignificant for wings [18] and therefore no correction for buoyancy was performed.

Solid blockage of the tunnel due to the model itself produces a reduced tunnel cross-sectional area and hence an increased velocity at the model relative to what should exist for the corresponding upstream and downstream test section velocities. Wing wake blockage also produces a reduced tunnel cross-sectional area and hence affects tunnel velocities. For this test total pressure was measured just upstream of the test section. An average static pressure was measured at the vertical cross plane of the model by the use of two piezo static ports in the tunnel walls (see figure 2.6). Flow in the test section is assumed isentropic and therefore the total pressure is assumed constant in the test section. Since the average static pressure in the vertical plane of the model was obtained, the measured dynamic pressure and velocity were average values for the vertical plane of the model and therefore no solid or wake blockage correction was performed.

According to the classical tunnel wall corrections for angle of attack as presented in reference [18], tunnel walls induce an angle of attack on the wing model which is

proportional to C_L.

$$\alpha_{corrected} = \alpha_{geometric} + \Delta\alpha_i \tag{2.12}$$

$$\Delta\alpha_i = \delta(\frac{S}{C})C_L \quad radians \tag{2.13}$$

$$C_{D_{corrected}} = C_D + C_{D_i} \tag{2.14}$$

$$C_{D_i} = \Delta\alpha_i C_L \tag{2.15}$$

If the cross-section of the tunnel above the reflecting is approximated by a semi-circle of radius R = 65.5" (see figure 2.14), $\delta = 0.125$ as determined in reference [18]. S and C represent wing planform area and tunnel cross-sectional area respectively. For S = 3072 sq.in. and $C = \pi R^2$, the ratio of S/C = 0.228 and the tunnel induced angle of attack and tunnel induced drag are as follows:

$$\Delta\alpha_i = 1.63C_L \quad degrees \tag{2.16}$$

$$C_{D_i} = 0.029C_L^2 \tag{2.17}$$

Although this method is for unswept wings, reference [18] states that when the aerodynamic center of the swept wing and the pivot point for angle of attack coincide and are near the tunnel centerline, the difference between the angle of attack induced by the tunnel walls for the swept wing and unswept wing is small. Reference [16] states that for a linearly tapered wing the location of the aerodynamic center is found from the following equation:

$$X_A = \frac{1+2}{1+\lambda}(\frac{1}{3})\frac{b}{2}\tan(\Lambda_{\frac{1}{4}}) \tag{2.18}$$

where X_A represents the distance distance aft from the quarter chord of the root section to the wing aerodynamic center. The pivot point is approximately at the half chord of the wing root ($X_P = 12.80$ in.) and $X_A = 15.36$ inches. The two points nearly coincide and therefore, the difference between tunnel wall corrections for a swept and unswept wing are small. Note that, although an estimate for the induced angle of attack has

been calculated, when the angle of attack is referred to, the geometric angle of attack is implied.

2.7.2 Pressure Coefficients

Figures 2.15 - 2.20 compare wing surface coefficients of pressure for this test with results of reference [2]. The model tested in reference [2] had a wing similar to the MCAIR wing. The wing had a 44 degree leading sweep, -5.7 degree trailing edge sweep, 2.5 aspect ratio, and 0.2 taper ratio. The airfoil section was symmetrical. The upper and lower surfaces were circular arcs which formed sharp leading and trailing edges. The thickness of the airfoil section varied linearly from 6 percent of section chord at the wing root to 4 percent of section chord at the wing tip. The wing of reference [2] was tested at Mach number 0.26 and Reynolds number 0.16 million/ft (0.12 million based on mean aerodynamic chord of ref. [2] wing) while the MCAIR wing was tested at nominal Mach number 0.15 and nominal Reynolds number 1.0 million/ft (2.67 million). The comparisons made here are for the MCAIR wing at 8 degrees angle of attack and the wing of reference [2] at 8.3 degrees angle of attack, but similar comparisons could be made for angles of attack between 0 and 14 degrees. The wing of reference [2] had six spanwise rows of pressure taps. Figures 2.15 - 2.20 compare coefficients of pressure in each of these rows with a similar spanwise row of the MCAIR wing. The points plotted for reference [2] were obtained from graphs and therefore the pressure coefficients have an uncertainty of approximately 0.05. The coefficient of pressure distributions for the outboard 2 span locations of reference [2] agreed well with the coefficient of pressure distributions obtained for the MCAIR wing (see figures 2.19 - 2.20). The pressure coefficient distributions for the inboard 4 span locations of reference [2] follow the same trend as those of the MCAIR wing but there are slight differences (see figures 2.15 -

2.18). The differences between the coefficient of pressure distributions for the inboard 4 span locations of reference [2] and the coefficient of pressure distributions for the MCAIR wing appear to be due to differences in the formation of the leading edge vortex. Note that for the outer 2 span locations a developed leading edge vortex did not exist and therefore the pressure coefficients agreed closely. These differences could result from the Reynolds number variation between the two tests. The following section discusses the effects of Reynolds number on the pressure coefficients. The differences discussed are similar to those between the pressure coefficient distributions for the two wings.

2.7.3 Boundary Layer Trip and Reynolds Number Effects

Figures 2.21 - 2.28 illustrate the effects of boundary layer trips and Reynolds number on wing pressure coefficients for the 0-0 and 20-30 flap configurations. Boundary layer trips and increased Reynolds number induced reattachment of the separated flow over the leading edge vortex at more forward chord locations (see figures 2.23 and 2.24). The effects of boundary layer trips and increased Reynolds number were similar because they both induced transition from laminar to turbulent flow.

Boundary layer trips had the most effect at the lower Reynolds number and the increased Reynolds number had the most effect when the wing did not have a boundary layer trip. Both the boundary layer trip and increased Reynolds number had the most effect on coefficient of pressure distributions for span locations where reattachment of the separated flow over the leading edge vortex occurred between 30% and 50% of local section chord.

For the 20-30 flap configuration, the leading edge flap deflection inhibited the development of the leading edge vortex and therefore the effect of either boundary layer

trip or increased Reynolds number was limited (see figures 2.25 - 2.28). For the 0-0 flap configuration at low angles of attack, reattachment of the flow over the leading edge vortex occurred between 30% and 50% local section chord for outer span locations (see figure 2.29). For the 0-0 flap configuration at angles of attack of 10 and 14 degrees, reattachment of the flow over the leading edge vortex occurred between 30% and 50% local section chord for midspan locations (see figures 2.31 and 2.32). As angle of attack increased, the span locations most affected by the trip and Reynolds number moved inboard.

2.7.4 Separation

The isometric plots of upper surface pressure coefficients illustrate the separation characteristics of the wing. For the wing with no flap deflections, trailing edge separation begins at outer span locations between 6 and 8 degrees angle of attack (see figures 2.29 and 2.30). At an angle of attack of 10 degrees, the outer 40% of the wing span was separated (see figure 2.31). At 14 degrees angle of attack, the outer 60% of the wing span was separated (see figure 2.32). Leading edge flap deflections decreased the extent of separation. For the 20-0 flap configuration, trailing edge separation did not begin until approximately 10 degrees angle of attack (see figures 2.33 and 2.34). Trailing edge flap deflections increased the extent of separation. For the 0-30 flap configuration, flow separation existed for angles of attack from 0 to 14 degrees (see figure 2.35). Trailing edge flap deflections had a much greater effect on separation than leading edge flap deflections. For the 20-30 flap configuration, flow separation also existed for angles of attack from 0 to 14 degrees (see figure 2.36).

2.7.5 Global Coefficients

The integration of pressure forces over the wing provides a lift coefficient and a coefficient of pressure drag. In order to obtain a coefficient of drag, the friction drag of the wing must be included.

$$C_D = C_{D_p} + C_{D_{fr}} \tag{2.19}$$

Reference [18] provides an estimate of the coefficient of friction drag for a wing with a fully turbulent boundary layer.

$$(C_{D_{fr}})_{turbulent} = \frac{0.910}{(\log_{10} Re)^{2.58}} \tag{2.20}$$

For a Reynolds number of 1.0 million/ft or 2.67 million, based on mean aerodynamic chord, the estimated coefficient of friction drag is 0.007. For a Reynolds number of 1.3 million/ft or 3.5 million, based on mean aerodynamic chord, the estimated coefficient of friction drag is also 0.007.

Tables 2.3 - 2.6 list C_L, C_D, $\alpha_{geometric}$, $\alpha_{corrected}$, and $C_{D_{corrected}}$ for all cases tested. Figure 2.37 displays the lift coefficient versus corrected angle of attack for each of the wing configurations tested at nominal Re = 1.0 million/ft, nominal M = 0.15, and with a boundary layer trip.

Reference [12] used force data to obtain coefficients of lift and drag for a wing having 48.54 degrees of leading edge sweepback, an aspect ratio of 3.0, a NACA 64A010 wing section, and a taper ratio of 0.5. The MCAIR wing, with no flap deflections, differed in the thickness of the wing section, the taper ratio, and the orientation of the airfoil sections. The MCAIR airfoil sections were parallel to the root chord while the wing of reference [12] had airfoil sections oriented with quarter chords at an angle of 45 degrees to the root chord. Figure 2.38 displays the lift curve of the wing from reference [12] for Reynolds number 4 million and Mach number 0.25 and the lift curve (versus $\alpha_{corrected}$

) of the MCAIR wing, with no flap deflections, for Reynolds number 3.5 million and Mach number 0.19. The lift curve slope of the wing of reference [12] is approximately 0.052/deg and compares with 0.057/deg for the MCAIR wing.

Figure 2.38 also presents an approximation for the lift curve slope at zero lift obtained from reference [18].

$$\frac{dC_L}{d\alpha} = 0.1(\frac{AR}{AR+2})\sqrt{\cos\Lambda_{1/4}} \tag{2.21}$$

For the MCAIR wing, with AR = 3 and $\Lambda_{1/4} = 38.66$ degrees, equation 2.21 results in a lift curve slope of 0.053/deg which is in reasonably close agreement with the lift curve slope obtained from pressure integration.

Figure 2.39 is a comparison of the C_L versus $C_{D_{corrected}}$ for the MCAIR wing and reference [12] wing. These plots are for the same tests which provided the data for figure 2.38. The results show relatively good agreement between the drag coefficients obtained from pressure integration and those obtained from force measurements.

2.8 Summary

A low speed wind tunnel test has been carried out for a wing having a 45 degree leading edge sweep, aspect ratio of 3.0, taper ratio of 0.25, and deflectable leading and trailing edge flaps. The test was divided into the following three phases:

- Several reflecting plane configurations were tested and the pressure distributions on the reflecting planes measured. Each reflecting plane configuration was tested with the wing at 0, 8, and 14 degrees angle of attack and with no wing flap deflections. An "optimum" reflecting plane was selected on the basis of these measured

reflecting plane pressure distributions and was employed for the subsequent two phases.

- Wing surface pressure coefficients were determined for leading edge flap deflections of 0, 10, and 20 degrees and for trailing edge flap deflections of 0, 10, and 30 degrees. Measurements were made at wing angles of attack between -8 and 14 degrees and for nominal Reynolds number of 1.0 million/ft, nominal Mach number of 0.15, and with a wing boundary layer trip.
- Three additional groups of measurements were made for the 0-0 and 20-30 flap configurations at wing angles of attack between -8 and 14 degrees. These additional measurements were conducted according to the three following groups: (Reynolds number, Mach number, boundary layer trip) equal to (1.0 million/ft, 0.15, absent), (1.3 million/ft, 0.19, present), (1.3 million/ft, 0.19, absent).

The results of the experimental test indicate the following conclusions:

- Analysis of several ground board configurations showed that upwardly deflected flaps at the trailing edge of the ground board produced an undesireable pressure gradient upstream at the wing. Results indicated that ground board flaps should not be deflected and the trailing edge of the ground board should be more than one root chord downstream of the wing trailing edge.
- The coefficients of pressure obtained for this test are consistent with reference [2]. Each coefficient of pressure measurement had an approximate standard deviation of 0.023. Results of repeat runs indicated that the coefficients of pressure are repeatable to the order of magnitude of the standard deviation.
- The integration of coefficients of pressure over the wing surface is a reliable method for obtaining estimates of the wing coefficients of lift and coefficients of pressure

drag. Results showed good agreement with both theory and reference [12]. Reference [12] obtained force coefficients from force data and not pressure data.

- Results show that boundary layer trips and increased Reynolds number induced reattachment of the separated flow over the leading edge vortex at more forward chord locations. Both had the most effect on coefficient of pressure distributions where reattachment occurred between 30% and 50% of local section chord.

Chapter 3

Analytical Model

3.1 Panel Theory

This discussion of panel theory follows from reference [10].

3.1.1 Background

For most high-Reynolds-number flows in aircraft aerodynamics, viscous effects are confined to thin boundary layers, thin wakes, and centers of vortex cores. If shocks are absent and if rotational flow is confined to small regions, the flow may be modeled as a potential flow with embedded infinitely thin vortex sheets and vortex cores. In incompressible flow, this simplifies further to a linear potential flow model and Laplace's equation applies. The flow field and the position of the vortex sheets and cores can be solved for by employing a boundary-integral type of approach with singularity distributions solely on the surface of the body and vortex sheets. The linear potential flow model is the model underlying the classical panel method.

3.1.2 Governing Equations

For incompressible flow, the steady state potential flow equation reduces to Laplace's equation.

$$\frac{\partial^2 \varphi}{\partial x^2} + \frac{\partial^2 \varphi}{\partial y^2} + \frac{\partial^2 \varphi}{\partial z^2} = 0 \tag{3.1}$$

where $\vec{u} = \vec{U}_\infty + \vec{\nabla}\varphi$ and φ is the perturbation velocity potential. From Bernoulli's equation

$$C_p = 1 - \frac{|\vec{U}_\infty + \vec{\nabla}\varphi|^2}{U_\infty^2} \tag{3.2}$$

3.1.3 Boundary conditions

- On a body surface S_b the tangential flow condition is enforced.

$$(\vec{U}_\infty + \vec{\nabla}\varphi) \cdot \vec{n} = 0 \tag{3.3}$$

- On a vortex sheet S_w two conditions must be applied. The vortex sheet lies along streamlines and therefore the tangential flow condition applies. Also, the static pressure is continuous across the sheet.

$$\Delta C_p = C_p(S_w^+) - C_p(S_w^-) = 0 \tag{3.4}$$

- The Kutta condition is applied to insure that the flow leaves the trailing edge of wing-like bodies "smoothly".

- In the far field, the perturbation velocity vanishes.

Only for the rigid wake assumption is the boundary value problem linear. For the relaxed wake, the boundary conditions are slightly nonlinear with φ and highly nonlinear in terms of the position of the wake vortex sheets.

3.1.4 Integral representation of solution

For a three-dimensional rigid solid moving through a liquid it can be shown through Green's theorem [14] that the perturbation velocity potential at a point P is

$$\varphi_P = -\int\int_S \frac{\partial \varphi}{\partial n}(\frac{1}{4\pi r})dS + \int\int_S \varphi \frac{\partial}{\partial n}(\frac{1}{4\pi r})dS \tag{3.5}$$

The first term in equation (3.5) represents a distribution of sources while the second term represents a distribution of doublets, both on the surface S. Since for every doublet distribution there exists an equivalent vortex distribution [17], the perturbation velocity potential can be represented by source and vorticity distributions. For this analysis, source and vorticity distributions on the body surface and vorticity distributions on the wake sheets were used to represent the perturbation velocity.

3.1.5 Discretization and Solution Approach

The surface of the body and wake are divided into "small" quadrilateral elements (panels). Each panel has a control point, at its centroid, where the boundary conditions are enforced. A suitable functional singularity distribution for the panels must be assumed. The velocity influence at each control point due to a unit singularity distribution on each panel is calculated. A matrix of velocity influence coefficients (i.e. $[I_{\gamma_x}]$) is formed [6], and the x, y, and z components of the perturbation velocities at all control points are defined as follows.

$$\begin{aligned} \{u\} &= [I_{\gamma_x}]\{\gamma\} + [I_{q_x}]\{q\} \\ \{v\} &= [I_{\gamma_y}]\{\gamma\} + [I_{q_y}]\{q\} \\ \{w\} &= [I_{\gamma_z}]\{\gamma\} + [I_{q_z}]\{q\} \end{aligned} \tag{3.6}$$

In a like manner, the normal components of the perturbation velocities at the panel control points are defined as follows.

$$\{V_n\} = [I_{\gamma_n}]\{\gamma\} + [I_{q_n}]\{q\} \tag{3.7}$$

Since the tangential flow condition is enforced on the body, the normal component of the perturbation velocity at each control point must be equal in magnitude, but opposite in sign to the normal component of the freestream velocity.

$$[I_{\gamma_n}]\{\gamma\} + [I_{q_n}]\{q\} = -\{(U_\infty)_n\} \tag{3.8}$$

Thus, the panel singularity strengths, $\{\gamma\}$ and $\{q\}$, can be solved for by a simple matrix inversion. For a relaxed wake, the boundary condition of zero normal flow at the wake sheet control points is not enforced so that the wake shape may be found iteratively. This does not, however, alter the solution procedure if the vorticity strengths of the wake panels have a known relation to the vorticity on the body. This will be futher discussed in the section on the wing model.

3.2 Model Basis

Wind tunnel wall effects on finite wing flow fields for conditions varying from fully attached to fully separated flow were the primary objective using a separated flow panel method. The wing model is, in fact, an extension of a vortex panel method to three-dimensions. The basis for the model of a finite wing with separation is the two-dimensional method of Dvorak and Maskew [4]. A two-dimensional airfoil is essentially a wing of infinite span which itself is represented by a single strip of panels each of infinite span; the three-dimensional model is a wing of finite span represented by several strips of panels each of finite span. An increased number of strips is required, of course, to account for variation in lift along the wing span.

The solution procedure requires an inner and outer iterative loop. The outer iterative loop is an analysis of the viscous boundary layer that determines separation locations. The inner iterative loop allows for relaxation of the wake shape. Because the wake shape is unknown *a priori*, an initial shape is assumed and relaxation proceeds until the shape converges.

The wind tunnel wall effect on wings with or without separation, follows from modeling both in free air and in a wind tunnel environment. The only modeling difference between the two flow conditions is the presence or relative location of the tunnel walls. The wind tunnel environment is modeled as a long open-ended cylinder installed in an external flow field and parallel to that flow field. The wing is modeled as in free air, but is located in the interior of the open-ended cylinder (see figure 3.1). Note that since flow symmetry exists, the solution procedure can be simplified by discretely modeling only the wing semi-span and the corresponding tunnel half.

3.3 Flow Regions

A sketch of the cross-section of a flow field for a separated flow wing is shown in figure 3.2. Four distinct flow regions can defined.

- *Potential flow regions*

  Those regions external to boundary layer, free shear layer, and wake regions. Assumed to be irrotational flow since the shear is small in these regions and therefore produces negligible vorticity.

- *Boundary layers*

  The thin regions adjacent to the wing and tunnel surfaces in which velocity gra-

dients and hence vorticity are large. The boundary layer is assumed to be of negligible thickness and the modeled vorticity is concentrated on the physical boundary surfaces.

- *Free shear layers*

  The thin region of shed vorticity fed by the separating boundary layer. Assumed to be of negligible thickness and therefore represented by a slip surface.

- *Wake regions*

  The region bounded by the upper and lower free shear layers. Assumed to have negligible vorticity and a constant total pressure and is therefore considered to be a potential flow region.

Essentially, the modeling reduces the problem to only potential flow regions which can be represented in a simple and straightforward manner by the use of vortex panels. Panels distributed on the tunnel and wing surfaces represent the vorticity located in the boundary layers and satisfy the tangential flow condition on those surfaces. The free shear layers of the wake are also modeled with vortex panels. Swept, untapered vortex panels with a linear distribution of vorticity along the panel chord and a constant distribution of vorticity along the panel span are used [1].

3.4 Wing Model

The vorticity on wing surface panels models both the wing thickness and its lifting character or circulation. Figure 3.3 illustrates the method of distributing panels on the wing surface. The corners of wing panels are determined by dividing the wing into streamwise strips of equal span and then placing points at the inboard and outboard

edges of each strip and on the wing surface according to the following distribution.

$$\frac{x_i'}{c} = 1 - \cos(\frac{i}{nc}\frac{\pi}{2}) \qquad where \quad i = 0, nc \tag{3.9}$$

For a wing with arbitrary sweep and no taper, the four corner points of each panel define a swept, untapered panel. For a wing with arbitrary sweep and arbitrary taper, the four corner points define a swept, tapered panel which is approximated by a swept, untapered panel of equal area. Equation (3.9) concentrates panels at the wing leading edge and thus better defines the shape of the leading edge and locates more control points where there are large variations in pressure.

Figures 3.4 and 3.5 represent the two basic flow conditions that exist for a streamwise strip. The number of vortex strength unknowns at panel leading and trailing edges and tangential flow conditions at panel centroids (control points) both equal $2 \cdot nc_{wing}$. The Kutta Condition for the attached case (figure 3.4), requires that $\gamma_{te} = 0$ while for the separated case (figure 3.5), $\gamma_{te_l} = -\gamma_{sep}$. In order to balance the number of boundary conditions and unknowns, a sheet source is distributed uniformly over the streamwise strip. Since the vorticity of the upper free vortex sheet equals γ_{sep} and that of the lower sheet equals $-\gamma_{sep}$, the wake does not introduce any additional unknowns.

The vortex lines distributed on the panels trail downstream along the edges of each streamwise strip. The trailing vorticity leaves the body surface at the separation node and continues to follow the edges of the streamwise strip in the wing wake. At the termination of the paneled wake, the vorticity trails downstream to infinity parallel to the x-axis.

3.5 Wake Model

Figure 3.6 shows the trailing edge separation flow model. The separation line and free vortex sheets are discontinuous at the edges of streamwise strips. Free vortex sheets are limited to vertical movement only and therefore wake roll-up is not modeled. Each free vortex sheet is modeled with vortex panels joined end to end from the separation line to termination of the sheet.

3.5.1 Wake shape relaxation

A free vortex sheet cannot support a pressure force and therefore must lie along a streamsurface. Because the streamsurfaces are not known *a priori*, the wake shape must be determined through an iterative process. Initially, the free vortex sheets are specified to trail downstream at $\frac{\alpha}{2}$. The potential flow solution satisfying the wing surface boundary conditions will produce normal velocities on the vortex panels of the free vortex sheets until the wake shape converges to a consistent contour. Beginning at the first panel downstream of separation and proceeding downstream, each panel must be rotated by $\Delta\theta$ given by

$$\Delta\theta = \arctan(\frac{\vec{u}\cdot\vec{n}}{\vec{u}\cdot\vec{t}}) \tag{3.10}$$

Since the free vortex sheets are continuous the wake panels are translated before rotation to insure that the leading edge of each panel coincides with the trailing edge of the panel immediately upstream. Convergence of the wake shape is assumed when the normal velocity on all wake panels is less than 1% of the freestream velocity.

3.5.2 Wake length

An abrupt termination of free vortex sheets is physically incorrect, but is justified as a reasonable approximation at a sufficient distance from the wing surface [4]. However, the accuracy of the approximation is dependent on the length of the free vortex sheets. Figure 3.7 shows the lift curves for a NACA 4412 airfoil with prescribed separation locations and various trailing vortex sheet lengths. Note that for angles of attack below stall, the wake length has little effect on lift coefficient. Reference [4] suggests a methodology for determining wake length which is adopted for this model. The wake length is defined in figure 3.8. In order to determine the wake length the wake height and wake length factor must be known. The wake height is dependent on separation location while the wake length factor is obtained from an empirical curve which relates wake length factor to airfoil thickness/chord ratio (see figure 3.9). Values of wake length factor presented in [4] are limited to thickness ratios greater that 10 percent. Therefore, for thickness ratios less than 10 percent, wake length factors were obtained by extrapolation. For the 64A005 airfoil section, an extrapolated wake length value of 3.0 was used for all cases.

3.6 Tunnel Model

As stated earlier, the tunnel is modeled as a long open-ended cylinder with vortex panels distributed on its surface. Tunnels with elliptic cross-sections can be modeled by specifying the major and minor axes. Figure 3.1 illustrates the paneling distribution on the tunnel surface. Chapter 2 discusses the tunnel shape and reflecting plane location used for the experiment. The panel method calculations were conducted with an approximate circular tunnel and the relative relationship between the actual tunnel and the modeled tunnel is shown in figure 2.14. This circular tunnel was used because when

modeling the actual tunnel shape, a discontinuity in the slope on the tunnel surface occurs at the reflecting plane. The slope discontinuity induced an oscillating vorticity distribution along the tunnel length for the adjacent panel strips. The circular tunnel eliminates this effect and also is a close approximation to the actual tunnel. Rings of panels are placed end to end to form the tunnel. The distribution of panels around each ring is accomplished by placing control points on the tunnel surface according to the following equation.

$$\phi_i = \frac{1}{ns_t}(i - \frac{1}{2})\frac{\pi}{2} \qquad i = 1, 4 \cdot ns_t \tag{3.11}$$

Rectangular panels are then determined from the intersection of planes tangent to the tunnel at the control points.

When modeling flow through the wind tunnel, several conditions must be satisfied or closely approximated.

- a uniform flow field of velocity U_∞ for tunnel locations far upstream of the model
- a stable flow condition for tunnel locations far downstream of wing.
- conservation of mass flow (i.e. no leakage)

The finite forward extension of the tunnel actually perturbs the flow at the inlet. However, the perturbation decreases as the tunnel boundary is extended further upstream of the wing and Holt and Hunt [11] suggest that a forward extension of 10 chordlengths is adequate for tunnel simulations. Reference [11] also suggests a check on the velocity at the inlet because the blockage effect of the wing could reduce the inlet speed below U_∞ if the upstream extension is not sufficiently long. For most cases tested, the flow at the inlet was within approximately 1% of U_∞.

The vorticity trailing from the wing and downstream of the paneled wake is specified

to trail in the direction of the tunnel central axis. Therefore, the wing trailing vortex system is in a stable flow condition for tunnel locations downstream of the paneled wake. In order to satisfy the stable flow condition, the remaining requirement is that vorticity on the tunnel walls downstream approach a stable solution. The suggestion is that a downstream extension of 10 chordlengths is adequate [11].

The leakage constraint through the tunnel walls requires some knowledge of where leakage is likely to occur, so that paneling density can be increased in these areas. Since flow "through tunnel walls" is most likely (for a finite number of control points) to occur in the vicinity of the wing, panel control points have been concentrated there. To accomplish this, the freestream length of the panels of successive tunnel rings were specified by a sine function.

$$\frac{c_i}{c} = |\sin(\frac{i}{nc_t}\pi) - \sin(\frac{i-1}{nc_t}\pi)| \qquad i = 1, nc_t \tag{3.12}$$

Since the tunnel extends equal distances upstream and downstream from the midpoint of the wing root chord, the maximum paneling density is located there.

It should be noted that the tunnel is essentially treated as a wing, and thus, there is a Kutta condition and a trailing vorticity system downstream of the paneled tunnel. The Kutta condition is enforced simply by requiring the vorticity at the tunnel trailing edge to be zero. The vorticity trailing downstream is specified to trail in the freestream direction.

3.7 Boundary Layer Analysis

With the flow regions properly represented based on vortex panels, the remaining requirement for predicting the aerodynamic characteristics of a wing is the determina-

tion of any separation locations on the wing surface. The present computational model has the option of specifying either the separation location or the Reynolds number. When a separation location is specified, the model only requires the wake to relax until it represents flow streamsurfaces. If the Reynolds number is specified, a boundary layer analysis is performed to determine the separation locations.

As noted earlier, the wing was divided into several streamwise strips. The boundary layer on each of these streamwise strips was approximated using two-dimensional methods. Along each strip, the boundary layer was laminar from the stagnation point to either the point of transition or of laminar separation. Because of the difficulty in modeling a laminar separation bubble, immediate reattachment of the laminar separation as a turbulent boundary layer was assumed. From the transition or reattachment location to the wing trailing edge, Stratford's Criterion for turbulent separation was used to determine if the boundary layer separated. Although two-dimensional methods were used, the flow on the wing actually had a component along the wing span. This was partially accounted for by the definition of an effective two-dimensional velocity,

$$u_e = \sqrt{u^2 + v^2} \tag{3.13}$$

which is the velocity used in the boundary layer analysis.

3.7.1 Laminar boundary layer

Thwaites [20] has shown that, for many types of laminar boundary layers, the momentum thickness(θ) can be determined by

$$\theta^2 = 0.45 \frac{\nu}{u_e^6} \int_{x_{stag}}^{x} u_e^5 dx \tag{3.14}$$

He also defined a dimensionless pressure gradient parameter

$$\lambda \equiv \frac{\theta^2}{\nu}\frac{du_e}{dx} \tag{3.15}$$

Thwaites determined that laminar separation occured when $\lambda < -0.09$. If u_e is nondimensionalized by u_∞ and it is noted that $Re = \frac{u_\infty L}{\nu}$, the above equations become

$$\theta^2 = 0.45\frac{L}{Re}\frac{1}{(\frac{u_e}{u_\infty})^6}\int_{x_{stag}}^{x}(\frac{u_e}{u_\infty})^5 dx \tag{3.16}$$

$$\lambda = \theta^2\frac{Re}{L}\frac{d(\frac{u_e}{u_\infty})}{dx} \tag{3.17}$$

With Re and the distribution of $\frac{u_e}{u_\infty}$ known, the above equations determine θ and λ from the stagnation point to the point of either laminar separation or transition to turbulence.

Michel [17] determined from experimental data on airfoils that transition from a laminar to turbulent boundary layer occurs when

$$Re_\theta > 1.174(1 + \frac{22,400}{Re_x})Re_x^{0.46} \tag{3.18}$$

where

$$Re_\theta = \frac{u_e\theta}{\nu} = \frac{Re}{L}(\frac{u_e}{u_\infty})\theta \tag{3.19}$$

$$Re_x = \frac{u_e x}{\nu} = \frac{Re}{L}(\frac{u_e}{u_\infty})x \tag{3.20}$$

When laminar separation occurs, immediate reattachment as a turbulent boundary layer is assumed. Transition is also assumed to occur over a negligible distance. That is a laminar boundary layer momentum thickness at transition and laminar separation is assumed to be the momentum thickness at the beginning of the turbulent boundary layer.

$$(\theta_{turbulent})_{initial} = (\theta_{laminar})_{final} \tag{3.21}$$

3.7.2 Turbulent boundary layer

A modified version of Stratford's Criterion [19], suggested by Cebeci and Smith [3], was used to determine if the turbulent boundary layer separated. Turbulent separation was predicted by the following equation.

$$\frac{\bar{C}_p(\bar{x}\frac{d\bar{C}_p}{d\bar{x}})^{\frac{1}{2}}}{(10^{-6}R)^{0.1}} = \mathcal{F}(x) \tag{3.22}$$

$$\mathcal{F}(x) < 0.3 \quad \textit{no separation} \tag{3.23}$$

$$0.3 < \mathcal{F}(x) < 0.5 \quad \textit{separation at } \mathcal{F}_{max} \tag{3.24}$$

$$0.5 < \mathcal{F}(x) \quad \textit{separation} \tag{3.25}$$

where

$$R = \frac{u_m \bar{x}}{\nu} \tag{3.26}$$

$$\bar{C}_p = \frac{p - p_m}{\frac{1}{2}\rho u_m^2} = \frac{C_p - C_{p_m}}{1 - C_{p_m}} \tag{3.27}$$

Figure 3.10 presents the relationship between the actual flow parameters and the equivalent (i.e. $\bar{x}$) flow parameters. If turbulent separation is predicted at a panel control point, the separation location is assumed to occur at the trailing edge of that panel.

Chapter 4

Results

4.1 Paneling

Determination of the number of streamwise strips along the wing semi-span (ns), the number of panels along the chord (nc), and the number of wake panels downstream of the wing trailing edge was based on several factors, including modeling simplicity and realistic behavior of the solutions. The analytical model of the wing consisted of streamwise strips of constant span and panels which were distributed along those strips in the chordwise direction. Typically, for a finite span wing, it is preferable to have several streamwise strips along the wing span in order to model spanwise lift variations as well as spanwise variations of separation locus. For the fully attached case, the experimental wing discussed in Chapter 2 was modeled with as many as nine streamwise strips. For the present model, however, convergence of the wake shape has not been achieved for finite wings for which the ratio $\frac{ns}{b}$ is greater than unity. Examples presented by Dvorak etal [5] also included only cases for which the ratio $\frac{ns}{b}$ is less than unity.

The current limitations on $\frac{ns}{b}$ for separated flows using the analytical model discussed in Chapter 3 are similar to those that the panel method developed by Burns [1] experienced. He originally enforced a Kutta condition by specifying that $\gamma_{te_l} = -\gamma_{sep}$ and applied this for both separated and attached flows. Thus, for an attached flow γ_{te_l}

$= -\gamma_{te_u}$. This condition led to proper behavior for two-dimensional wings, or similarly for wings with relatively "small" ratios of $\frac{ns}{b}$. Figure 4.1 illustrates the typical behavior for attached flows when $\frac{ns}{b}$ is no longer "small". The figure shows the vorticity distribution on the upper surface of a rectangular wing of at an angle of attack of zero degrees. The wing had a NACA 64A005 airfoil section, AR = 6, nc = 20, ns = 6, b = 6.0, and thus the ratio $\frac{ns}{b}$ is unity. Since the wing is at zero degrees angle of attack and has a symmetric section, the lower surface mirrors this effect and the panel boundary conditions are indeed satisfied. However, the large vorticities at the wing trailing edge induce unrealistically large velocities at points near the trailing edge. In an attempt to alleviate this problem, a Kutta condition for attached cases was enforced by specifying that $\gamma_{te} = 0$. This however, introduces an additional boundary condition since it in effect requires the specification that $\gamma_{te_u} = 0$ and $\gamma_{te_l} = 0$. In order to equate the number of boundary conditions and unknowns the two tangential flow requirements on the upper and lower surface trailing edge panels of each streamwise strip were replaced by the single condition that the tangential velocities are equal on those two panels. Figure 4.2 shows the improved vorticity distribution on the upper surface of a rectangular wing at an angle of attack of zero degrees and with these new boundary conditions. The wing had a NACA 64A005 airfoil section, AR = 6, nc = 20, ns = 6, b = 6.0, and thus the ratio $\frac{ns}{b}$ is unity. The only difference between the testing conditions for figures 4.2 and 4.1 was the boundary conditions. The magnitude of the vorticity near the wing trailing edge was reduced and thus the velocities at the trailing edge were reduced appreciably. An increase in vorticity to a peak value occurred at the wing outboard trailing edge panel. This problem was accentuated and affected inboard locations for wings with increasing ratios of $\frac{ns}{b}$. Figure 4.3 shows the vorticity distribution on the upper surface of a rectangular wing at zero degrees angle of attack. The wing had a NACA 64A005 airfoil section, AR = 3, ns = 6, nc = 20, b = 3.0, $\frac{ns}{b} = 2.0$, and shows the affect on

inboard locations for ratios of $\frac{ns}{b}$ greater than unity. Figure 4.2 clearly shows that the problem is essentially a "tip effect" because for a $\frac{ns}{b}$ value of unity, the vorticity peak exists solely on the wing outboard trailing edge panel.

The finite thickness, or gap, which exists between the upper and lower surfaces at the wing tip appears to be responsible for this "tip effect". Figure 4.6 shows the finite distance which exists between the vorticity trails which follow the outer edge of the outboard streamwise strips on the upper and lower surfaces. For a real wing, either the thickness of the wing goes to zero at the wing tip or the wing tip essentially has a vertical panel which closes the tip. A vertical panel still results in a vertical space between the upper and lower vorticity trails, but the additional singularity distributions and control points now affect the strengths of the vorticity trails and thus influence the final solution. It was assumed that for an unclosed wing tip, the vorticity trails following the outboard strip edges should be located vertically midway between the upper and lower surfaces at the outboard edge. For a symmetric wing at an angle of attack of zero degrees, this essentially ensures that the vorticity trails at the outboard edge vanish since there is flow symmetry on the upper and lower surfaces and $\Gamma_L = -\Gamma_U$. Figures 4.4 and 4.5 are for the same wing and conditions as were figures 4.2 and 4.3 respectively. The results for these figures were obtained by eliminating the voriticity trailing along the outer edges of the outboard wing panels. For all panels on the outer edge strips, the vorticity which was forced to vanish only included that vorticity trailing along the outer edge of a panel which was due to upstream panels and not the vorticity trailing along the edge of the panel from the bound vorticity on its own surface. The improvement is dramatic and illustrates that there is a "tip effect". The continued presence of a reduced "tip effect" was due to the vorticity trailing along the panel edge from the bound vorticity on its surface. Since the velocity induced by Γ_U and Γ_L should be zero if the upper and lower vorticity trails coincide at a vertically intermediate location, the

effect of such a vertical gap can be determined by examining the velocity produced on a panel control point by the vorticity trailing downstream along the panel edges at the wing tip. The control point examined was on the upper surface outboard strip. The wing was assumed to be at an angle of attack of zero degrees. The following derivation relates to figure 4.6.

$$V_{n_U} = -\frac{\Gamma_U}{4\pi l} \tag{4.1}$$

$$V_{n_L} = -\frac{\Gamma_L}{4\pi l}\left(\frac{1}{1+(\frac{r}{l})^2}\right) \tag{4.2}$$

$$\Delta V_n = V_{n_U} + V_{n_L} \tag{4.3}$$

$$\Delta V_n = -\frac{\Gamma_U}{4\pi l}\left(1+\frac{\Gamma_L}{\Gamma_U}\left(\frac{1}{1+(\frac{r}{l})^2}\right)\right) \tag{4.4}$$

For $\alpha = 0$, Γ_L = -Γ_U

$$\Delta V_n = -\frac{\Gamma_U}{4\pi l}\left(\frac{(\frac{r}{l})^2}{1+(\frac{r}{l})^2}\right) \tag{4.5}$$

Noting that,

$$l = \frac{b/2}{2 \cdot ns} = \frac{1}{4}\left(\frac{b}{ns}\right) \tag{4.6}$$

$$\Delta V_n = -\frac{\Gamma_U}{4\pi}\left(\frac{4 \cdot ns}{b}\right)\left(\frac{(\frac{4 \cdot ns}{b})^2 r^2}{1+(\frac{4 \cdot ns}{b})^2 r^2}\right) \tag{4.7}$$

Since a real wing has a closed tip ($r = 0$), ΔV_n from equation (4.7) is zero. For wings modeled with r nonzero, it is clear that when the ratio of $\frac{ns}{b}$ approaches zero, ΔV_n also approaches zero. Thus for two-dimensional wings ($\frac{ns}{b} = 0$), "tip effects" don't occur as mentioned previously. As $\frac{ns}{b}$ becomes larger, ΔV_n increases as illustrated by the increased "tip effect" present in figures 4.2 and 4.3. An increase in r for a constant $\frac{ns}{b}$ also increases ΔV_n. Figure 4.7 shows the vorticity distribution on the upper surface of a rectangular wing with AR = 6, nc = 20, ns = 6, b = 6.0, $\frac{ns}{b}$ of unity, and a NACA 0010 airfoil section. Comparing results for figures 4.7 and 4.2, the doubling of r increases the "tip effect". However, a doubling in the magnitude of r has a lesser effect than a doubling of $\frac{ns}{b}$ as can be seen by comparing figures 4.2 and 4.3. Equation (4.7)

indicates that ΔV_n should in fact be affected more by a factor of 2 increase in $\frac{ns}{b}$ than a corresponding increase in τ.

Woodward [6] suggests problems generally exist for attached flow vortex panel methods due to the formation of an ill-conditioned matrix if γ_{te_u} and γ_{te_l} are not individually set equal to zero . Instead of replacing the two tangential flow boundary conditions on the upper and lower trailing edge panels with the one condition of equal tangential velocities, he suggests the application of these two conditions along with the addition of an unknown line source strength in the wing interior. He also states that the strength of the line source should be relatively small because it is not needed to actually solve the boundary conditions. Despite it being unnecessary, it did not in fact tend to vanish and produced results which had varying effects at the wing tip depending on its location in the interior of the wing.

The method of Dvorak etal [5] solved the problem related to determining the line source location by distributing a sheet source on the wing surface. An interesting aspect of the distribution of the sheet source on the surface is its solution of the "tip effect" problem for attached cases. What is even more interesting is that Dvorak etal [5] did not distribute sources on the surface to solve the "tip effect" problem. The wing model was a direct extension of a two-dimensional model to three-dimensions, and since the two-dimensional model distributed sources on the wing surface, the three-dimensional model also did. Since the "tip effect" does not occur for two-dimensional cases, the source distribution was not originally required to solve such problems and was thus implemented for other reasons. Although the sheet source distributions were not introduced for this purpose, they do indeed correct for ΔV_n on the outboard streamwise strip. Figure 4.8 shows the vorticity distribution on the upper surface of a rectangular wing at zero angle of attack and with a NACA 64A005 airfoil section, AR = 6, nc =

20, ns = 6, b = 6.0, $\frac{ns}{b}$ of unity, and was obtained using the analytical model presented in Chapter 3 and thus by distribution of sheet sources on the wing surface. No "tip effect" is apparent and for $\frac{ns}{b}$ ratios as high as 8 there are no further indications of "tip effects". Figure 4.8 shows the increase in sheet source strength at the tip for this same wing. For positive values of Γ_U, equation (4.7) predicts a ΔV_n in the negative z-direction for a control point on the upper surface and thus the increased source strength clearly compensated for ΔV_n on the outboard strip.

Since the wake is solved as discontinuous vortex strips, what has been referred to as a "tip effect" up to now, also produced similar solution behavior for wake shape convergence when $\frac{ns}{b}$ was greater than unity. Since the vorticity trails follow the edges of the streamwise strips, and the wake is discontinuous at the edges of these strips, as it is also on the body surface at the wing tip, a ΔV_n exists at wake control points. This is the reason that $\frac{ns}{b}$ must be kept approximately equal to unity for the wake shape to converge. Since no sources exists on the wake surfaces, the ΔV_n cannot be compensated for as simply as on the body surface. As a result, for positive angles of attack and separation locations upstream of the trailing edge, the upper free vortex sheet has a ΔV_n in the negative z-direction. The lower free vortex sheet correspondingly has a ΔV_n in the positive z-direction. Therefore, the upper wake strips continuously rotate down, the lower wake strips continuously rotate up, and the wake strips cross and do not converge. In order to eliminate the ΔV_n present due to discontinuity of the wake sheets, three possible options are listed below.

- a) the wake sheets must be modeled continously
- b) the concentrated vorticity trails should not be located at discontinuous panel side edges, but at locations intermediate to the edges of adjacent streamwise strips.
- c) the ratio $\frac{ns}{b}$ must be limited to values less than unity.

Items a) and b) represent possible future approaches, but for the model as presented in Chapter 3, the approach suggested for item c) was followed.

For a wing with $\Lambda_{le} = 45$ degrees, AR = 3, NACA 64A005 airfoil section, $\lambda = 0.25$, and b = 1.875, a value of approximately unity for $\frac{ns}{b}$ requires ns = 2. Although only two streamwise strips were used to model the wing, fully attached modeling based on ns > 2 was carried out to show that cases with ns = 2 provided an acceptable result. An investigation of the effects of ns and nc was conducted for a wing angle of attack of 10 degrees and fully attached flow. Figure 4.10 shows the variation of lift coefficient with inverse number of semi-span panels for various numbers of chordwise panels. Note that the C_L convergence is not linear with the inverse number of semi-span panels as is the case for most first order panel methods in which the lifting surface then is approximated by a flat plate. For a flat plate vortex panel method, the modeled lifting surface is always the identically same flat plate. Therefore, the actual values of ns and nc only change the extent to which the pressure distribution is defined. For vortex panels distributed on a wing surface, variations in ns and nc levels actually change the shape of the wing that is being modeled. Thus the pressures and wing shape are better defined with an increase in panel number and the variation of C_L with 1/ns and 1/nc is not linear. The behavior for nc = 5 is unexpected, however, for larger values of nc the variation of C_L with 1/ns is relatively consistent and appears to indicate a converged solution within 5% of that obtained from the following. [18]

$$\frac{dC_L}{d\alpha} = 0.1\left(\frac{AR}{AR+2}\right)\sqrt{\cos\Lambda_{1/4}} \tag{4.8}$$

For a wing with AR = 3, $\Lambda_{1/4} = 38.66$, and $\alpha = 10$ degrees, a theoretical lift coefficient of 0.530 is obtained. Thus figure 4.10 shows that for ns = 2 and nc values of 5,10,15,20, and 25, the panel method provides reasonable values of C_L. The average C_L for ns = 2 was within 8% of that predicted from equation (4.8) and there was a spread of $\pm$

1.5% about the average. A nc value of 20 was chosen to model the wing because it provided a suitable paneling density for the analysis. Figure 4.11 shows the variation of C_L with 1/ns for nc = 20. Figure 4.12 shows the variation of C_L with 1/nc for ns = 2. The wake downstream of the trailing edge for each streamwise strip was modeled with 4 panels. For most cases, this provided a relatively smooth and continuous paneling distribution from the wing trailing edge into the downstream wake. The surrounding tunnel surface was modeled with 20 panels along its length and with 10 panels around half of the tunnel circumference. This provided an adequate paneling density for tunnel sections in the vicinity of the wing model.

4.2 Comparison with experiment

The experimental data of Chapter 2 provides an excellent base with which to compare results from the analytical method. Figure 4.13 compares the lift coefficients obtained for the experiment and the lift coefficients obtained from the panel method. Since the airfoil section is symmetric, the lift coefficient at zero angle of attack should identically be zero. Apparently, the experiment was conducted with an angle of attack offset that was determined by relating the lift coefficient at what had been thought to be zero angle of attack to the lift curve slope at that point. From this information, an angle of attack offset of 0.44 degrees was determined. When the experimental data were corrected for the offset angle, results from the experiment and panel method proved to be within approximately 2% for angles of attack up to and including 8 degrees.

The panel method predicted fully attached flow for angles of attack up to and including 6 degrees (see figure 4.14). At 8 degrees, the analytical model predicted separation of the outboard strip at approximately 5% of the local chord (see figure 4.15). From the

experimental pressure distribution in figure 2.30, the outboard 50% of the wing appears to be separated as predicted by the analytical model. The experimental pressure distribution in figure 2.29 also seems to justify the fully attached prediction for 6 degrees angle of attack.

For angles of attack greater than 8 degrees, C_L from the panel method is underpredicted by approximately 6%. The upper surface pressure distributions obtained from experiment (see figures 2.31 and 2.32), seem to show that separation exists near the leading edge for approximately the outer 50% and 85% of the wing semi-span for angles of attack of 10 and 14 degrees respectively. The panel method predicted separation over 100% of the wing semi-span for all angles of attack greater than or equal to 10 degrees. The separation location for all angles of attack greater than 8 degrees and for both the inboard and outboard strips was approximately 5% of the local chord (see figures 4.16 and 4.17). Since the experiment shows separation over less of the wing semi-span than the analytical model for these angles of attack, modified panel method calculations were performed which forced the inboard strip to remain attached. This was carried out by specifying the separation location originally determined by the panel method for the outboard strip as well as specifying that the inboard strip was fully attached. Figure 4.18 compares the lift coefficient from experiment, the original calculations, and the modified calculations. The modified panel method calculations for 10 degrees angle of attack agree closely with experiment. Notice how the original and modified panel method calculations bound the experimental data. This implies that the actual separation occurs between the root and 50% of the wing semi-span for angles of attack greater than 10 degrees as was also seen in figure 2.31. Since a more accurate spanwise variation of the separation locus could not be modeled for such a low aspect ratio wing, this limitation cannot presently be avoided. If separation should occur over the outer 85% of the semi-span as suggested by experiment for 14 degrees angle of attack, the

panel method can best approximate this with separation of the inboard and outboard strips and thus underpredicts the value of C_L. Although limitations in the discrete spanwise separation locus possibly explain the underpredictation of C_L for angles of attack of 12 and 14 degrees, another difference between the experiment and the analytical model is the prediction of separation for the inboard strip for $\alpha = 10$ degrees. The panel method predicted separation for the inboard strip while the experimental data suggests fully attached flow. The presence of a leading edge vortex on the experimental wing could possibly explain the differences between results from the experiment and the panel method. A leading edge vortex formation on a swept tapered wing delays separation. Since the panel method does not model a leading edge vortex formation, it seems plausible that separation will not be delayed, as is the case for the panel method. Thus, the limitations of the application of a two-dimensional boundary layer analysis to this three-dimensional flow may account for the discrepancy in separation prediction. In addition to the delay of separation, the formation of a leading edge vortex produces a lift augmentation which the panel method does not include. Thus, for higher angles of attack where the lift augmentation due to the leading edge vortex would be greater, the lift coefficient from the panel method would be underpredicted. Although the lift coefficients at the higher angles of attack were slightly underpredicted by the panel method, the relative differences between the free air and wind tunnel analytical models provide insights about the relative differences between the experiment and the actual free air flow condition.

4.3 Comparison of free air and tunnel

Figure 4.19 compares the lift curves obtained from the panel method, for the wing in free air and in the wind tunnel. Reference [18] presents a method for determining the

angle of attack induced on a finite wing model in a circular tunnel by the use of image vortices. Although that method is applicable for rectangular wings with a constant spanwise lift distributions, it does provide a simple approximation for the induced angle of attack due to tunnel walls. Figure 2.14 shows the location of image vorticies required to produce a streamline at the tunnel walls. The image vorticies produce an upwash at the wing and effectively increase the angle of attack of the wing model. As predicted by classical corrections, the lift coefficient in the wind tunnel is greater than the lift coefficient in freestream flow.

$$\Delta\alpha_i = \delta(\frac{S}{C})C_{L_t} \tag{4.9}$$

$$C_{L_f} = C_{L_t} - \Delta\alpha_i(\frac{dC_L}{d\alpha})_t \tag{4.10}$$

$$C_{L_f}/C_{L_t} = 1 - \delta(\frac{S}{C})(\frac{dC_L}{d\alpha})_t \tag{4.11}$$

The ratio of wing planform area to tunnel cross-sectional area (S/C) for the simulation of the experiment was 0.228. For a circular tunnel $\delta = 0.125$ [18]. The lift curve slope at zero lift as determined by the panel method for the wing in the wind tunnel was $(\frac{dC_L}{d\alpha})_t = 0.066$. For these values, equation (4.11) predicts $C_{L_f}/C_{L_t} = 0.89$. Figure 4.20 is a plot of C_{L_f}/C_{L_t} versus α for the original panel method calculations. The approximate ratio of C_{L_f}/C_{L_t} was 0.86 and thus varies by only 3.5% from the theorectical calculation. This implies that the tunnel wall corrections for lift coefficient do not vary much over this angle of attack range even for large wing models. The relative consistency of C_{L_f}/C_{L_t} gives some indication that an estimate of the wall corrections for separated flow conditions on wings for moderate angles of attack such as 10 to 14 degrees, may be obtained from an analysis of the wall corrections for an unseparated wing at low angles of attack.

4.4 Variation of tunnel diameter

The results discussed in this section refer to modeling of the 45 degree leading sweep wing of Chapter 2 and circular cross-section tunnels with various ratios of wing span to tunnel diameter. As the tunnel scale increases to infinity relative to the model scale (b/B $\rightarrow$ 0), the flow in the wind tunnel approaches that of an equivalent free air flow and thus C_{L_f}/C_{L_t} should approach unity. Also, as b/B approaches unity C_{L_f}/C_{L_t} should decrease due to the increased upwash produced on the wing model by the tunnel walls. Figure 4.21 shows the variation in C_{L_f}/C_{L_t} for the wing at an angle of attack of 4 and 14 degrees with various wing span to tunnel diameter ratios (b/B). For the wing at $\alpha = 4$ degrees, C_{L_f}/C_{L_t} decreases rapidly as b/B is increased from 0.6 to 0.85. For the wing at $\alpha = 14$ degrees, the same trend is evident for b/B values up to 0.80. The magnitude of C_{L_f}/C_{L_t} is less for $\alpha = 14$ degrees and b/B values less than 0.80. Some interesting behavior is apparent for b/B = 0.85 and $\alpha = 14$ degrees. Figure 4.22 shows the theoretical upwash from classical corrections produced by image vorticies of unit strength. Between b/B = 0.73 and b/B = 0.85, the upwash increases very rapidly and thus explains the rapidly decreasing values of C_{L_f}/C_{L_t} in figure 4.21. The extreme magnitude of upwash for b/B = 0.85 could possibly have caused the break in the C_{L_f}/C_{L_t} curve for $\alpha = 14$ degrees. The results for the variation of wing span to tunnel diameter on C_{L_f}/C_{L_t} show that the wall induced lift on the wing is less than 10% of the lift in free air when b/B ratios are less than 0.60. The wall induce lift rapidly increases from approximately 10% to approximately 18% as b/B increases from 0.60 to 0.80. Therefore, it seems that b/B ratios less than 0.60 are preferable.

Chapter 5

Summary

The separated flow vortex panel method implemented for the analysis of tunnel wall effects was successfully used to approximate the complex separated flow conditions associated with swept, tapered wings of moderate aspect ratio. Modeling in free air and a wind tunnel environment was carried out for an aspect ratio three wing with a taper ratio of 0.025, leading edge sweep of 45 degrees and a NACA 64A005 airfoil section. An experimental test of the wing was carried out in a wind tunnel with a ratio of wing span to tunnel span (b/B) of 0.73 and served as a basis of comparison for the panel method. Results of the modeling show the following.

- For angles of attack where less than 50% of the wing surface experienced separation, C_{L_t} determined from the panel method was within 2% of the values obtained for C_{L_t} from the integration of the experimental wing surface pressures.
- For angles of attack where more than 50% of the wing surface experienced separation, the C_{L_t} values determined from the panel method underpredicted, by approximately 6%, the experimental values of C_{L_t}.
- For the angles of attack tested in the experiment and a tunnel model with b/B = 0.73, C_{L_f}/C_{L_t} is approximately equal to 0.86.

The behavior of the vortex panel method was shown to be sensitive to the ratio of the number of streamwise panels along the wing semi-span to the wing span ($\frac{ns}{b}$). For

$\frac{ns}{b}$ values greater than unity, paneling discontinuities at such locations as the outboard streamwise strips on the wing surface and the strips of the separated wake, resulted in induced velocities on panel control points. These "tip effects" are due to a vertical spacing between the edges of adjacent panels. For attached flows, sheet souce distributions on the wing surface compensate for these induced velocities at the wing tip. For separated flows, however, the discontinuity of the free vortex sheets presently limits modeling to $\frac{ns}{b}$ values of approximately unity. In order to model with higher values of $\frac{ns}{b}$, it seems that either a continuous free vortex sheet must be modeled or the concentrated vorticity trails that follow the edges of streamwise strips must be moved to locations vertically intermediate between the edges of the discontinuous streamwise strips.

When modeling separated flows with consideration of the limits on $\frac{ns}{b}$, the panel method was shown to be in good agreement with experimental results, and thus further development of the model with the purpose of reducing or eliminating the discontinuous modeling of free vortex sheets promises to provide even better agreement with actual flow results.

Bibliography

[1] J.H. Burns. *A Three-Dimensional Correction Panel Method for Swept Tapered Airfoils with Separation.* Master's thesis, Massachusetts Institute of Technology, 1988.

[2] J.F. Campbell. *Effects of Spanwise Blowing on the Pressure Field and Vortex-Lift Characteristics of a 44 deg. Swept Trapezoidal Wing.* Technical Report NASA-TN-D-7907, National Aeronautics and Space Administration, June 1975.

[3] T. Cebeci, G.J. Mosinskis, and Smith A.M.O. "The Calculation of Separation Points in Incompressible Turbulent Flows." *Journal of Aircraft*, 9(9):618–624, September 1972.

[4] F.A. Dvorak and B. Maskew. "The Prediction of Clmax Using a Separated Flow Model." *Journal of American Helicopter Society*, April 1974.

[5] F.A. Dvorak, B. Maskew, and B.M. Rao. *Prediction of Aerodynamic Characteristics of Fighter Wings at High Lift.* Technical Report ONR-CR215-258-1, Office of Naval Research, 1979.

[6] Woodward F.A. *An Improved Method for the Aerodynamic Analysis of Wing-Body-Tail Configurations in Subsonic and Supersonic Flow Part I - Theory and Application.* Technical Report NASA CR-2228, Pt. I, National Aeronautics and Space Administration, 1973.

[7] B.R. Gilmer and D.R. Bristow. "Analysis of Stalled Airfoils by Simultaneous Perturbations to Viscous and Inviscid Equations." *AIAA Journal*, (AIAA 81-1239R):1160–1166, September 1982.

[8] M.L. Henderson. *Two-Dimensional Separated Wake Modeling and its Use to Predict Maximum Sectin Lift Coefficient.* Technical Report AIAA-78-156, American Institute of Aeronautics and Astronautics, 1978.

[9] J.L. Hess and A.M.O. Smith. "Calculation of Potential Flow About Arbitrary Bodies." *Progress in Aerospace Sciences*, 8:1–138, 1966.

[10] H.W.M. Hoeijmakers. "Panel Methods in Aerodynamics; Some Highlights." In *Panel Methods in Fluid Mechanics with Emphasis on Aerodynamics*, 1987.

[11] D.R. Holt and B. Hunt. *The Use of Panel Methods for the Evaluation of Subsonic Wall Interference.* Technical Report AGARD-CP-335, Advisory Group for Aerospace Research and Development, 1983.

[12] C.D. Kolbe and F.W. Boltz. *The Forces and Pressure Distributions at Subsonic Speeds on a Plane Wing Having 45 deg. of Sweepback, an Aspect Ratio of 3, and a Taper Ratio of 0.5.* Technical Report NACA-RM-A51G31, Ames Aeronautical Laboratory, Moffet Field, CA., October 1951.

[13] A.M. Kuethe and C.-Y. Chow. *Foundations of Aerodynamics.* John Wiley and Sons, Inc., 1986.

[14] H. Lamb. *Hydrodynamics.* Dover Publications, 1945.

[15] K.D. Lee. "Numerical Simulation of the Wind Tunnel Environment by a Panel Method." *AIAA Journal*, (AIAA 80-0419R):471–475, April 1981.

[16] B.W. McCormick. *Aerodynamics, Astronautics, and Flight Mechanics.* John Wiley and Sons, Inc., 1979.

[17] J. Moran. *An Introduction to Theoretical and Computational Aerodynamics.* John Wiley and Sons, Inc., 1984.

[18] A. Pope and W.H. Rae. *Low-Speed Wind Tunnel Testing.* John Wiley and Sons, Inc., 1984.

[19] B.S. Stratford. "The Prediction of Separation of the Turbulent Boundary Layer." *Journal of Fluid Mechanics*, 5:1–16, 1959.

[20] F.M. White. *Viscous Fluid Flow.* McGraw-Hill Book Company, 1974.

upper surface		*lower surface*	
chordwise tap number	x'/c	chordwise tap number	x'/c
0	0.000	0	0.000
1	0.005		
2	0.015	25	0.015
3	0.025		
4	0.040	26	0.050
5	0.070		
6	0.100	27	0.100
7	0.150		
8	0.200	28	0.200
9	0.250		
10	0.300	29	0.300
11	0.350		
12	0.400	30	0.400
13	0.450		
14	0.500	31	0.500
15	0.550		
16	0.600	32	0.600
17	0.650		
18	0.700	33	0.700
19	0.750		
20	0.800	34	0.800
21	0.850		
22	0.900	35	0.900
23	0.950	36	0.950
24	0.980		

Table 2.1: Chordwise distribution of wing surface pressure taps

distance from leading edge of ground board (in.)		
upper surface side	centerline	lower surface side
3.75	3.75	3.75
2.0	2.0	2.0
0.85	0.85	0.85
0.0	0.0	0.0
0.85	0.85	0.85
2.0	2.0	2.0
3.75	3.75	3.75
11.25	11.25	11.25
	18.0	
23.25		23.25
	27.5	
35.0		35.0
47.0	W	47.0
59.0	I	59.0
71.0	N	71.0
83.0	G	83.0
	91.0	
95.5		95.5
	103.0	
107.5		107.5
120.0	120.0	120.0
138.5	138.5	138.5
156.5	156.5	156.5

- figure 2.7 illustrates ground board pressure tap locations
- ground board tap locations for the turntable vary with wing angle of attack
- tap locations presented above are for the wing at 0 deg. angle of attack
- root chord locations(C_r = 51.2") - leading edge 31.8" - trailing edge 83.0"

Table 2.2: Ground board pressure tap locations

δ_{le}	δ_{te}	Re $10^6/ft$	M	$b.l.$ $trip$	$\alpha_{geometric}$	$\alpha_{corrected}$	C_L	C_D	$C_{D_{corrected}}$
0	0	1.0	0.15	N	-8	-8.8	-0.479	0.057	0.064
0	0	1.0	0.15	N	-4	-4.3	-0.205	0.016	0.017
0	0	1.0	0.15	N	0	0.1	0.039	0.006	0.006
0	0	1.0	0.15	N	2	2.3	0.161	0.007	0.008
0	0	1.0	0.15	N	4	4.5	0.295	0.014	0.017
0	0	1.0	0.15	N	6	6.7	0.428	0.033	0.038
0	0	1.0	0.15	N	8	8.9	0.568	0.064	0.073
0	0	1.0	0.15	N	10	11.1	0.687	0.104	0.118
0	0	1.0	0.15	N	14	15.4	0.861	0.198	0.219
0	0	1.3	0.19	N	-8	-8.8	-0.499	0.058	0.065
0	0	1.3	0.19	N	-4	-4.4	-0.224	0.016	0.017
0	0	1.3	0.19	N	0	0.0	0.011	0.006	0.006
0	0	1.3	0.19	N	2	2.2	0.132	0.007	0.008
0	0	1.3	0.19	N	4	4.4	0.263	0.012	0.014
0	0	1.3	0.19	N	6	6.7	0.406	0.027	0.032
0	0	1.3	0.19	N	8	8.9	0.552	0.061	0.070
0	0	1.3	0.19	N	10	11.1	0.671	0.099	0.112
0	0	1.3	0.19	N	14	15.4	0.861	0.197	0.218
0	0	1.0	0.15	Y	-8	-8.8	-0.472	0.056	0.062
0	0	1.0	0.15	Y	-4	-4.3	-0.202	0.016	0.017
0	0	1.0	0.15	Y	0	0.0	0.029	0.006	0.006
0	0	1.0	0.15	Y	2	2.3	0.161	0.007	0.008
0	0	1.0	0.15	Y	4	4.5	0.286	0.015	0.017
0	0	1.0	0.15	Y	6	6.7	0.423	0.030	0.035
0	0	1.0	0.15	Y	8	8.9	0.564	0.063	0.072
0	0	1.0	0.15	Y	10	11.1	0.682	0.102	0.115
0	0	1.0	0.15	Y	14	15.4	0.862	0.196	0.218
0	0	1.3	0.19	Y	-8	-8.8	-0.498	0.057	0.064
0	0	1.3	0.19	Y	-4	-4.4	-0.227	0.017	0.018
0	0	1.3	0.19	Y	0	0.0	0.015	0.007	0.007
0	0	1.3	0.19	Y	2	2.2	0.137	0.007	0.008
0	0	1.3	0.19	Y	4	4.4	0.264	0.014	0.016
0	0	1.3	0.19	Y	6	6.6	0.396	0.027	0.032
0	0	1.3	0.19	Y	8	8.9	0.553	0.060	0.069
0	0	1.3	0.19	Y	10	11.1	0.677	0.100	0.113
0	0	1.3	0.19	Y	14	15.4	0.859	0.197	0.218

Table 2.3: Experimental lift and drag coefficients

δ_{le}	δ_{te}	Re $10^6/ft$	M	$b.l.$ $trip$	$\alpha_{geometric}$	$\alpha_{corrected}$	C_L	C_D	$C_{D_{corrected}}$
20	30	1.0	0.15	N	-8	-7.7	0.211	0.112	0.113
20	30	1.0	0.15	N	-4	-3.2	0.500	0.082	0.089
20	30	1.0	0.15	N	0	1.2	0.716	0.092	0.107
20	30	1.0	0.15	N	2	3.3	0.809	0.102	0.121
20	30	1.0	0.15	N	4	5.5	0.907	0.116	0.140
20	30	1.0	0.15	N	6	7.6	1.002	0.137	0.166
20	30	1.0	0.15	N	8	9.8	1.117	0.170	0.206
20	30	1.0	0.15	N	10	11.9	1.156	0.232	0.271
20	30	1.0	0.15	N	14	16.0	1.248	0.311	0.356
20	30	1.3	0.19	N	-8	-7.7	0.204	0.118	0.119
20	30	1.3	0.19	N	-4	-3.2	0.497	0.089	0.096
20	30	1.3	0.19	N	0	1.2	0.735	0.098	0.114
20	30	1.3	0.19	N	2	3.3	0.820	0.108	0.127
20	30	1.3	0.19	N	4	5.5	0.923	0.121	0.146
20	30	1.3	0.19	N	6	7.6	1.006	0.141	0.170
20	30	1.3	0.19	N	8	9.8	1.107	0.166	0.202
20	30	1.3	0.19	N	10	11.9	1.176	0.236	0.276
20	30	1.3	0.19	N	14	16.1	1.259	0.315	0.361
20	30	1.0	0.15	Y	-8	-7.7	0.171	0.122	0.123
20	30	1.0	0.15	Y	-4	-3.3	0.450	0.094	0.100
20	30	1.0	0.15	Y	0	1.1	0.691	0.098	0.112
20	30	1.0	0.15	Y	2	3.3	0.788	0.110	0.128
20	30	1.0	0.15	Y	4	5.5	0.890	0.124	0.147
20	30	1.0	0.15	Y	6	7.6	0.994	0.144	0.173
20	30	1.0	0.15	Y	8	9.8	1.108	0.173	0.209
20	30	1.0	0.15	Y	10	11.9	1.162	0.238	0.277
20	30	1.0	0.15	Y	14	16.1	1.259	0.315	0.361
20	30	1.3	0.19	Y	-8	-7.7	0.211	0.115	0.116
20	30	1.3	0.19	Y	-4	-3.2	0.497	0.089	0.096
20	30	1.3	0.19	Y	0	1.2	0.725	0.098	0.113
20	30	1.3	0.19	Y	2	3.3	0.820	0.109	0.128
20	30	1.3	0.19	Y	4	5.5	0.912	0.122	0.146
20	30	1.3	0.19	Y	6	7.6	1.000	0.141	0.170
20	30	1.3	0.19	Y	8	9.8	1.130	0.174	0.211
20	30	1.3	0.19	Y	10	11.9	1.174	0.235	0.275
20	30	1.3	0.19	Y	14	16.1	1.260	0.315	0.361

Table 2.4: Experimental lift and drag coefficients

δ_{le}	δ_{te}	Re $10^6/ft$	M	$b.l.$ $trip$	$\alpha_{geometric}$	$\alpha_{corrected}$	C_L	C_D	$C_{D_{corrected}}$
10	0	1.0	0.15	Y	-8	-8.8	-0.485	0.093	0.100
10	0	1.0	0.15	Y	-4	-4.4	-0.221	0.031	0.032
10	0	1.0	0.15	Y	0	0.0	0.028	0.009	0.009
10	0	1.0	0.15	Y	2	2.2	0.150	0.007	0.008
10	0	1.0	0.15	Y	4	4.5	0.278	0.009	0.011
10	0	1.0	0.15	Y	6	6.7	0.407	0.015	0.020
10	0	1.0	0.15	Y	8	8.9	0.544	0.029	0.038
10	0	1.0	0.15	Y	10	11.1	0.678	0.055	0.068
10	0	1.0	0.15	Y	14	15.4	0.860	0.135	0.156
10	10	1.0	0.15	Y	-8	-8.3	-0.176	0.054	0.055
10	10	1.0	0.15	Y	-4	-3.8	0.103	0.014	0.014
10	10	1.0	0.15	Y	0	0.6	0.341	0.015	0.018
10	10	1.0	0.15	Y	2	2.8	0.465	0.020	0.026
10	10	1.0	0.15	Y	4	5.0	0.589	0.030	0.040
10	10	1.0	0.15	Y	6	7.2	0.715	0.046	0.061
10	10	1.0	0.15	Y	8	9.4	0.847	0.073	0.094
10	10	1.0	0.15	Y	10	11.5	0.933	0.113	0.138
10	10	1.0	0.15	Y	14	15.7	1.038	0.203	0.234
0	10	1.0	0.15	Y	-8	-8.2	-0.138	0.020	0.021
0	10	1.0	0.15	Y	-4	-3.8	0.112	0.011	0.011
0	10	1.0	0.15	Y	0	0.6	0.345	0.015	0.018
0	10	1.0	0.15	Y	2	2.8	0.470	0.023	0.029
0	10	1.0	0.15	Y	4	5.0	0.594	0.037	0.047
0	10	1.0	0.15	Y	6	7.2	0.719	0.066	0.081
0	10	1.0	0.15	Y	8	9.3	0.824	0.108	0.128
0	10	1.0	0.15	Y	10	11.4	0.888	0.155	0.178
0	10	1.0	0.15	Y	14	15.6	0.996	0.254	0.283
0	30	1.0	0.15	Y	-8	-7.4	0.370	0.061	0.065
0	30	1.0	0.15	Y	-4	-3.1	0.562	0.076	0.085
0	30	1.0	0.15	Y	0	1.2	0.757	0.098	0.115
0	30	1.0	0.15	Y	2	3.4	0.866	0.120	0.142
0	30	1.0	0.15	Y	4	5.6	1.001	0.159	0.188
0	30	1.0	0.15	Y	6	7.8	1.092	0.212	0.247
0	30	1.0	0.15	Y	8	9.9	1.140	0.264	0.302
0	30	1.0	0.15	Y	10	11.9	1.158	0.312	0.351
0	30	1.0	0.15	Y	14	15.9	1.174	0.406	0.446

Table 2.5: Experimental lift and drag coefficients

δ_{le}	δ_{te}	Re $10^6/ft$	M	$b.l.$ $trip$	$\alpha_{geometric}$	$\alpha_{corrected}$	C_L	C_D	$C_{D_{corrected}}$
20	0	1.0	0.15	Y	-8	-8.8	-0.521	0.150	0.158
20	0	1.0	0.15	Y	-4	-4.4	-0.267	0.071	0.073
20	0	1.0	0.15	Y	0	0.0	0.004	0.020	0.020
20	0	1.0	0.15	Y	2	2.2	0.131	0.010	0.010
20	0	1.0	0.15	Y	4	4.4	0.253	0.010	0.012
20	0	1.0	0.15	Y	6	6.6	0.385	0.013	0.017
20	0	1.0	0.15	Y	8	8.8	0.521	0.022	0.030
20	0	1.0	0.15	Y	10	11.1	0.651	0.038	0.050
20	0	1.0	0.15	Y	14	15.4	0.860	0.097	0.118

Table 2.6: Experimental lift and drag coefficients

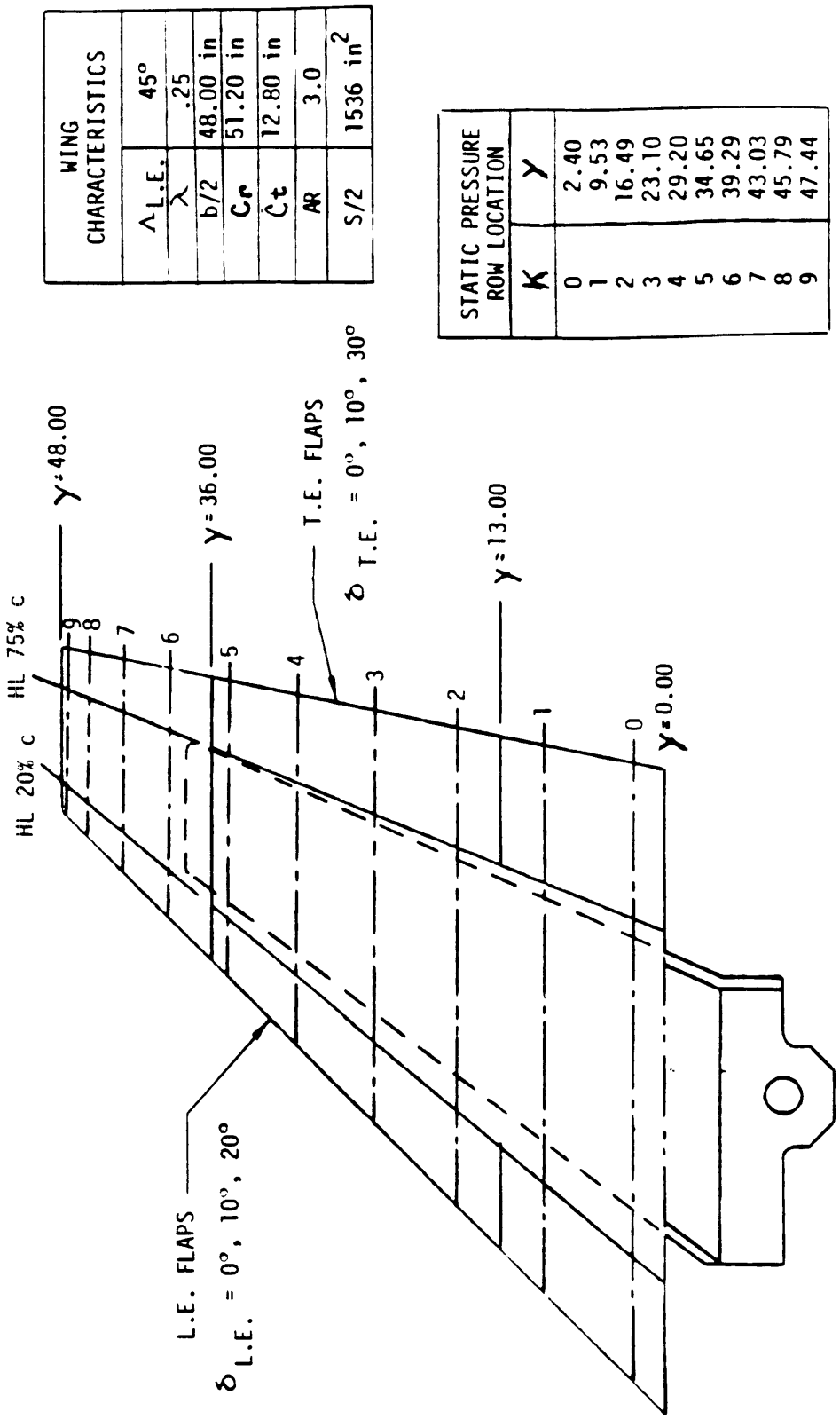

Figure 2.1: 45 degree leading edge sweep wing characteristics

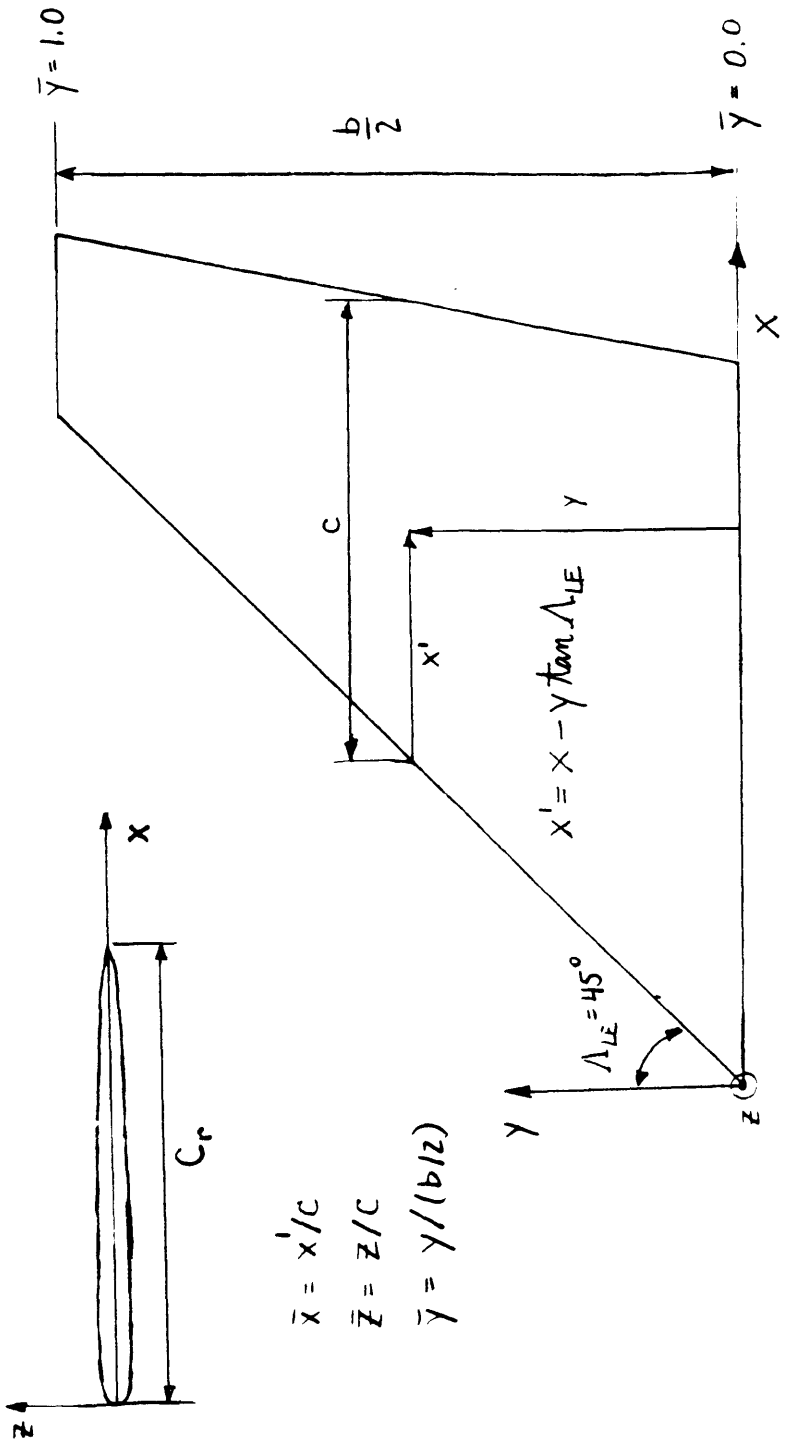

Figure 2.2: Experimental wing axis system - ($\alpha = 0$)

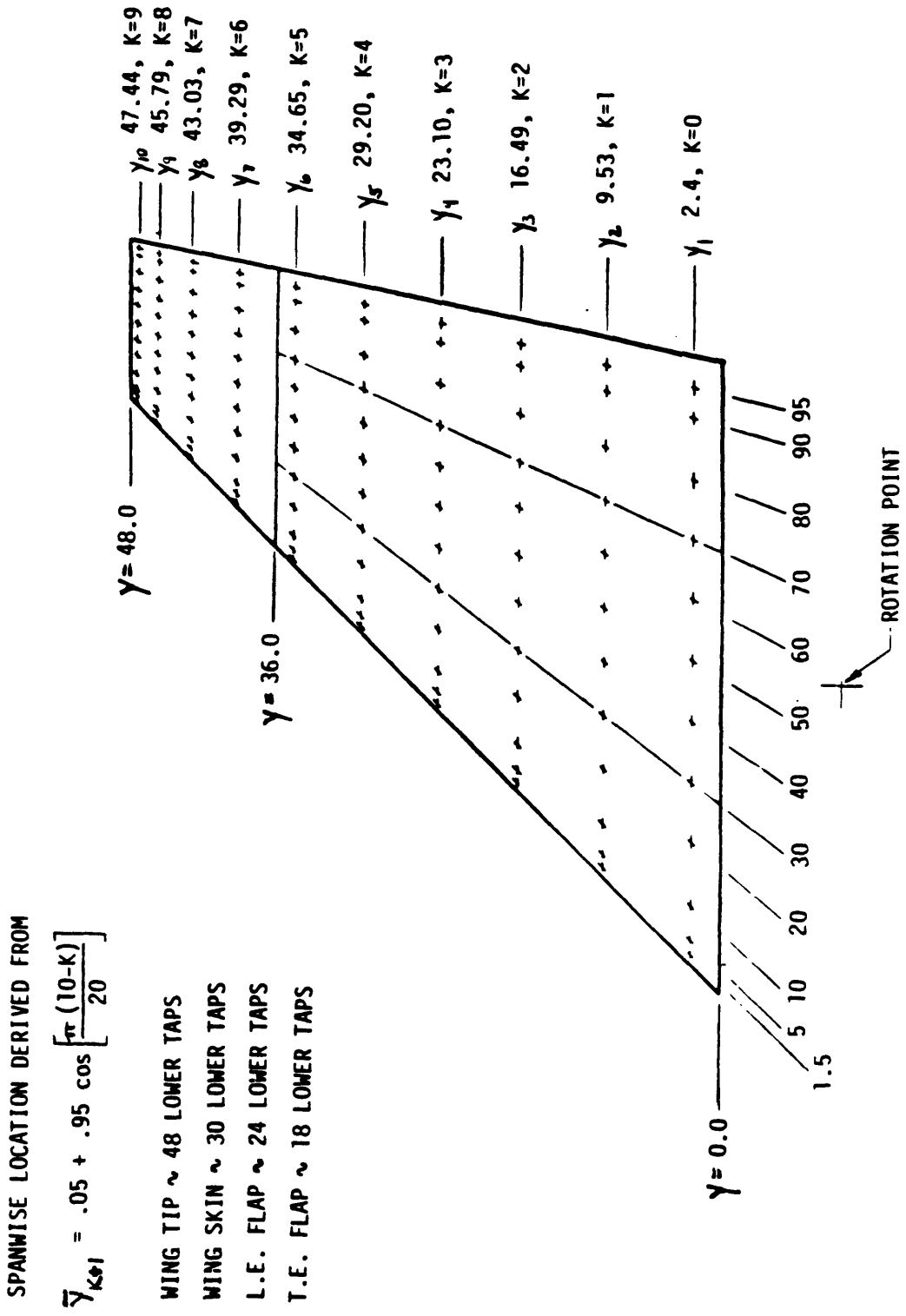

Figure 2.3: Wing pressure tap locations - upper surface

SPANWISE LOCATION DERIVED FROM

$$\bar{y}_{K+1} = .05 + .95 \cos\left[\frac{\pi (10-k)}{20}\right]$$

WING TIP ~ 100 UPPER TAPS

WING SKIN ~ 54 UPPER TAPS

L.E. FLAPS ~ 60 UPPER TAPS

T.E. FLAPS ~ 36 UPPER TAPS

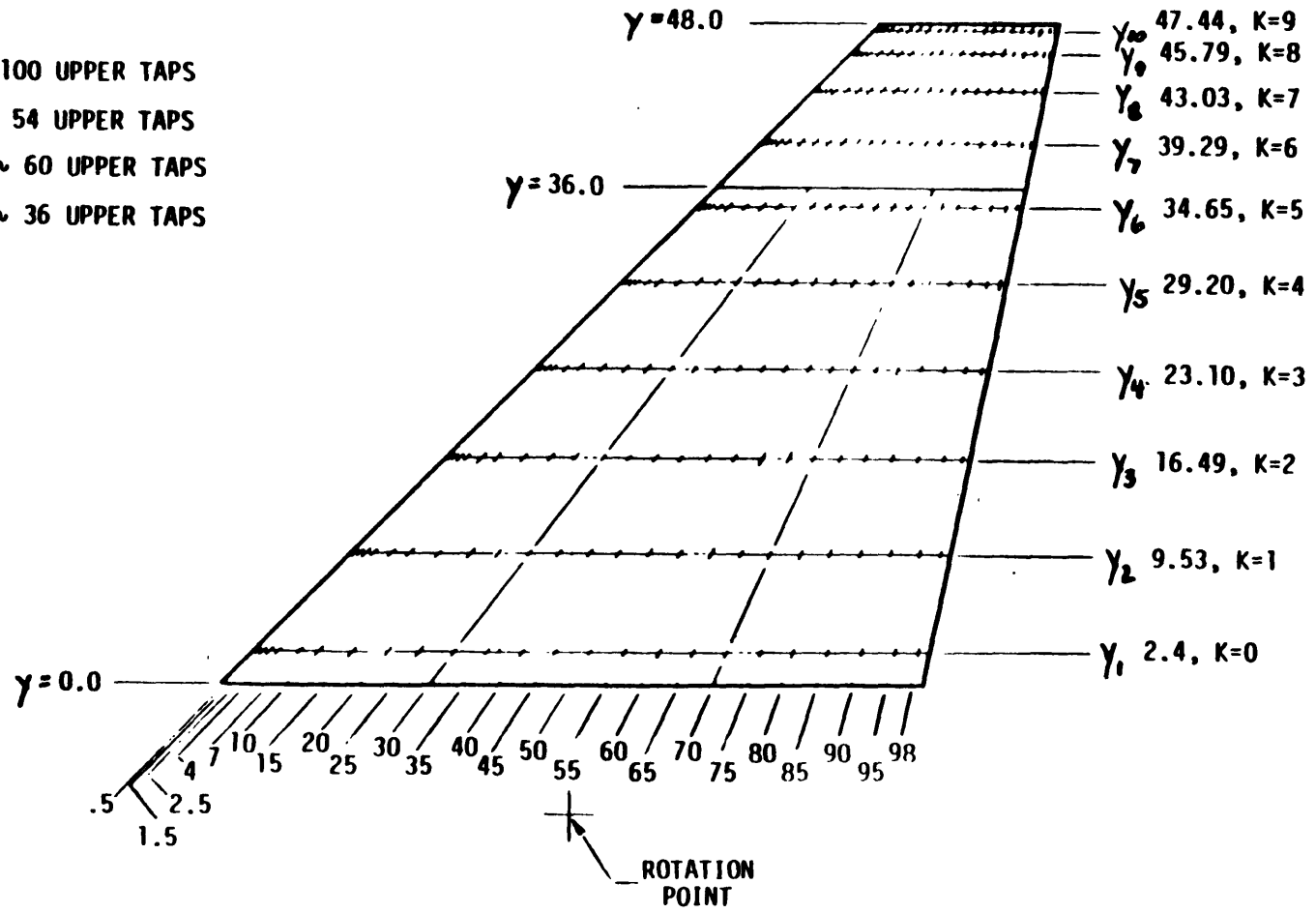

Figure 2.4: Wing pressure tap locations - lower surface

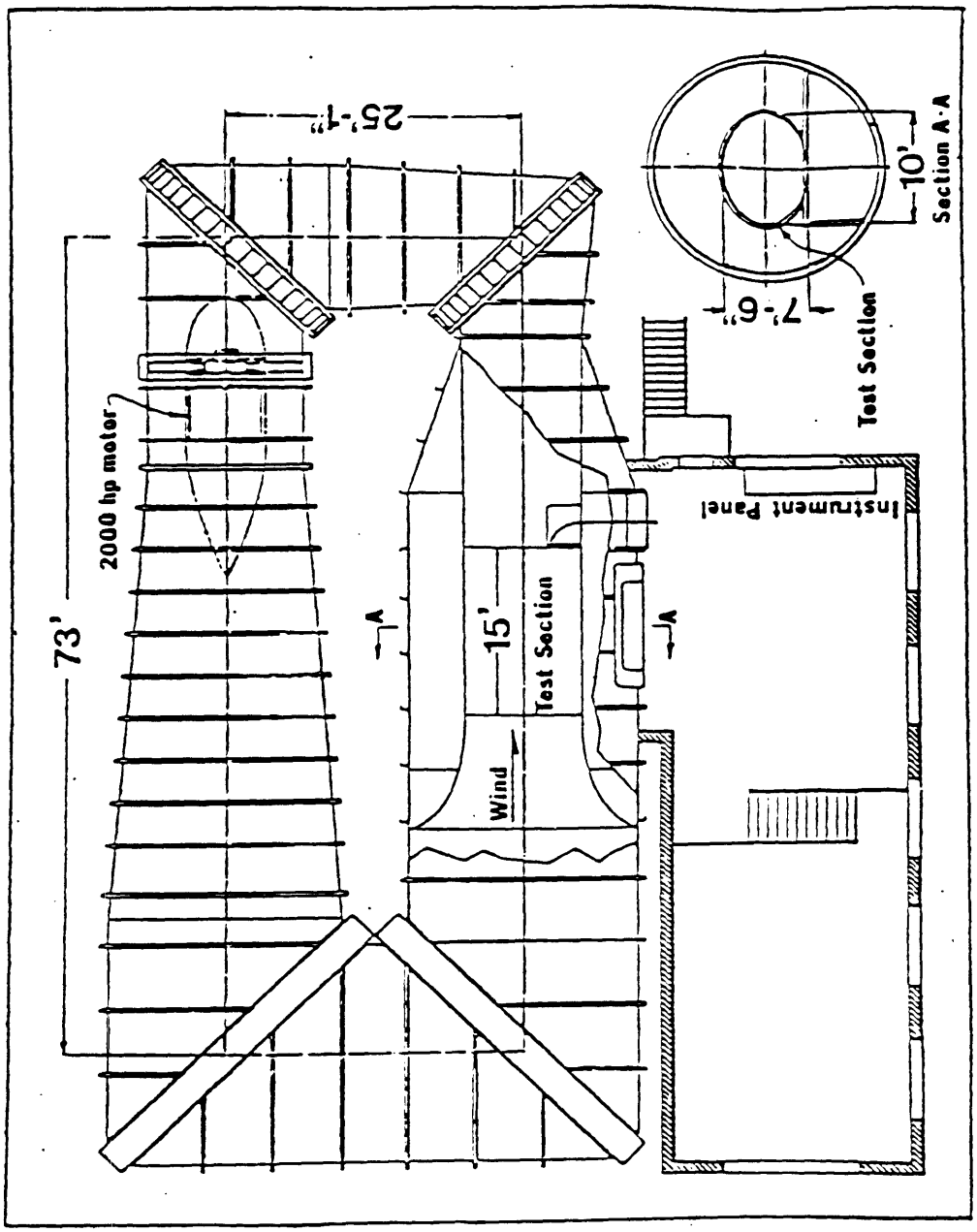

Figure 2.5: Schematic diagram of Wright Brothers Wind Tunnel

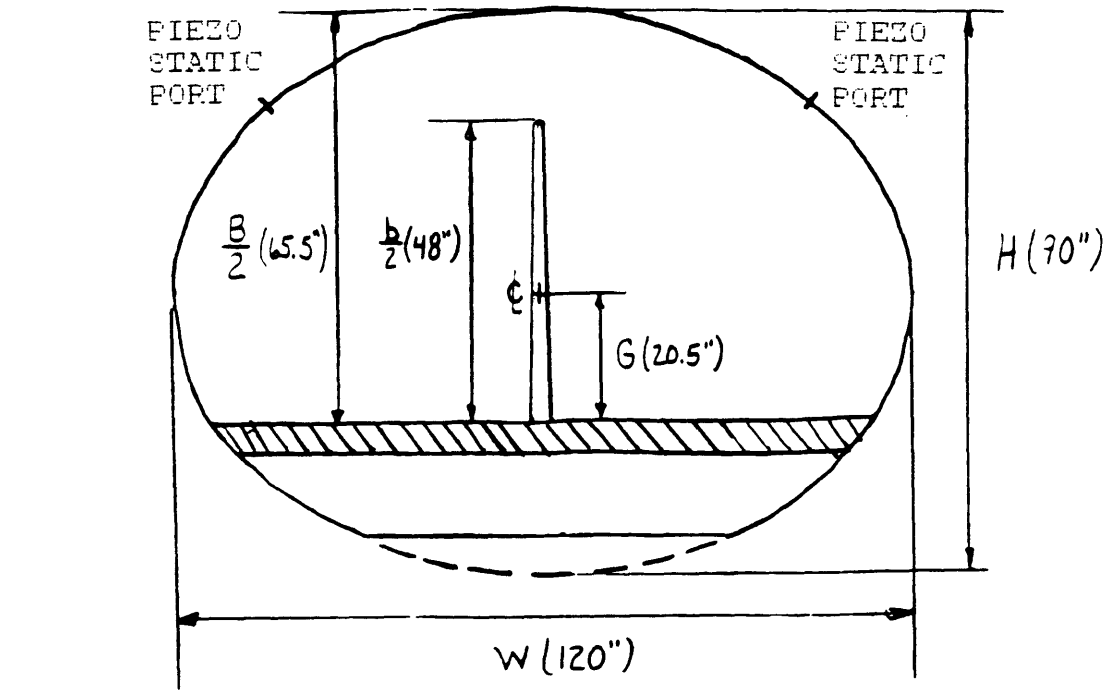

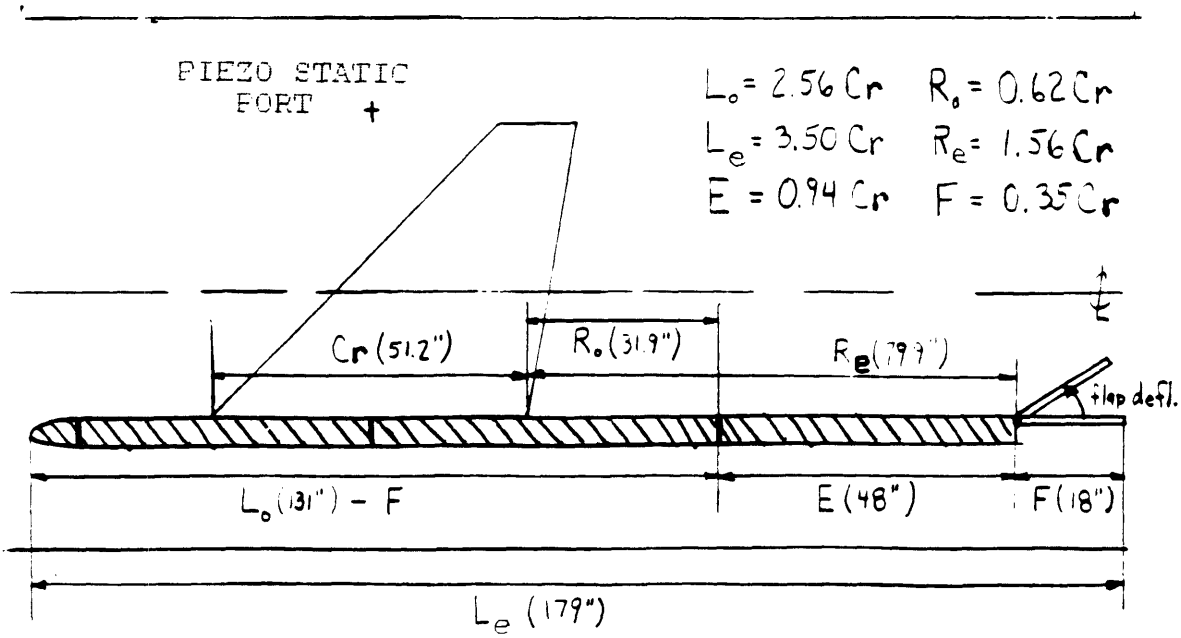

Figure 2.6: Dimensions of wing and reflecting plane installation

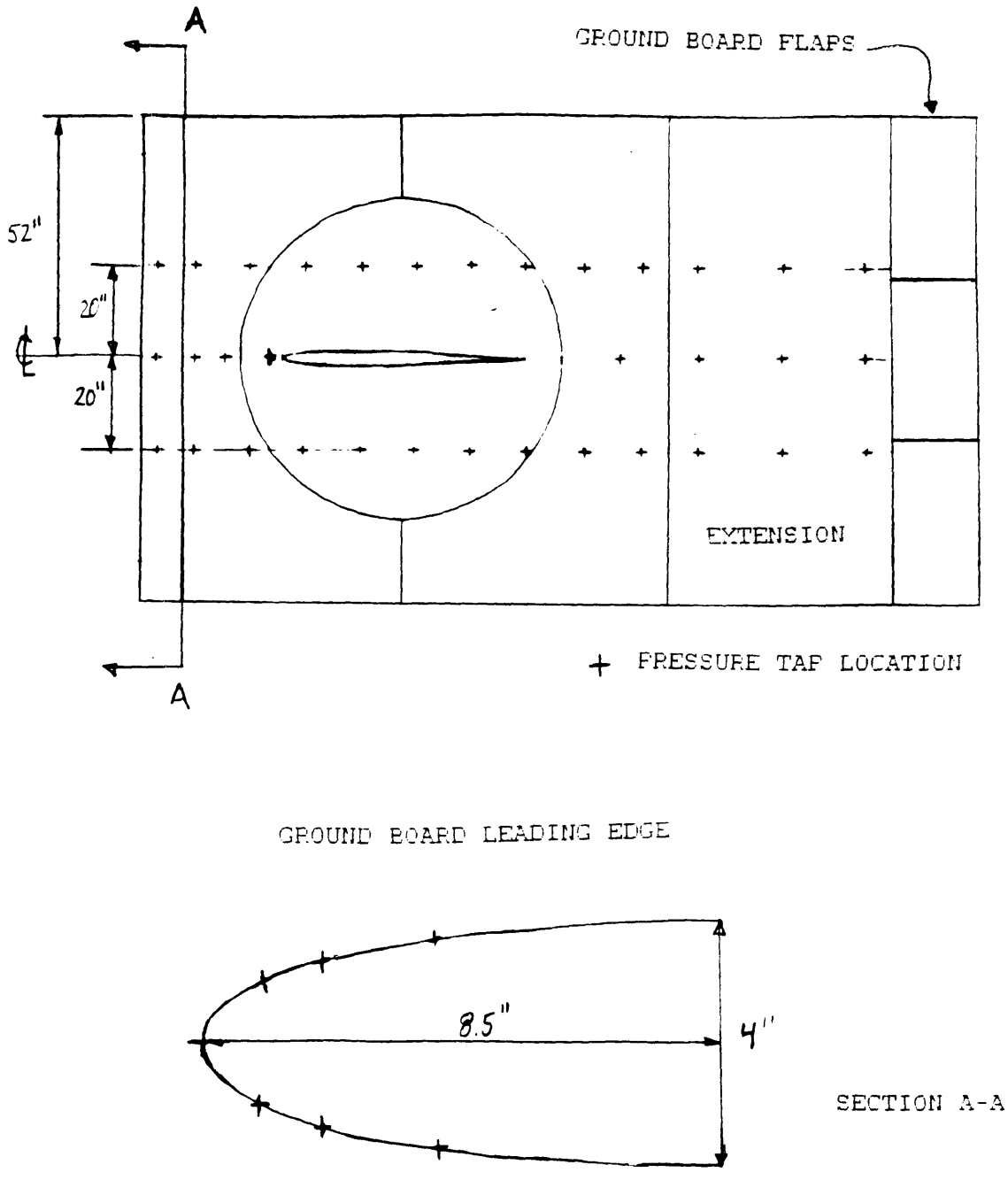

Figure 2.7: Pressure tap locations on reflecting plane surface

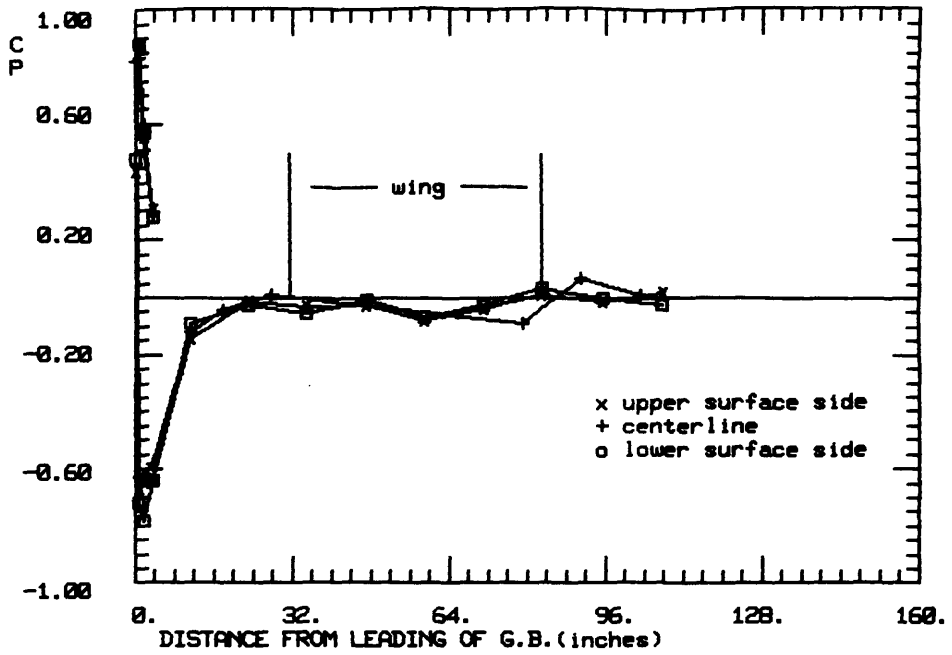

Figure 2.8: Ground board C_p's, short board, $\delta_{gbf} = 0$, $\alpha = 0$

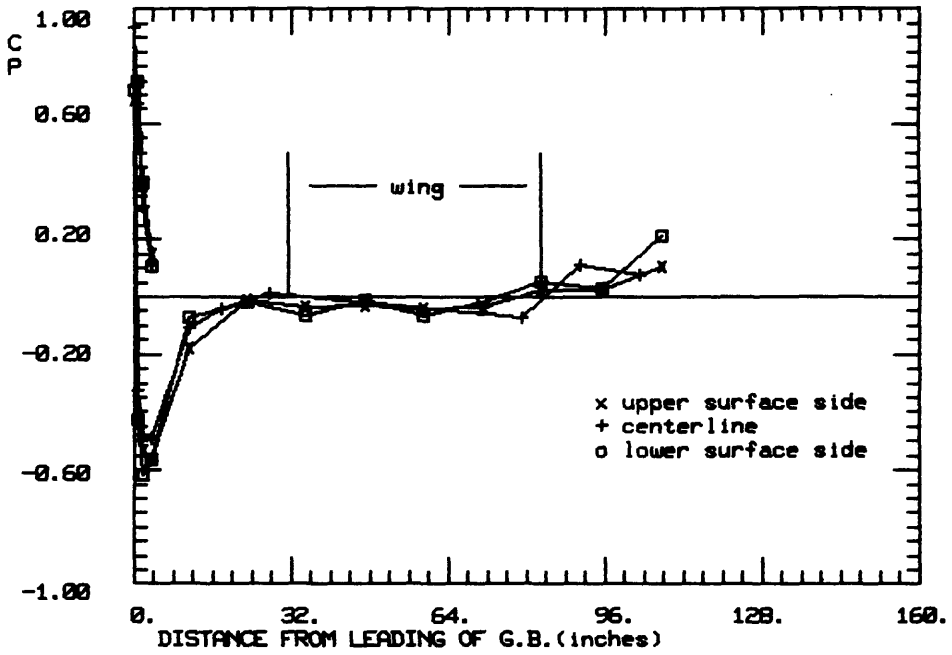

Figure 2.9: Ground board C_p's, short board, $\delta_{gbf} = 10$, $\alpha = 0$

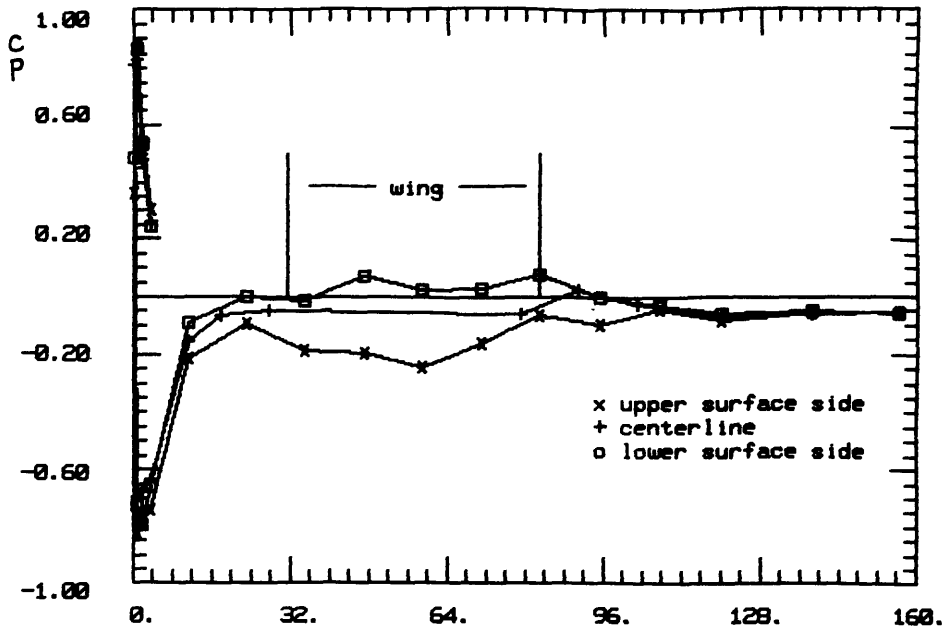

Figure 2.10: Ground board C_p's, long board, $\delta_{gbf} = 0$, $\alpha = 8$

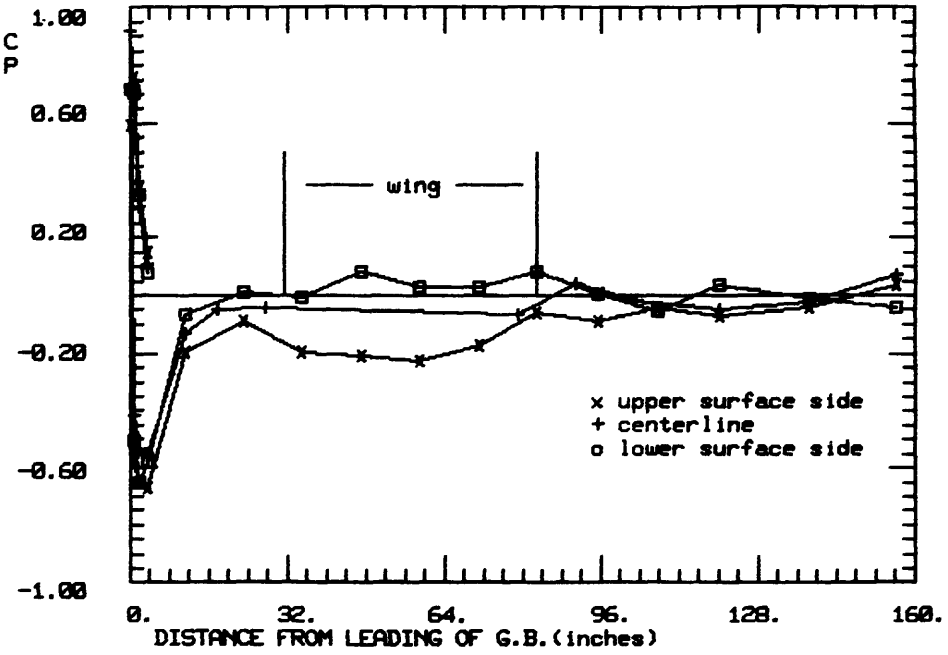

Figure 2.11: Ground board C_p's, long board, $\delta_{gbf} = 10$, $\alpha = 8$

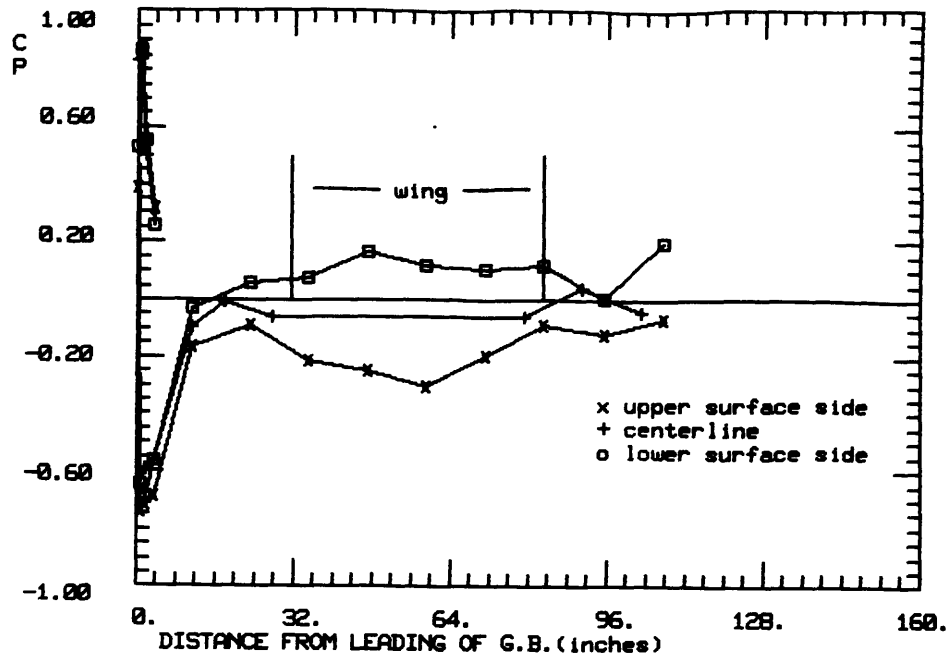

Figure 2.12: Ground board C_p's, short board, $\delta_{gbf} = 0$, $\alpha = 14$

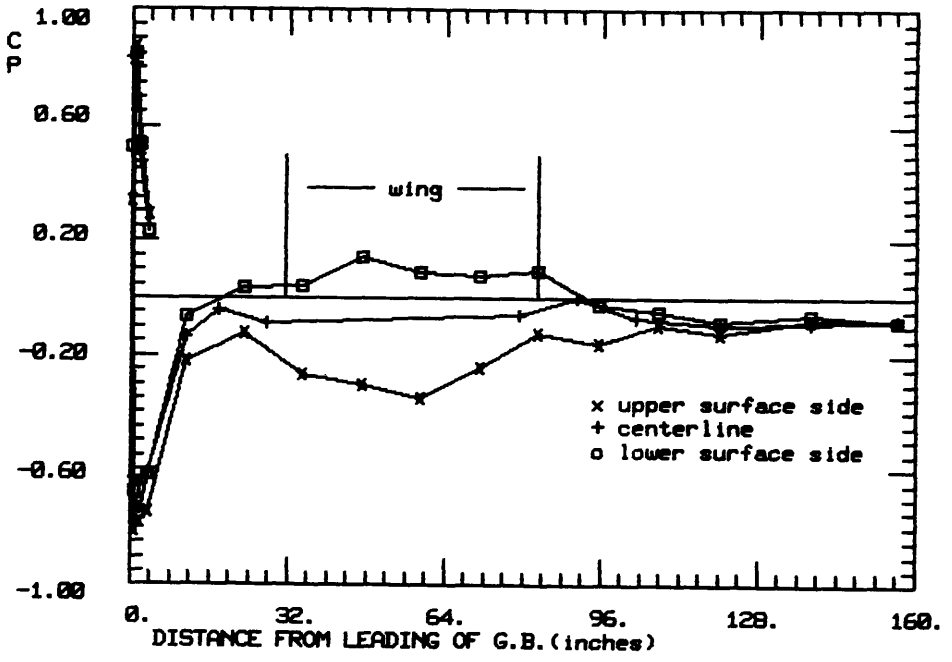

Figure 2.13: Ground board C_p's, long board, $\delta_{gbf} = 0$, $\alpha = 14$

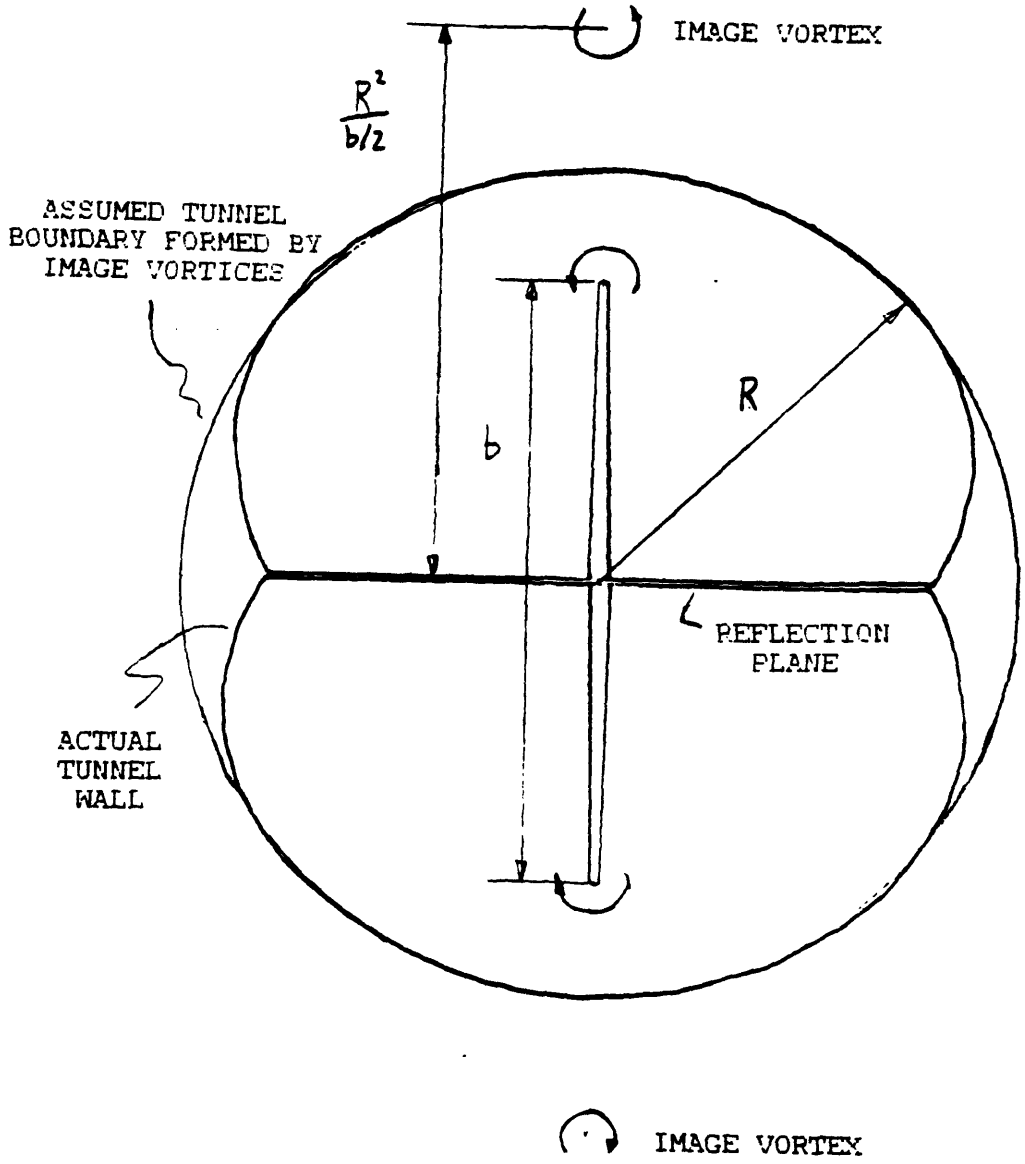

Figure 2.14: Assumed wing and tunnel configuration for wall effects

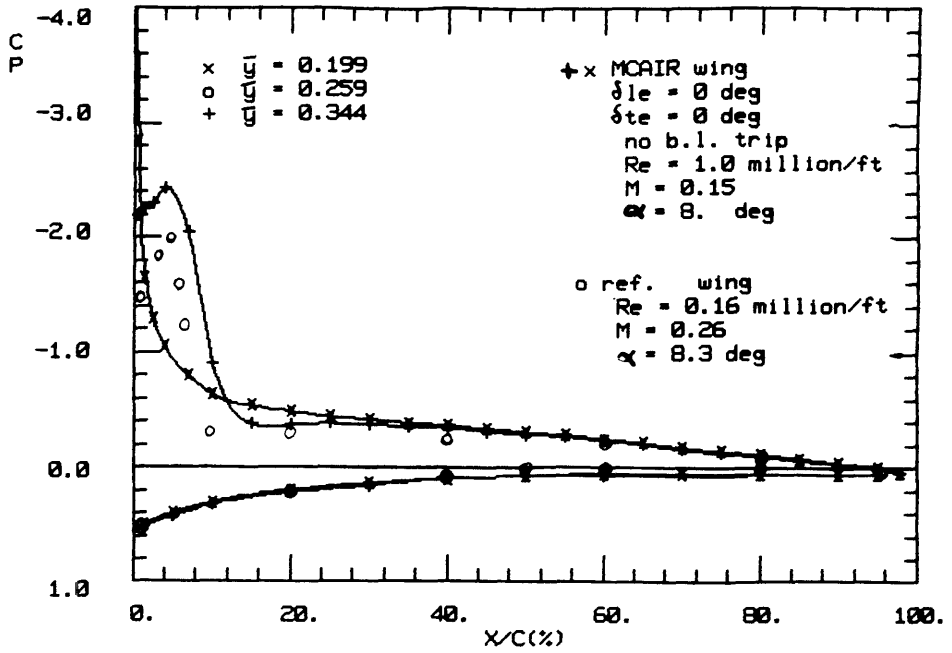

Figure 2.15: Experimental C_p comparisons, $\alpha = 8$, $\delta_{le,te} = 0$, $\bar{y} = 0.199$ and 0.344

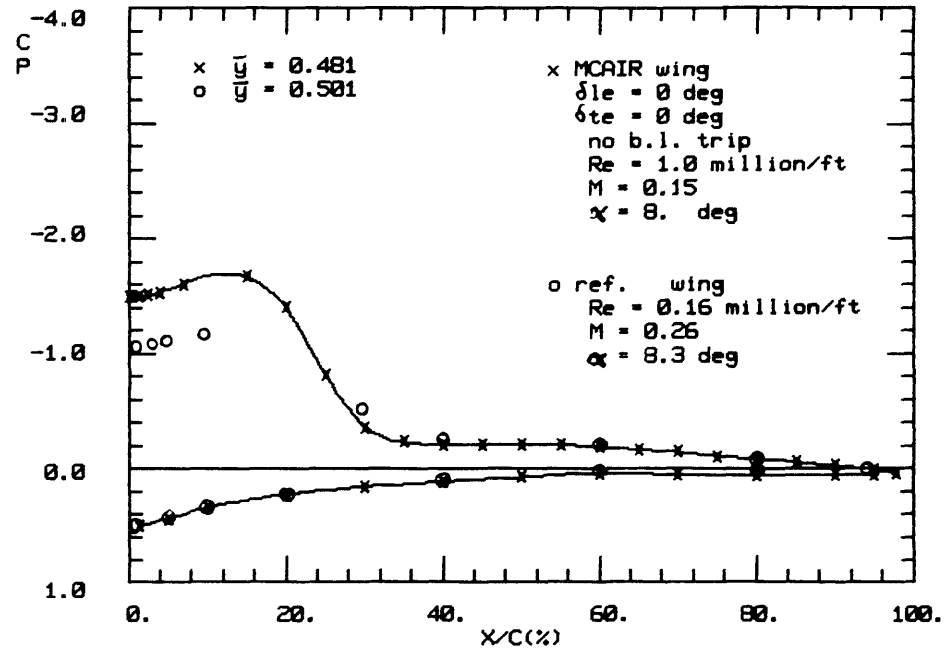

Figure 2.16: Experimental C_p comparisons, $\alpha = 8$, $\delta_{le,te} = 0$, $\bar{y} = 0.481$

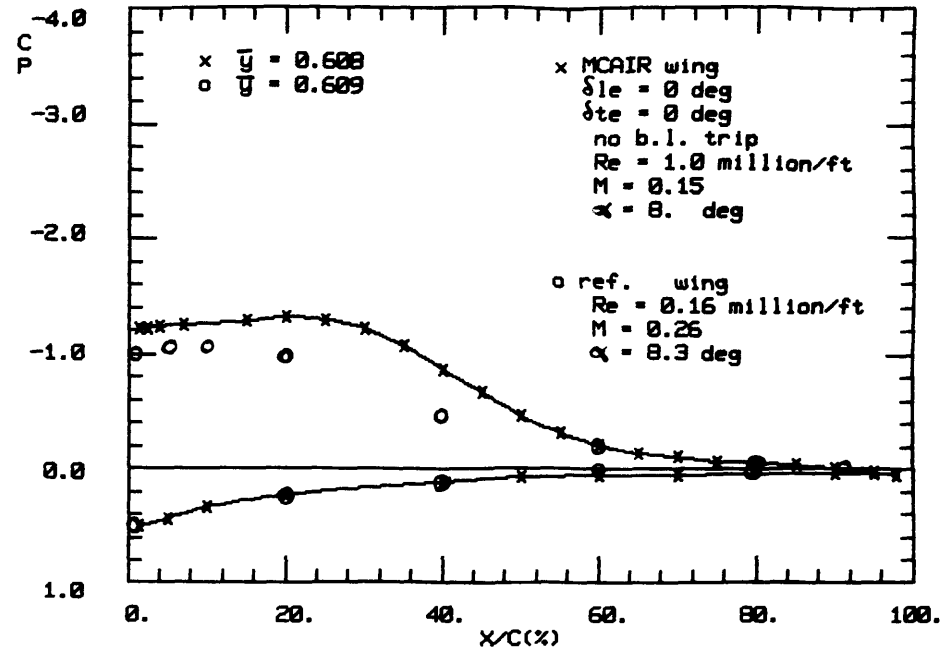

Figure 2.17: Experimental C_p comparisons, $\alpha = 8$, $\delta_{le,te} = 0$, $\bar{y} = 0.608$

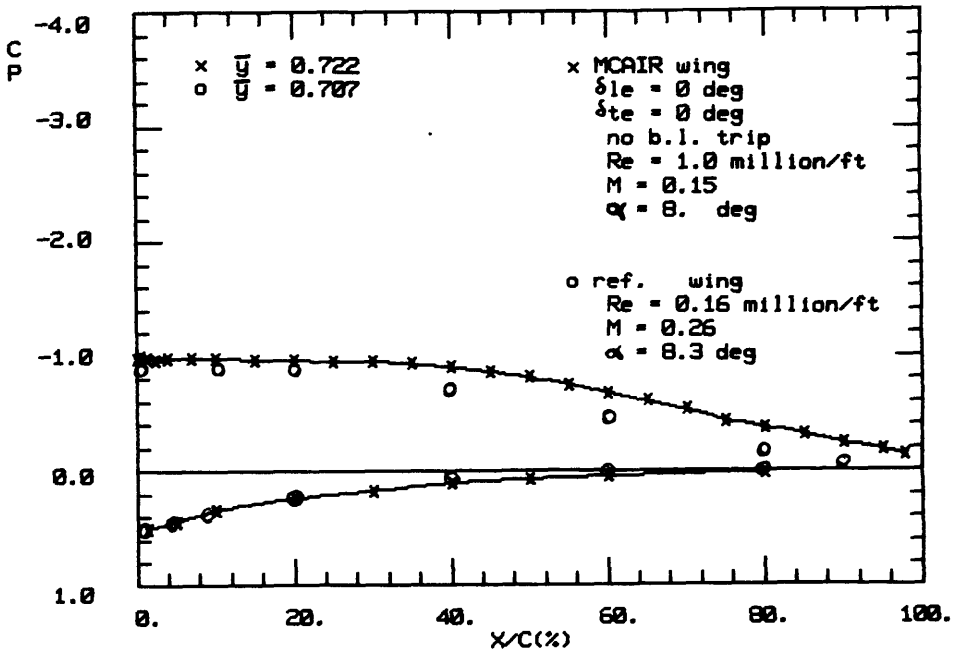

Figure 2.18: Experimental C_p comparisons, $\alpha = 8$, $\delta_{le,te} = 0$, $\bar{y} = 0.722$

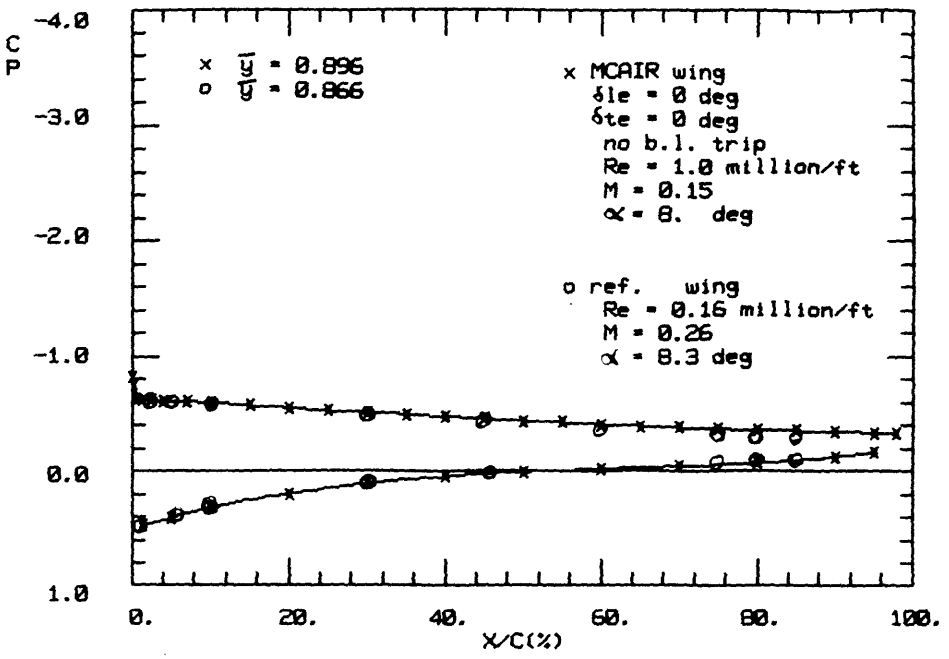

Figure 2.19: Experimental C_p comparisons, $\alpha = 8$, $\delta_{le,te} = 0$, $\bar{y} = 0.896$

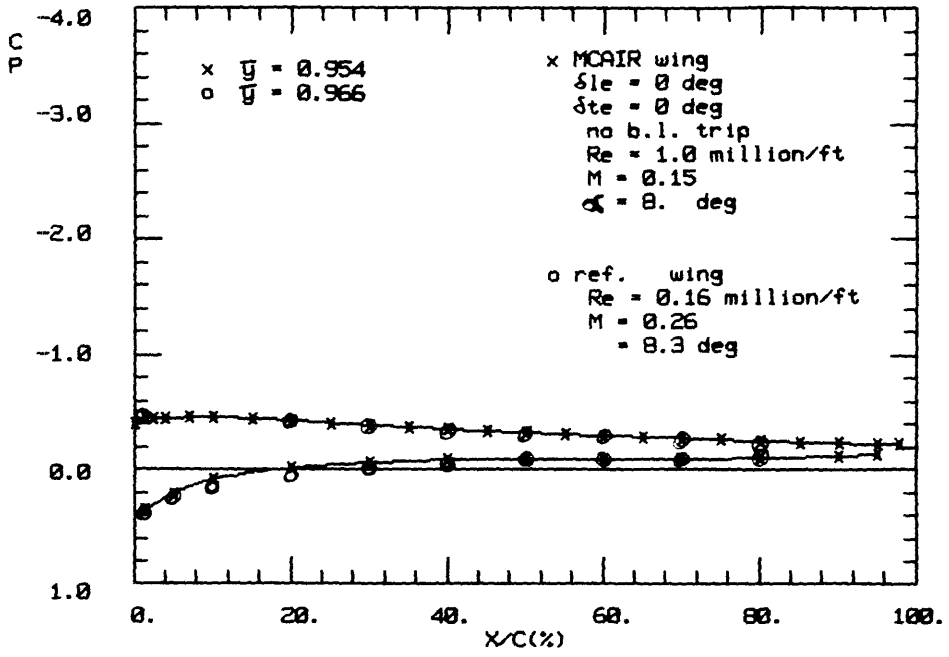

Figure 2.20: Experimental C_p comparisons, $\alpha = 8$, $\delta_{le,te} = 0$, $\bar{y} = 0.954$

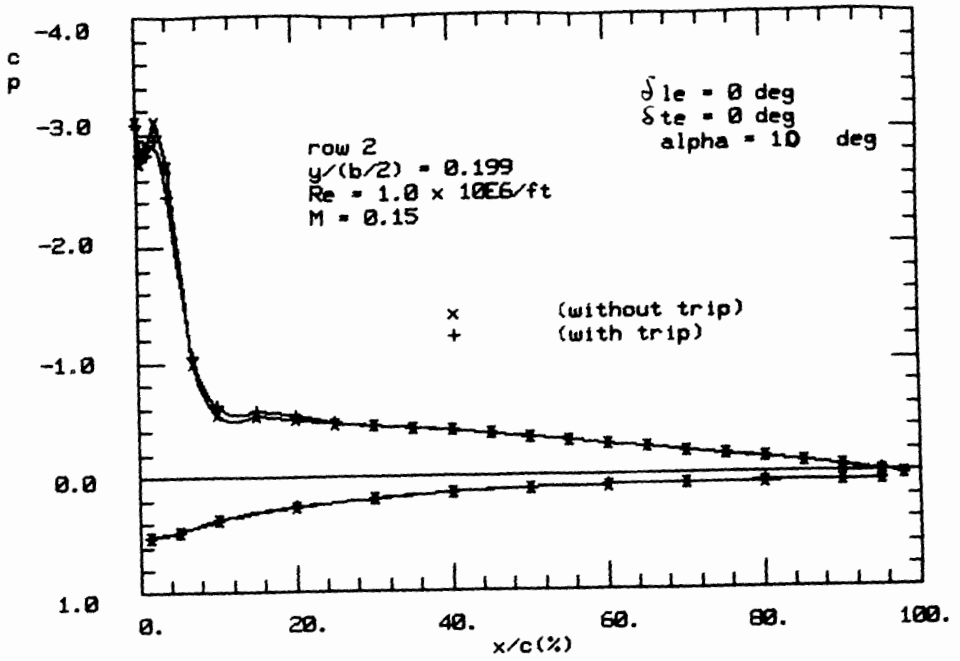

Figure 2.21: Re and trip effects on C_p, $\delta_{le} = 0$, $\delta_{te} = 0$, $\bar{y}$=0.199, Re=1.0 million/ft

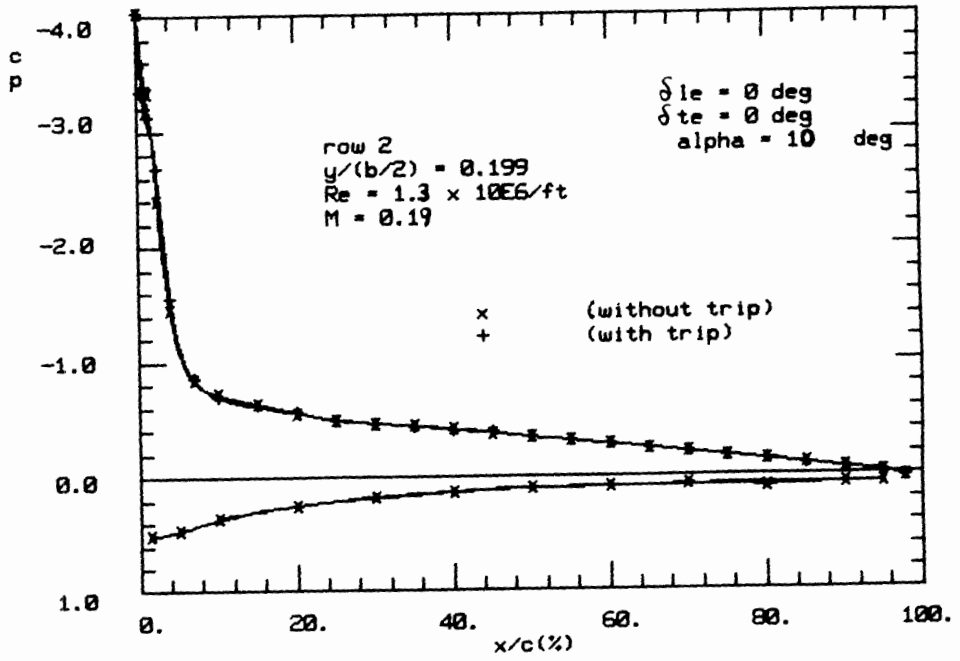

Figure 2.22: Re and trip effects on C_p, $\delta_{le} = 0$, $\delta_{te} = 0$, $\bar{y}$=0.199, Re=1.3 million/ft

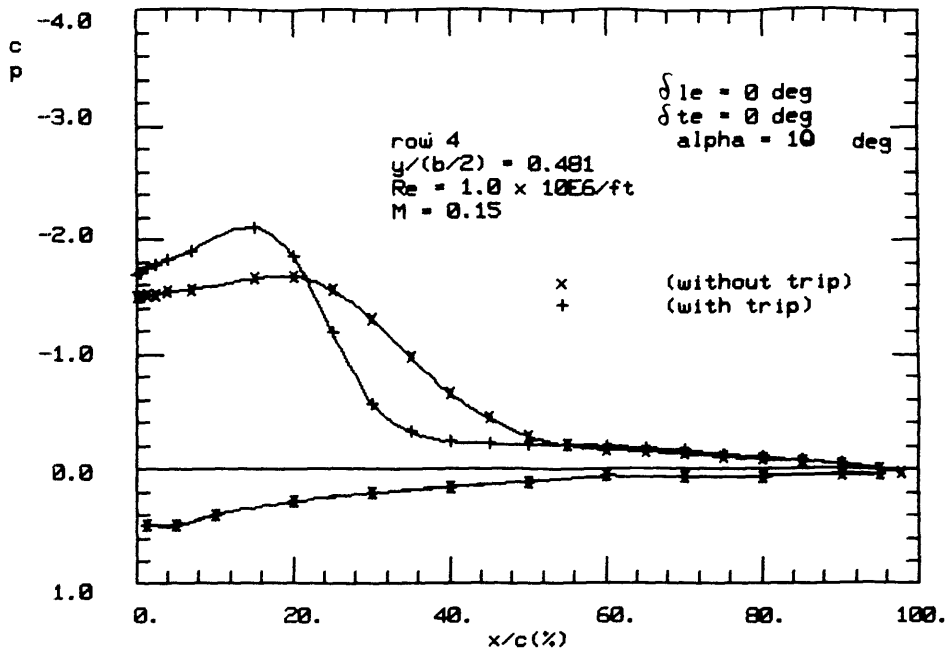

Figure 2.23: Re and trip effects on C_p, $\delta_{le} = 0$, $\delta_{te} = 0$, $\bar{y}$=0.481, Re=1.0 million/ft

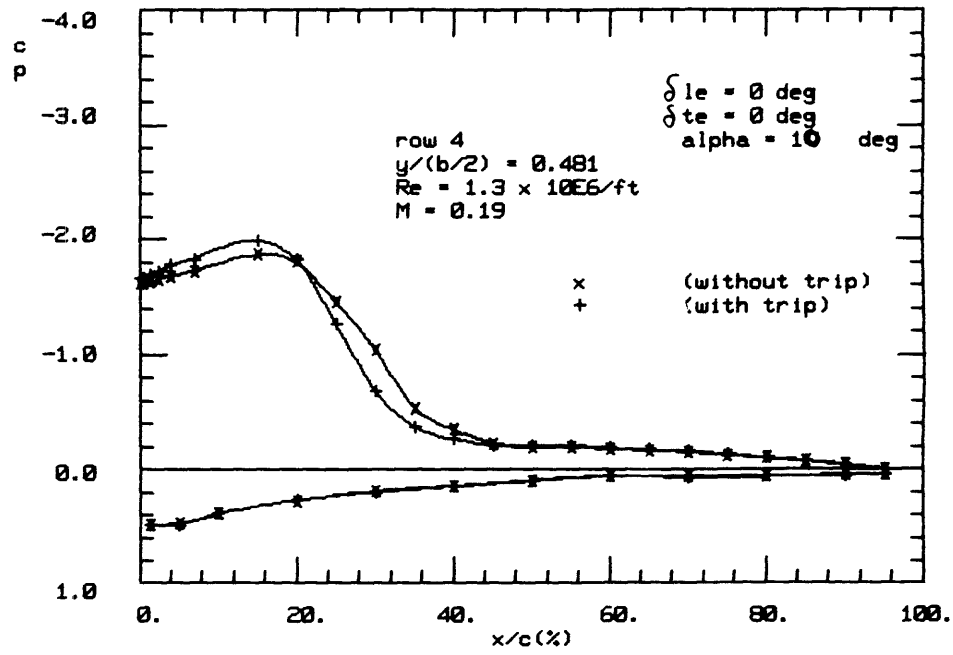

Figure 2.24: Re and trip effects on C_p, $\delta_{le} = 0$, $\delta_{te} = 0$, $\bar{y}$=0.481, Re=1.3 million/ft

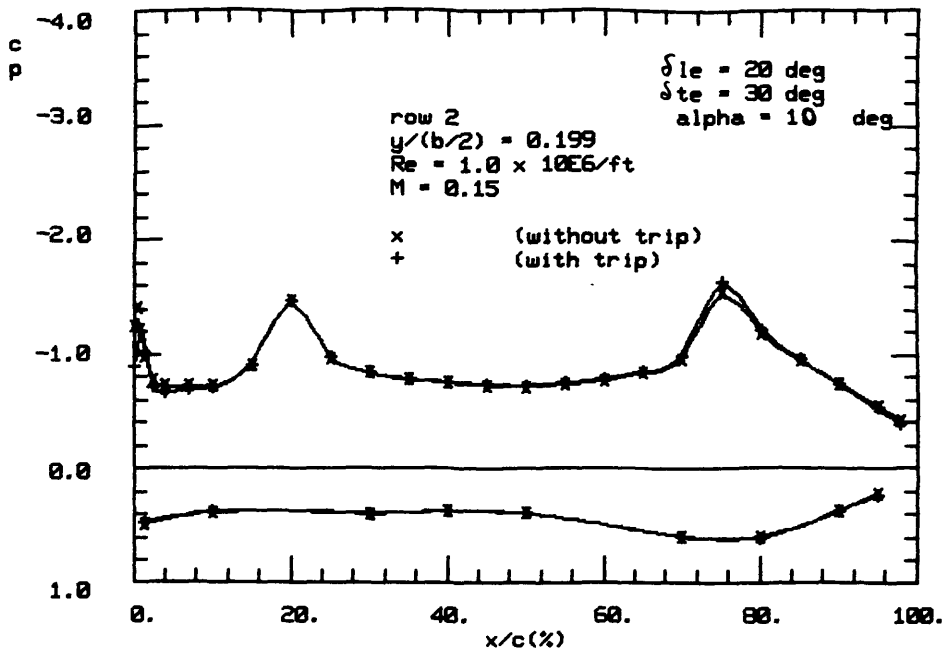

Figure 2.25: Re and trip effects on C_p, δ_{le}=20, δ_{te}=30, $\bar{y}$=0.199, Re=1.0 million/ft

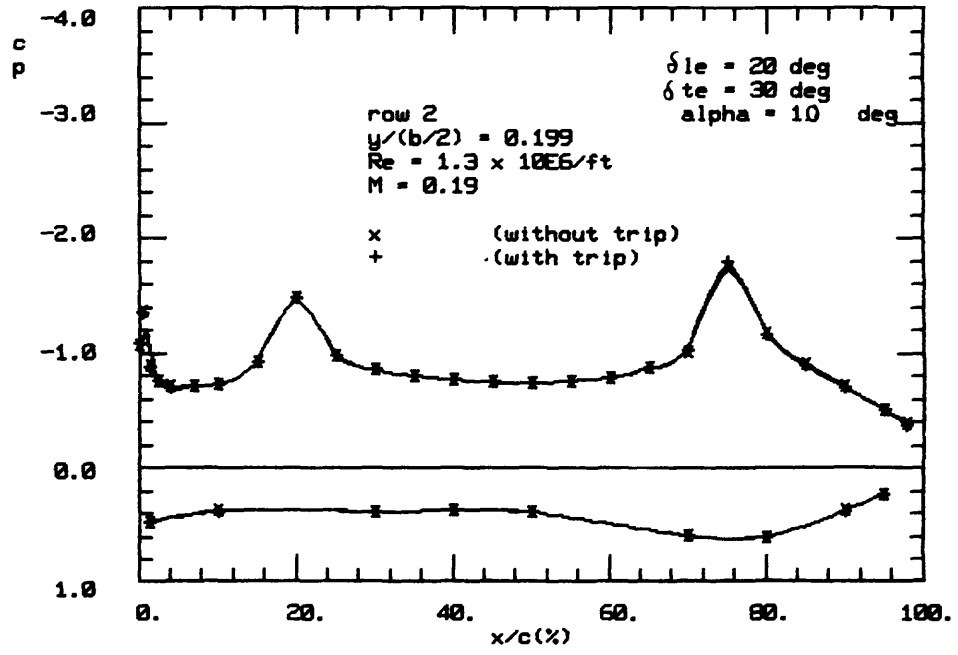

Figure 2.26: Re and trip effects on C_p, δ_{le}=20, δ_{te}=30, $\bar{y}$=0.199, Re=1.3 million/ft

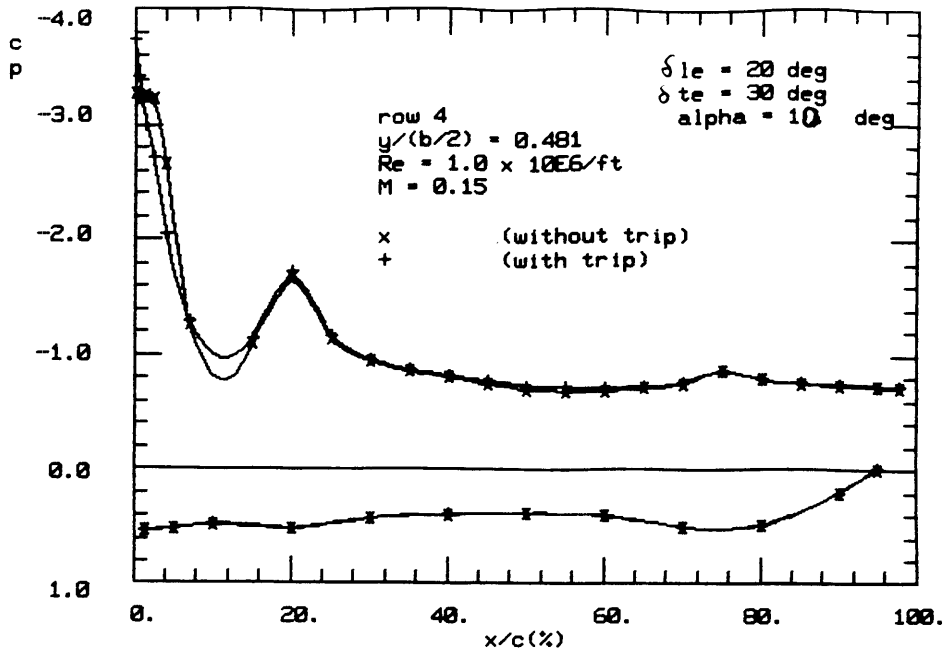

Figure 2.27: Re and trip effects on C_p, δ_{le}=20, δ_{te}=30, $\bar{y}$=0.481, Re=1.0 million/ft

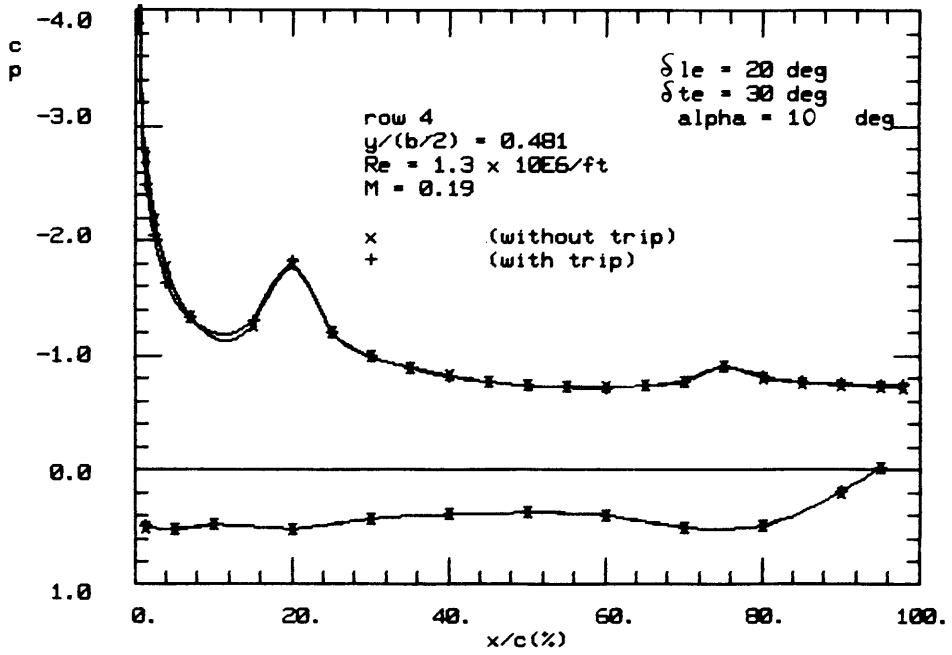

Figure 2.28: Re and trip effects on C_p, δ_{le}=20, δ_{te}=30, $\bar{y}$=0.481, Re=1.3 million/ft

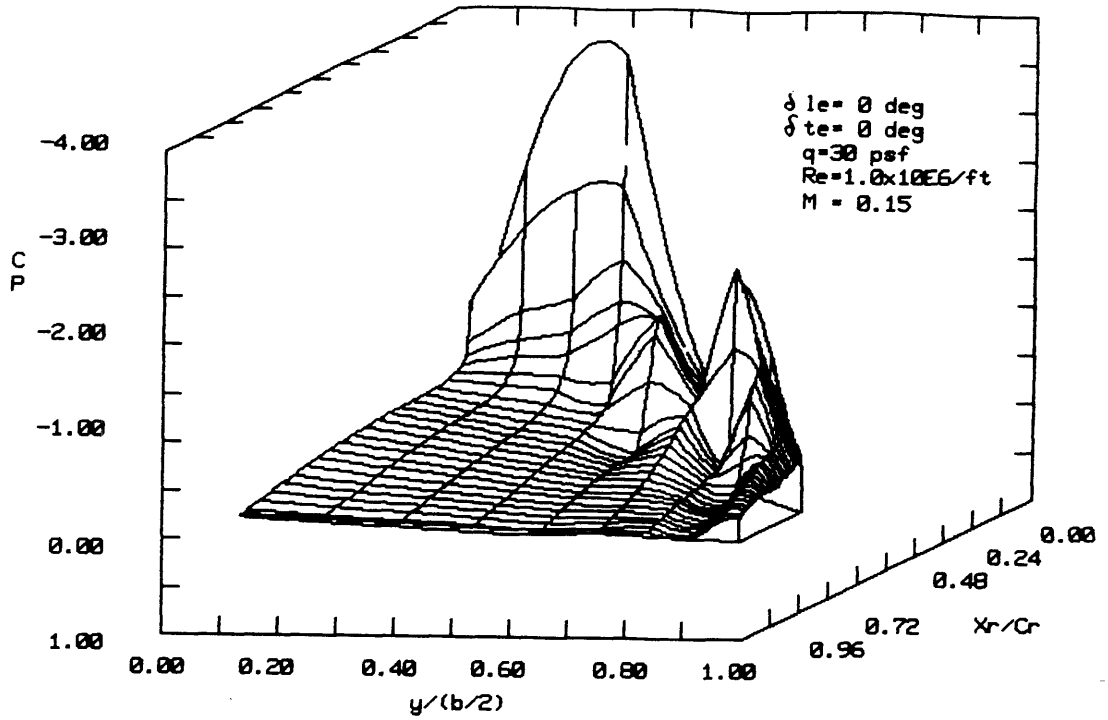

Figure 2.29: Carpet C_p plots, $\delta_{le} = 0$, $\delta_{te} = 0$, $\alpha = 6$ deg

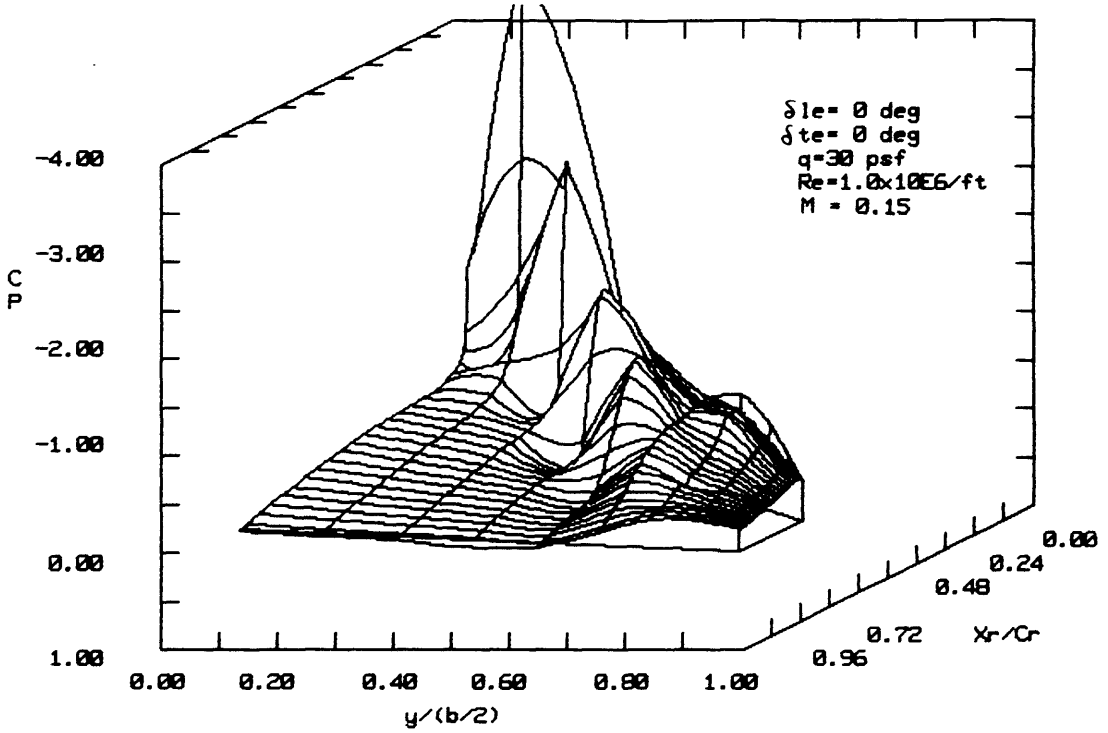

Figure 2.30: Carpet C_p plots, $\delta_{le} = 0$, $\delta_{te} = 0$, $\alpha = 8$ deg

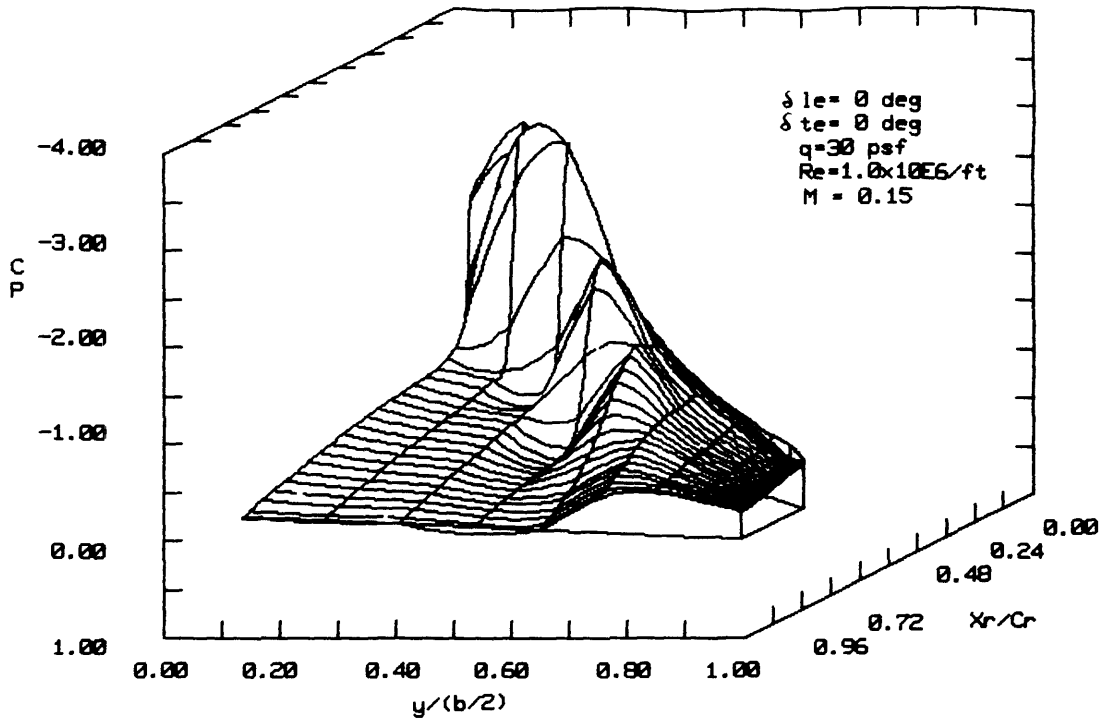

Figure 2.31: Carpet C_p plots, $\delta_{le} = 0$, $\delta_{te} = 0$, $\alpha = 10$ deg

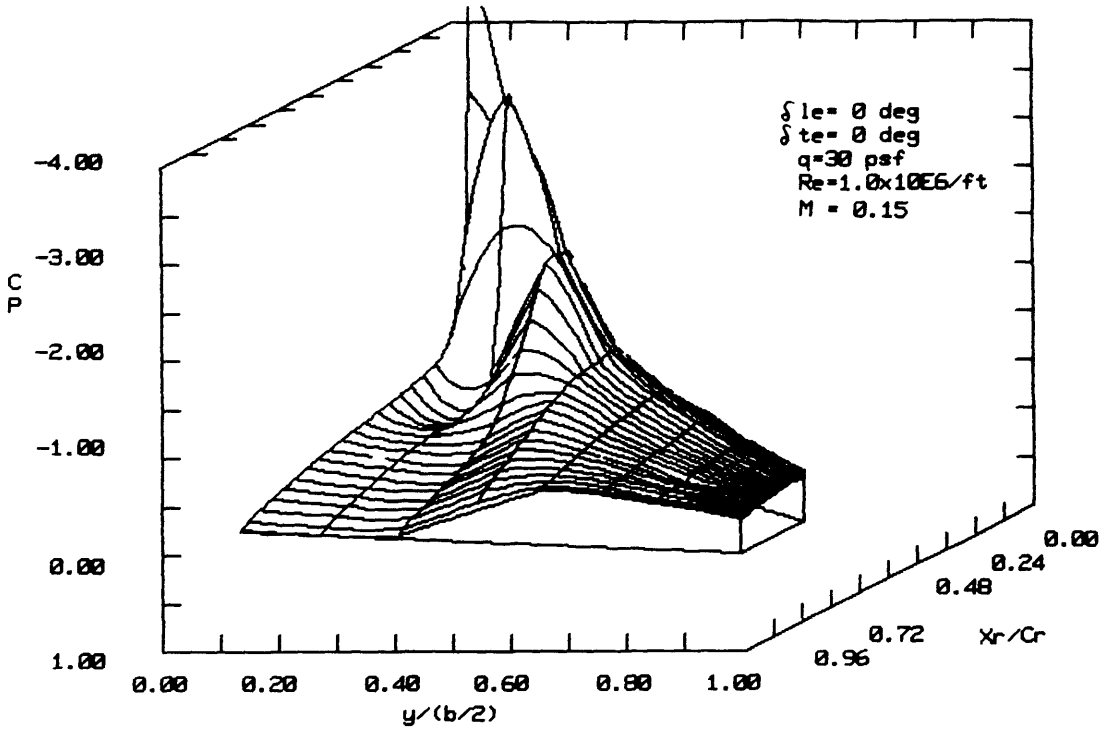

Figure 2.32: Carpet C_p plots, $\delta_{le} = 0$, $\delta_{te} = 0$, $\alpha = 14$ deg

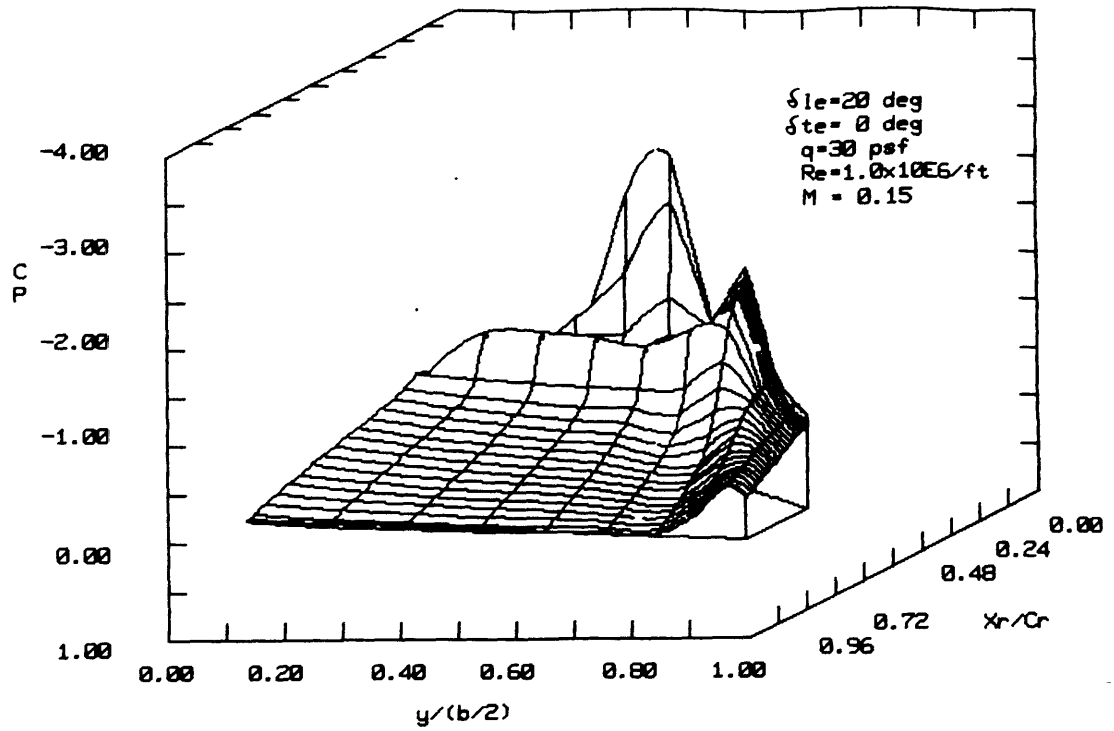

Figure 2.33: Carpet C_p plots, $\delta_{le} = 20$, $\delta_{te} = 0$, $\alpha = 10$ deg

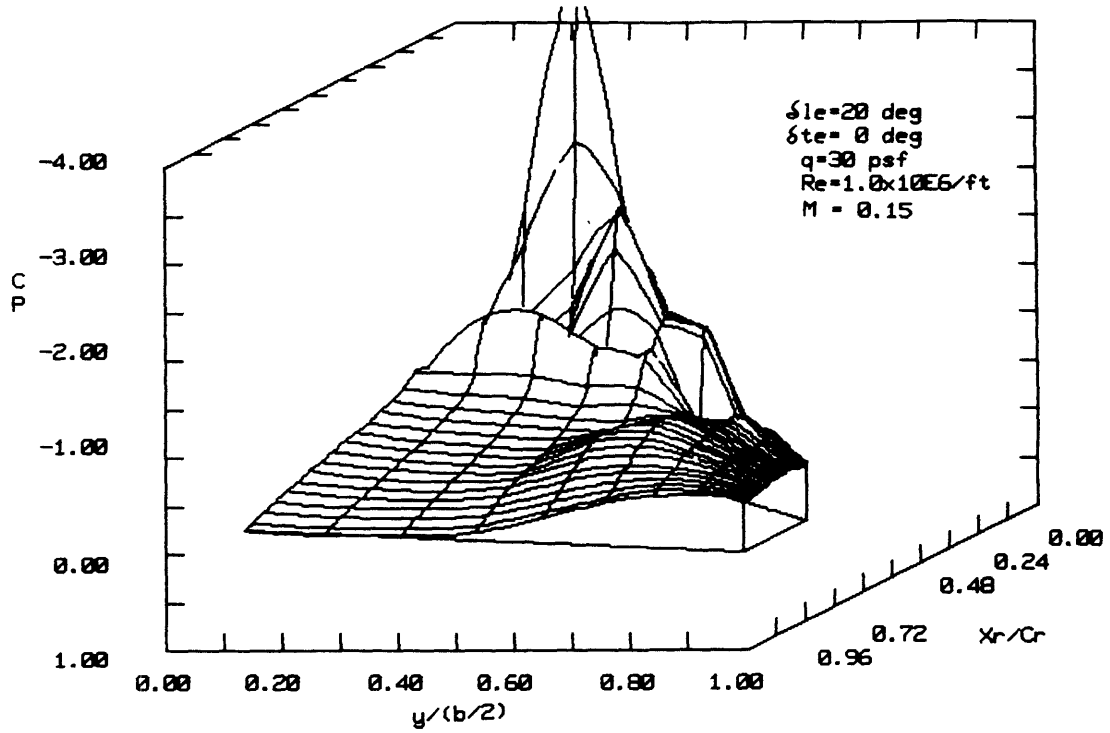

Figure 2.34: Carpet C_p plots, $\delta_{le} = 20$, $\delta_{te} = 0$, $\alpha = 14$ deg

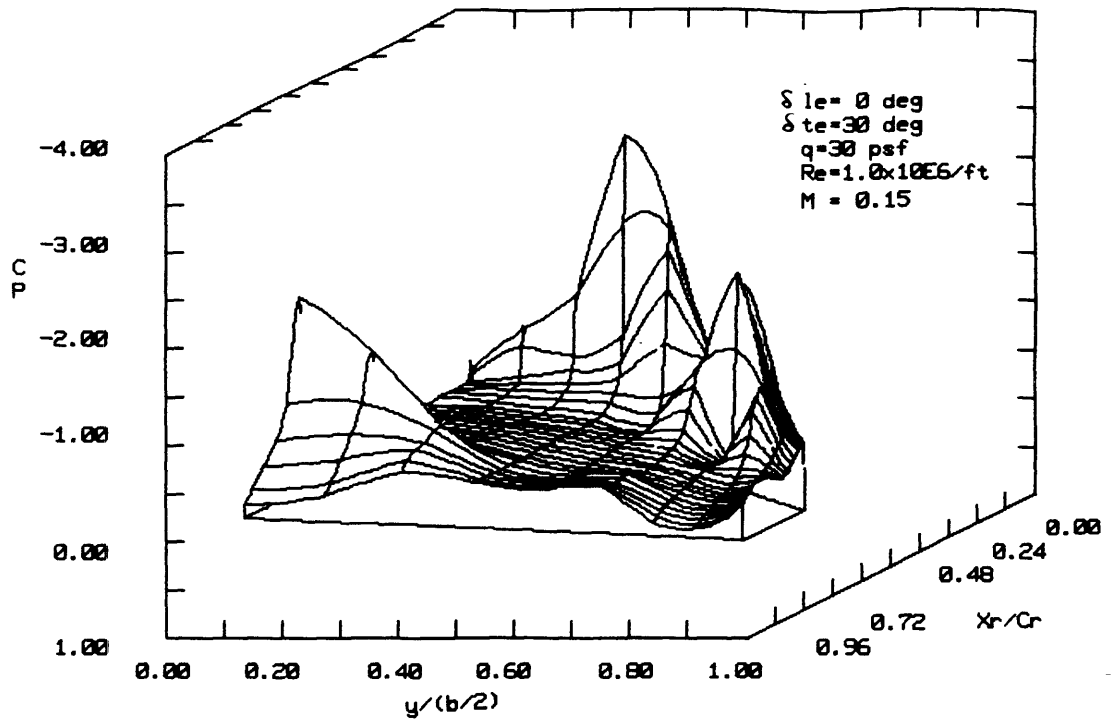

Figure 2.35: Carpet C_p plots, $\delta_{le} = 0$, $\delta_{te} = 30$, $\alpha = 0$ deg

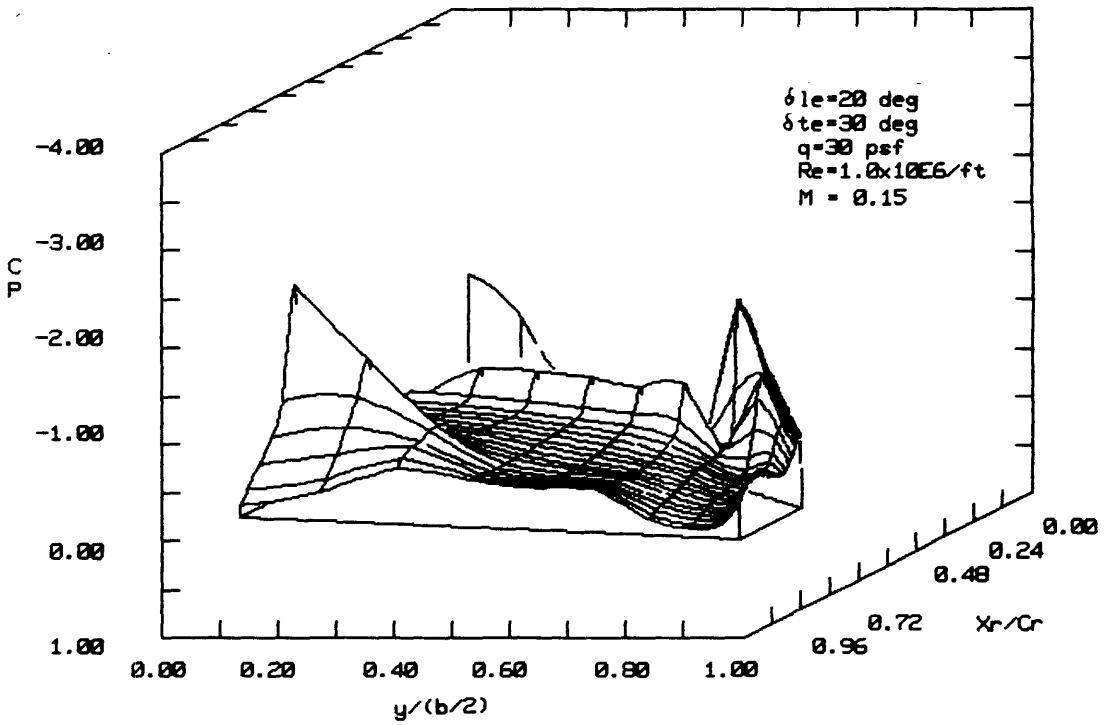

Figure 2.36: Carpet C_p plots, $\delta_{le} = 20$, $\delta_{te} = 30$, $\alpha = 0$ deg

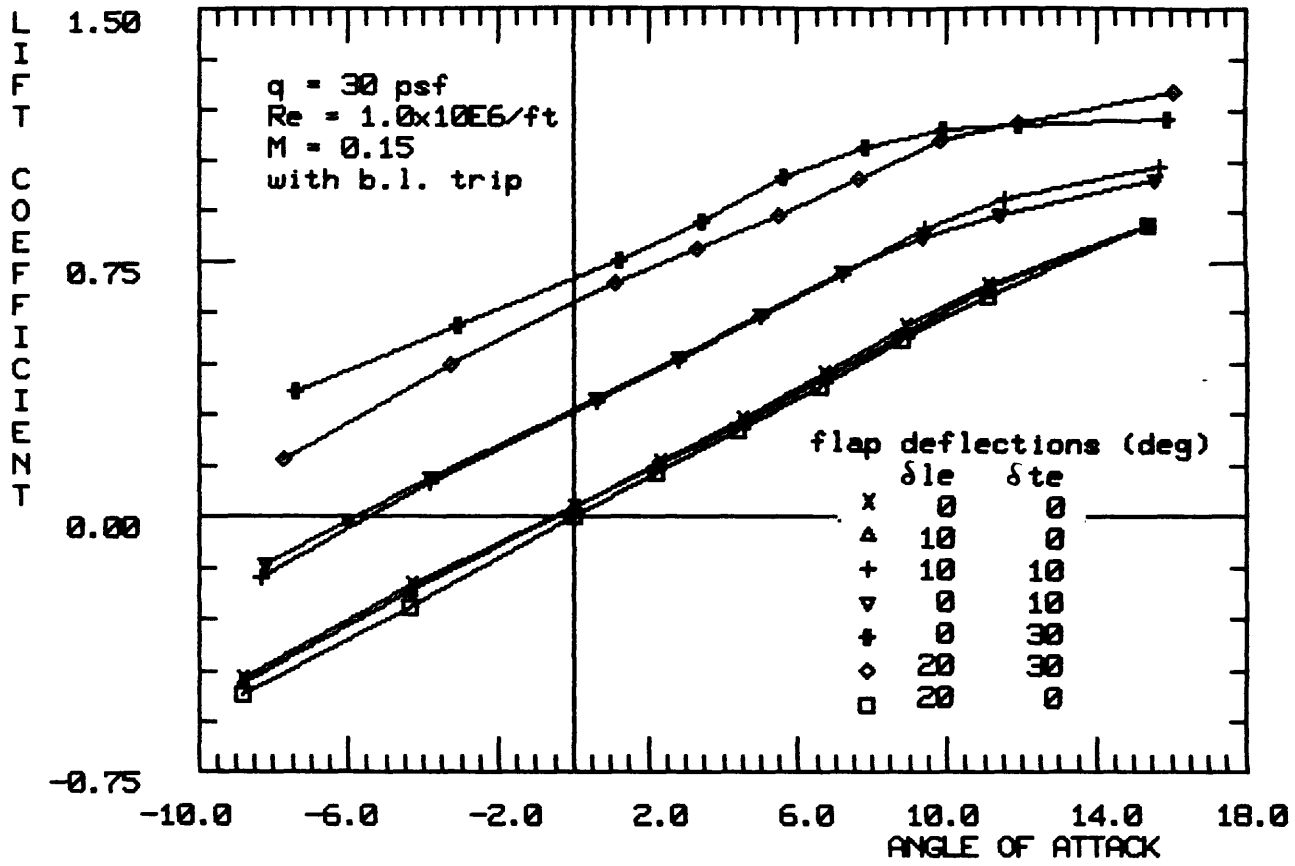

Figure 2.37: Flap effects on C_L versus α

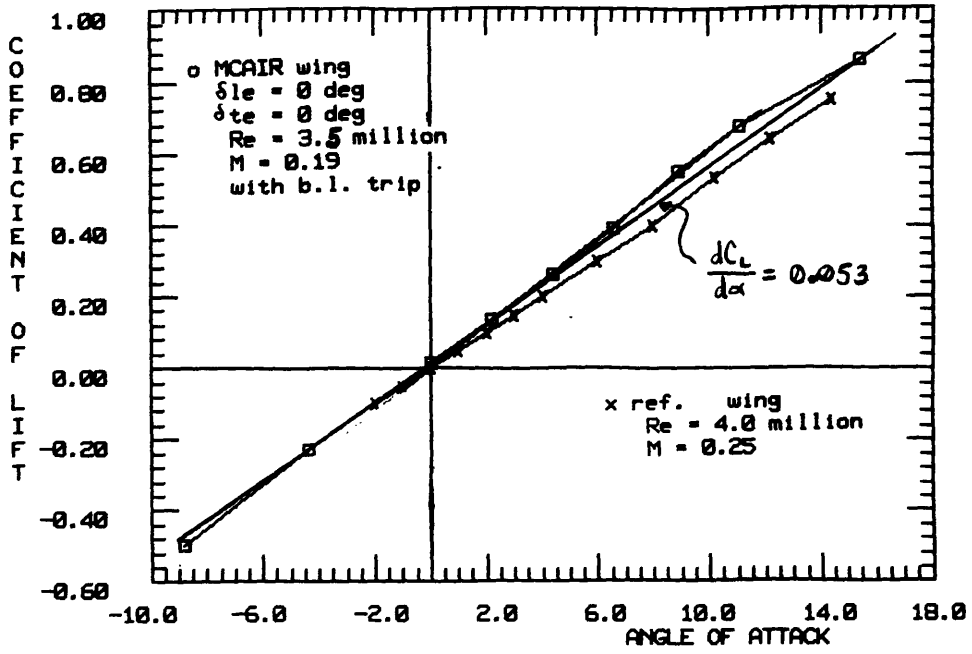

Figure 2.38: Experimental comparisons of C_L vs. $\alpha_{corrected}$

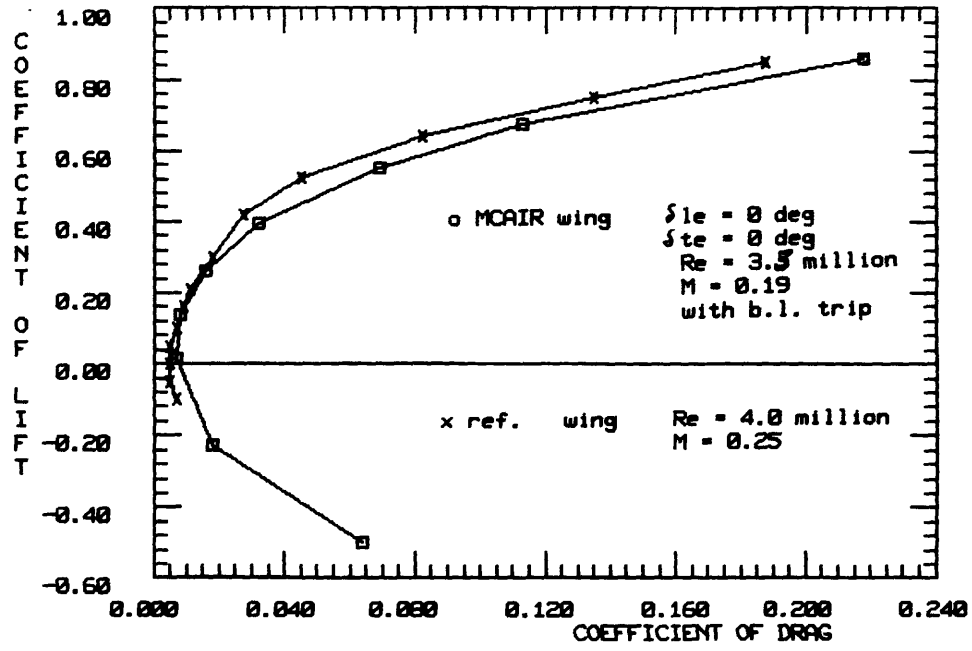

Figure 2.39: Experimental comparisons of C_L vs. $C_{D_{corrected}}$

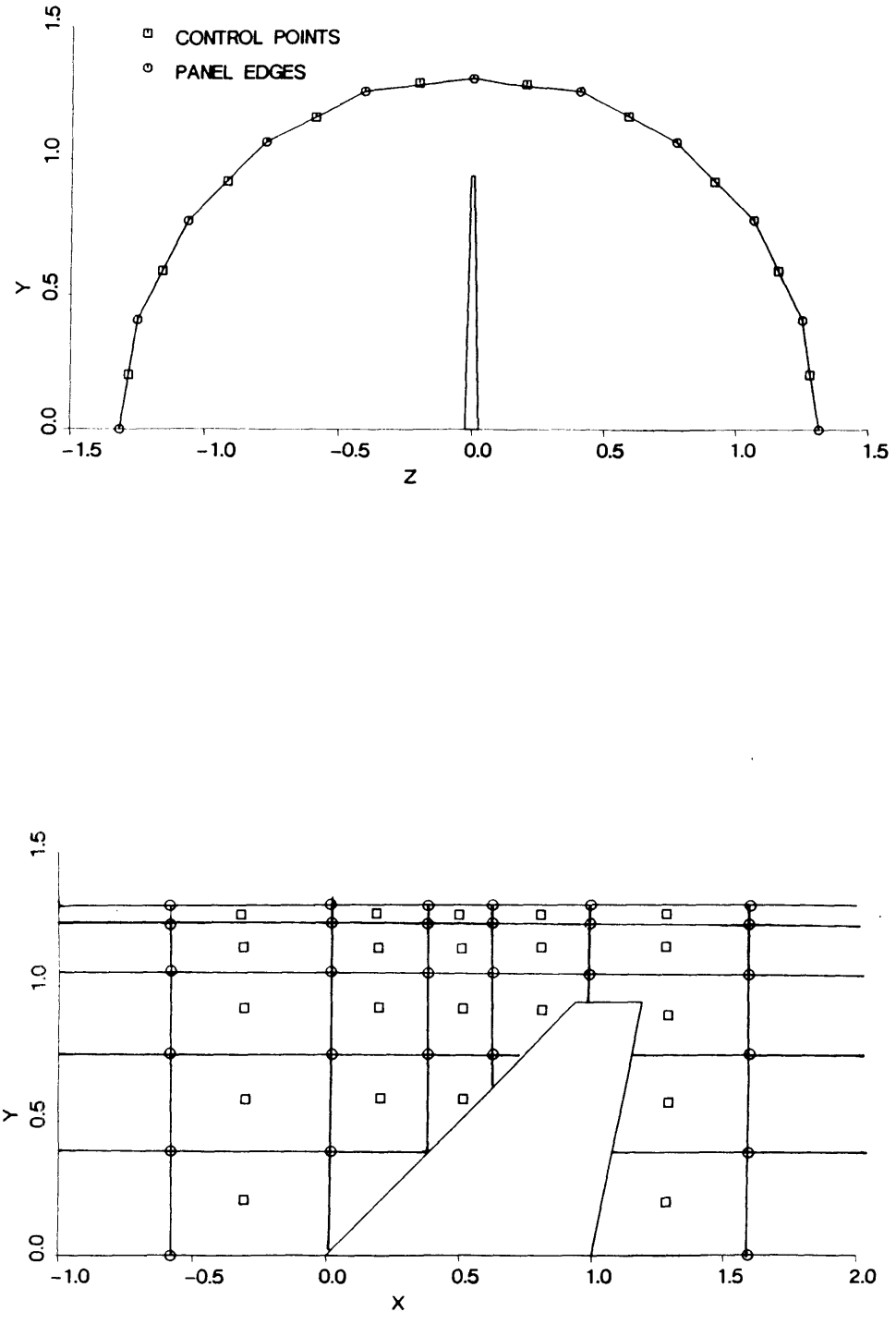

Figure 3.1: Wind tunnel paneling, floor mounted semi-span wing

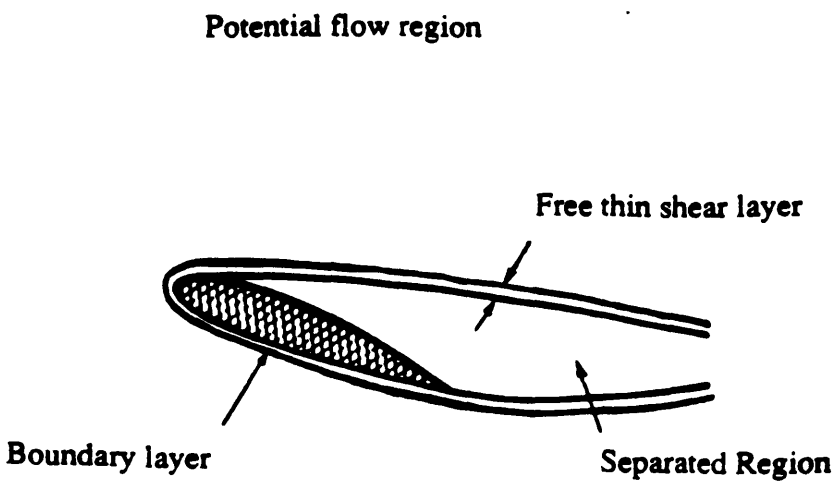

Figure 3.2: Flow regions for analytical wing model

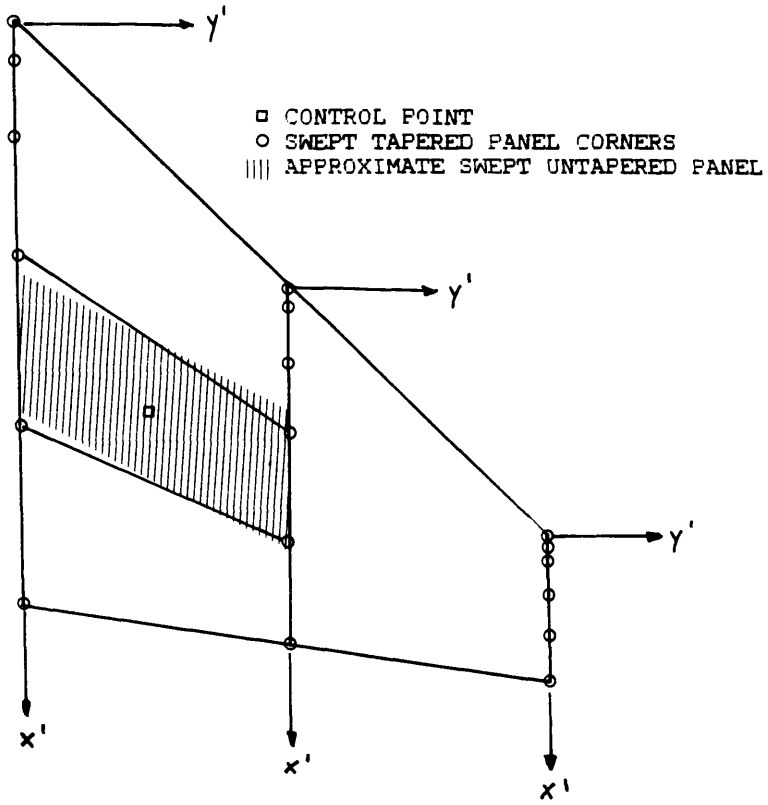

Figure 3.3: Paneling distribution on analytical wing model

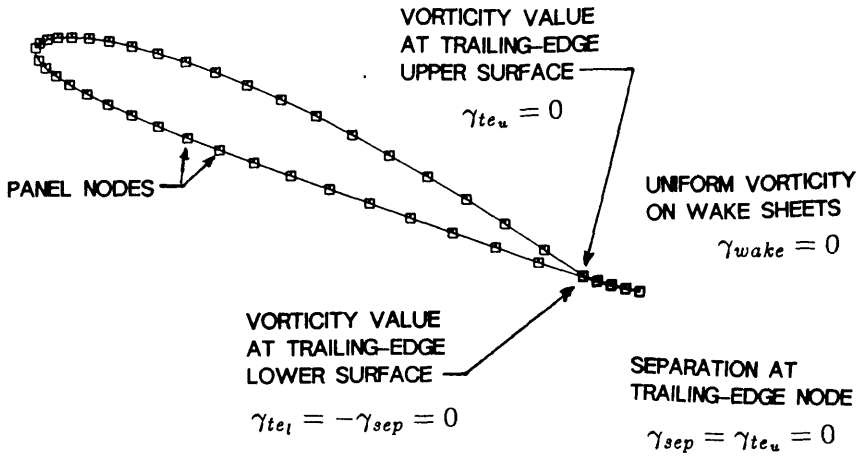

Figure 3.4: Vorticity boundary conditions for attached flow

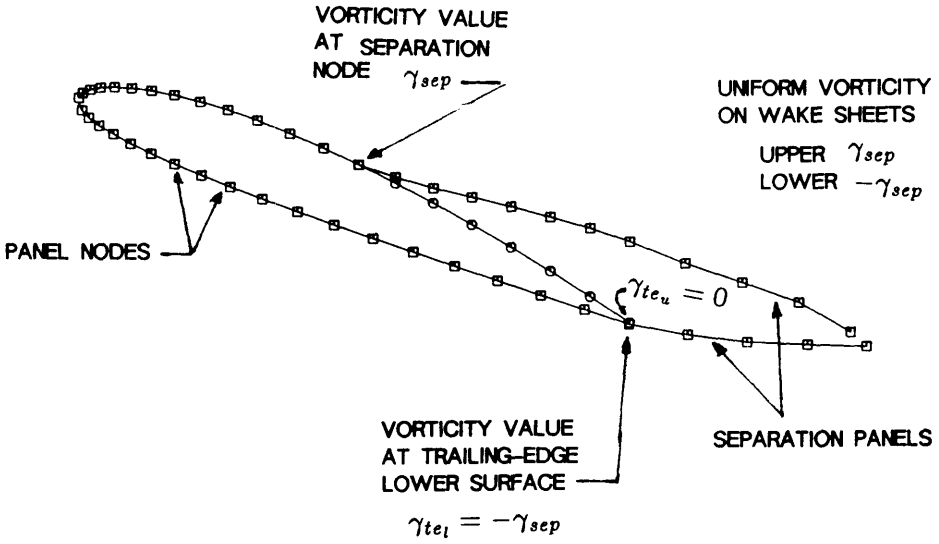

Figure 3.5: Vorticity boundary conditions for separated flow

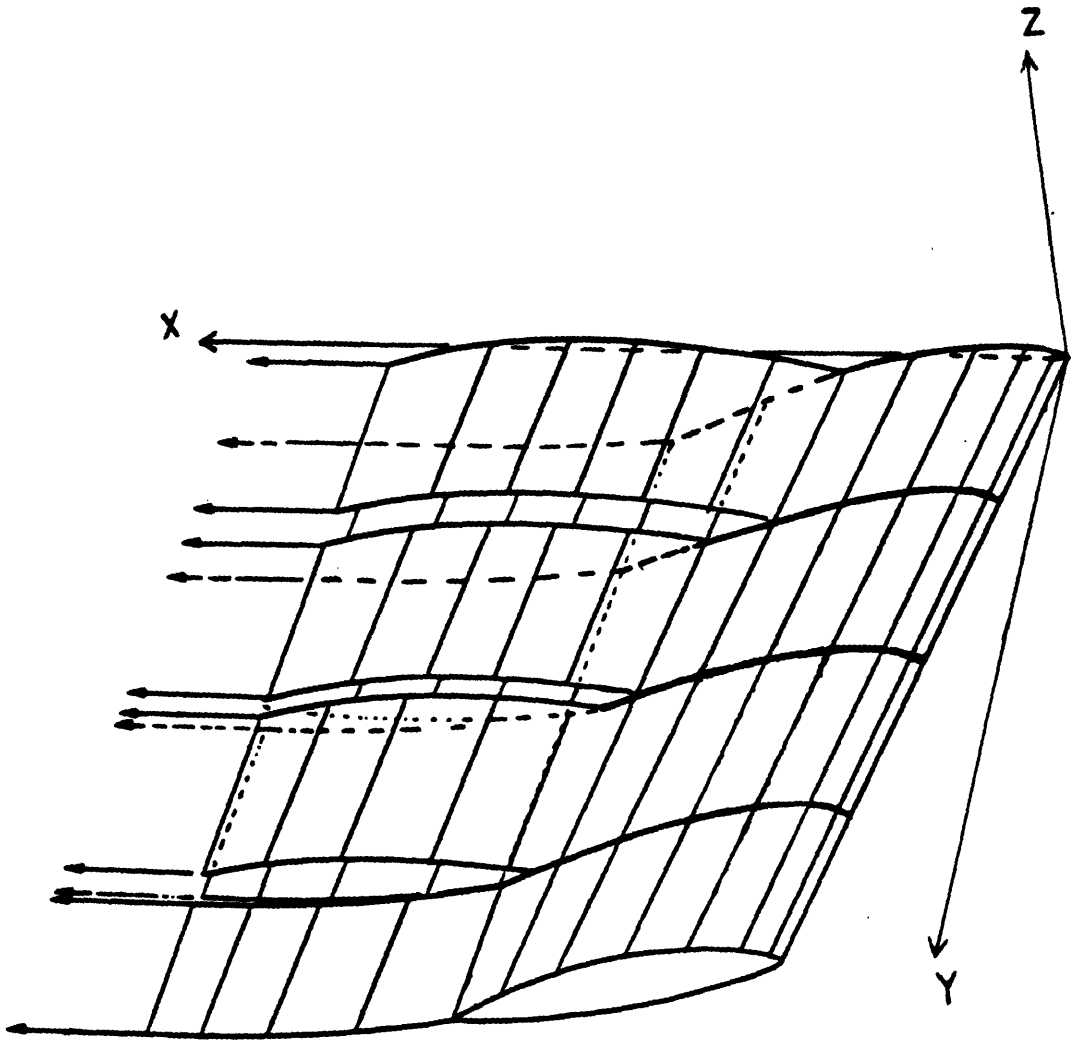

Figure 3.6: Separated flow model for finite wing

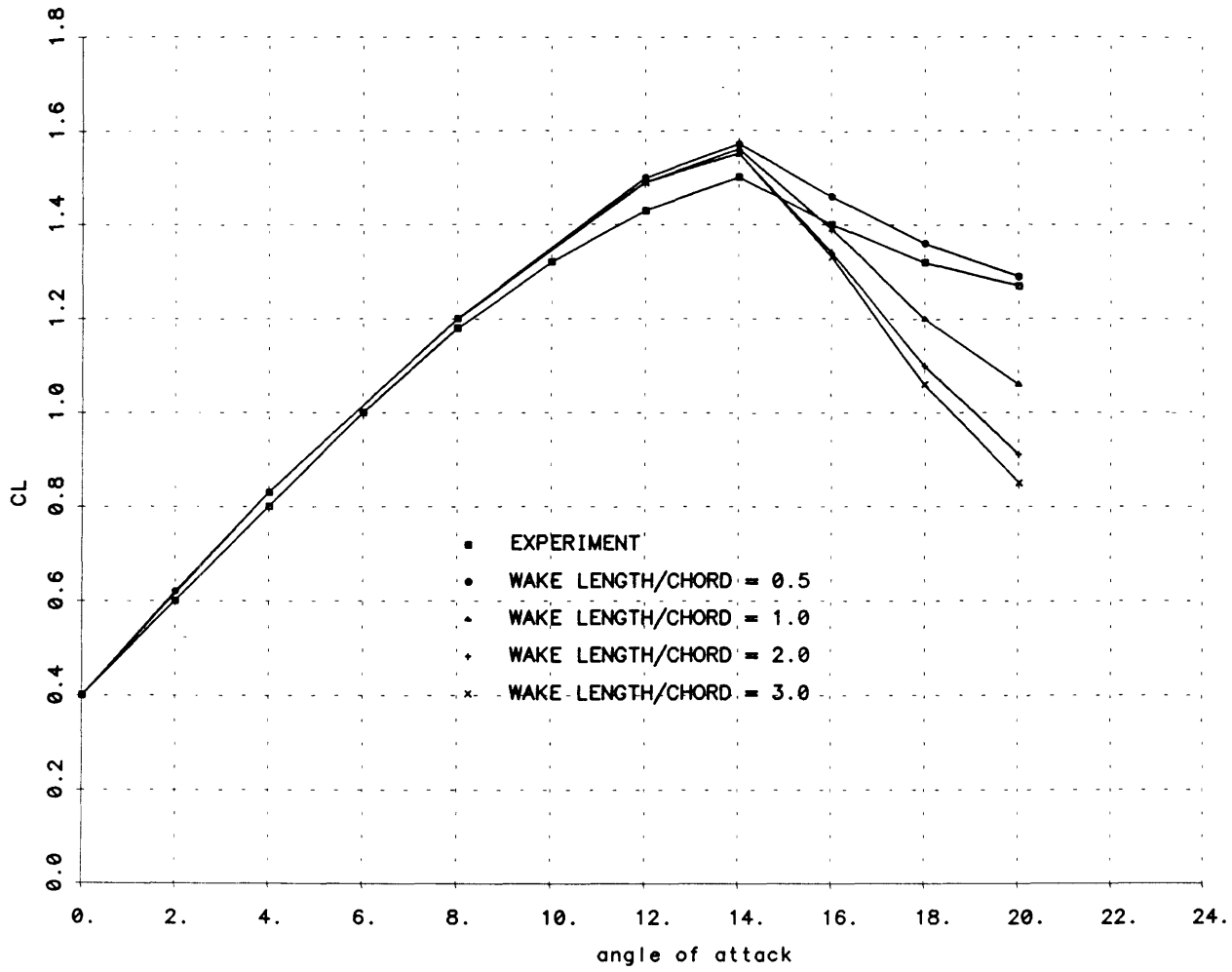

Figure 3.7: Influence of wake length on lift curve (NACA 4412)

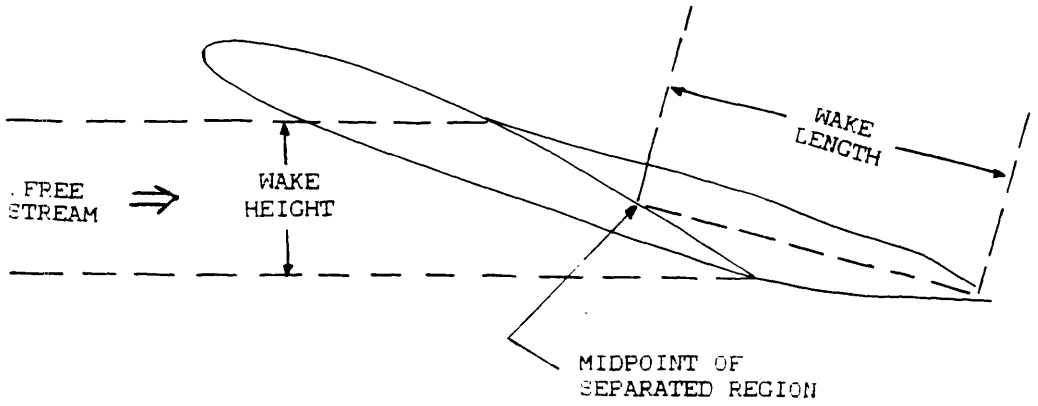

WAKE LENGTH = (WAKE HEIGHT) x (WAKE LENGTH FACTOR)

Figure 3.8: Definition of wake length

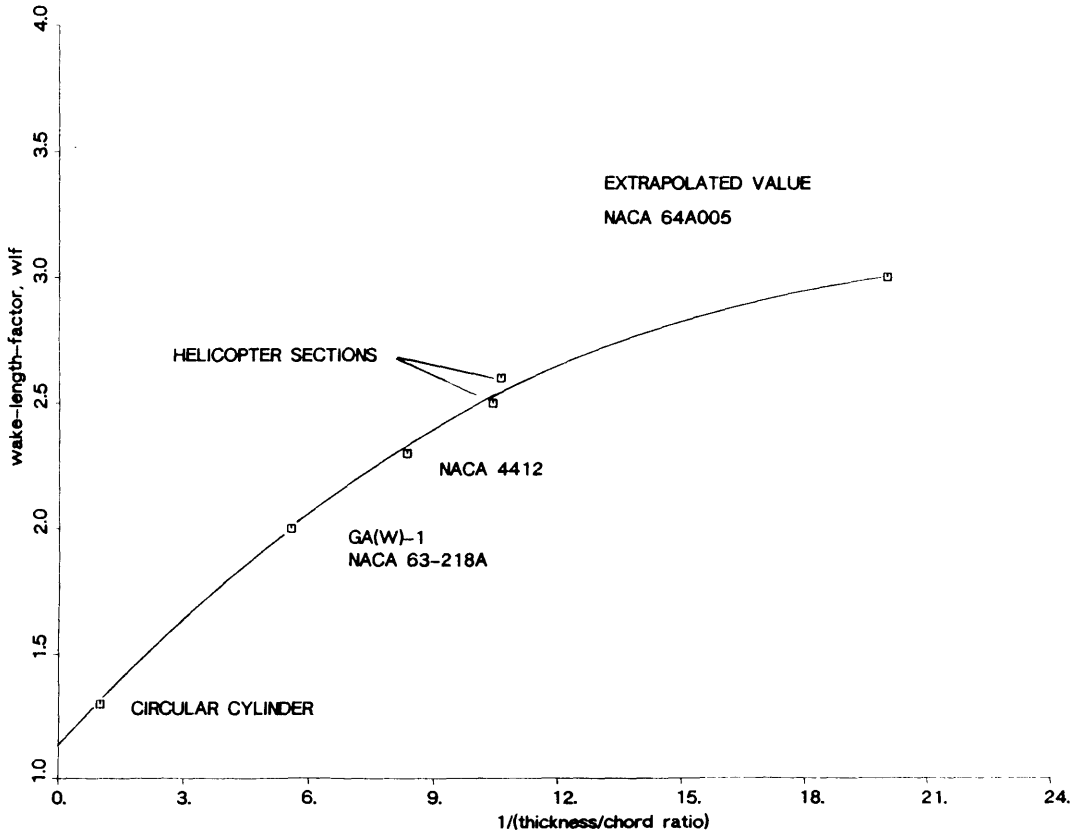

Figure 3.9: Curve for estimating wake length factor

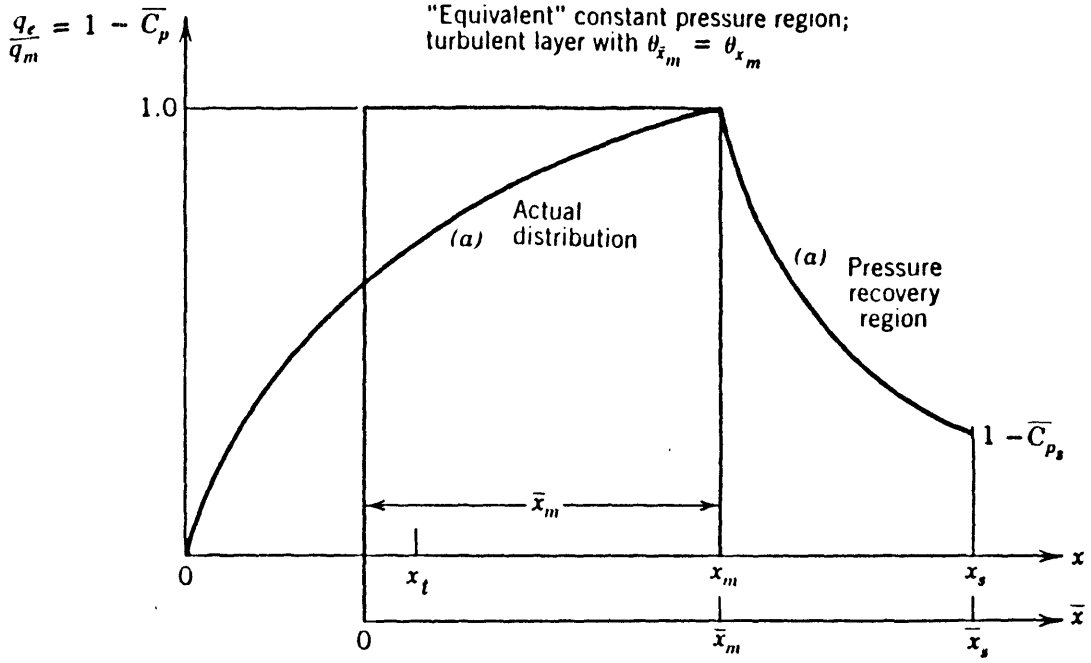

Actual and "equivalent" distributions of $\overline{C_p}$ versus x and $\bar{x}$.

Reference [13]

Figure 3.10: Stratford's "equivalent" distributions

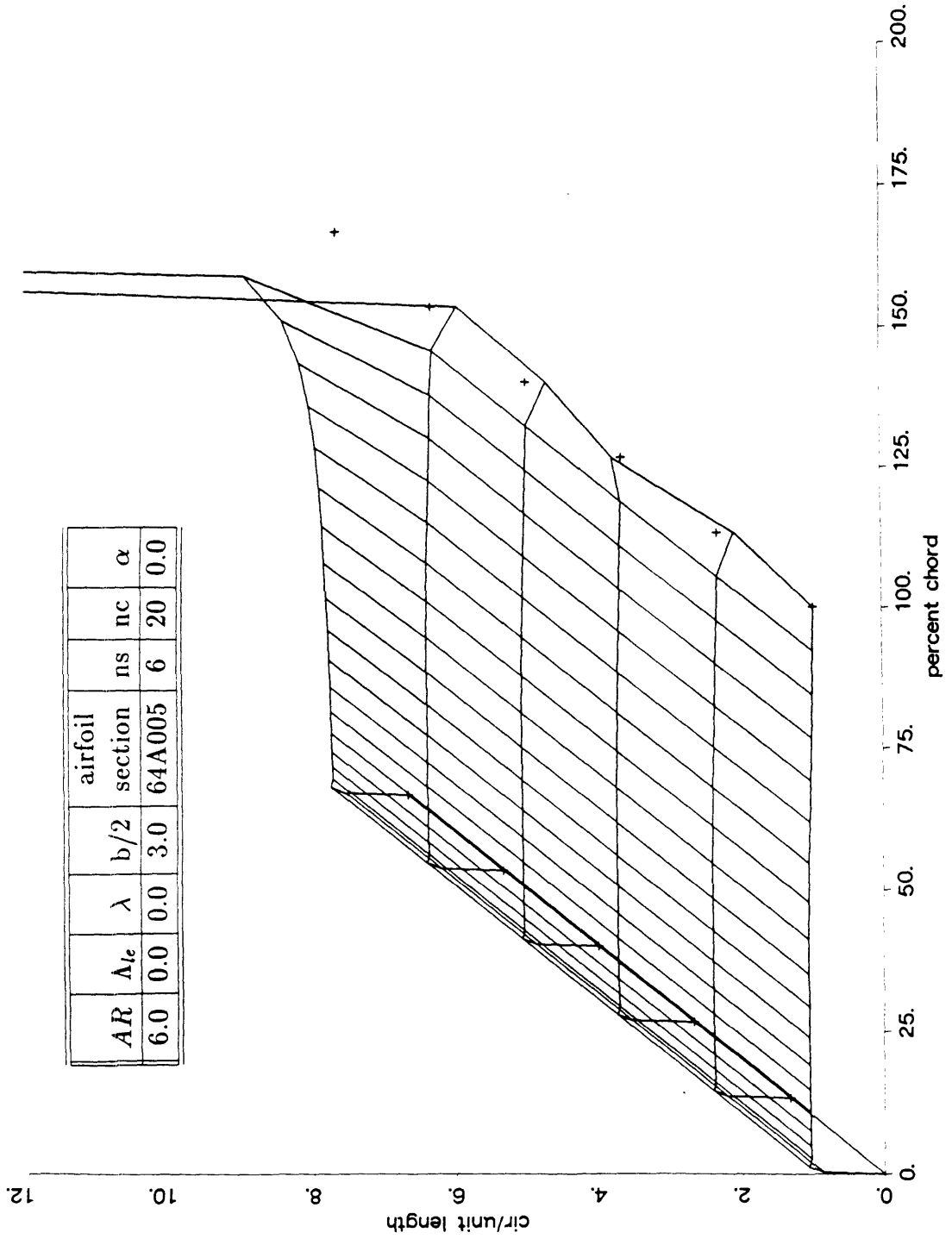

Figure 4.1: Wing surface vorticity, $\gamma_{te_l} = -\gamma_{te_u}$, $\frac{n_s}{b} = 1$, t/c = 0.05

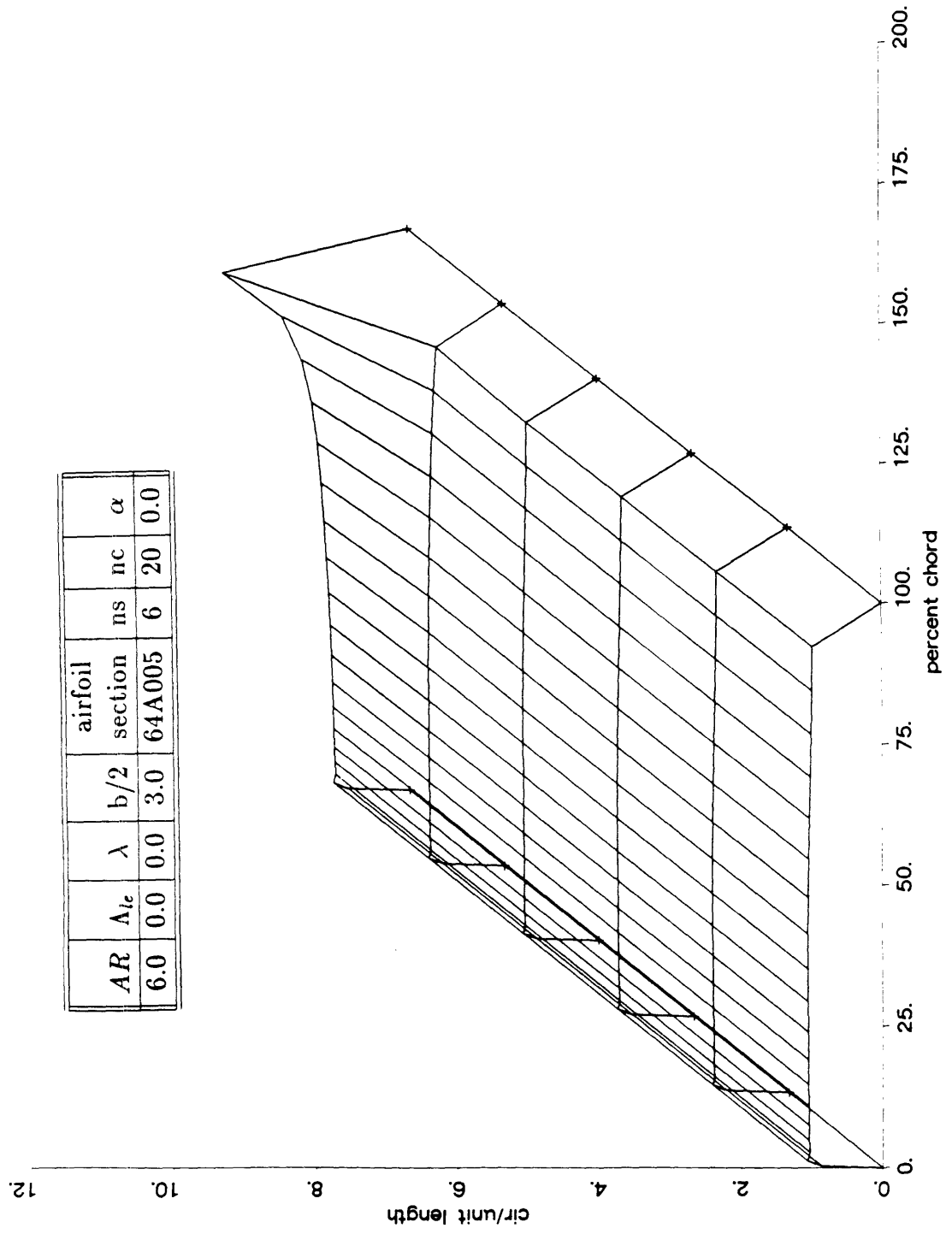

Figure 4.2: Wing surface vorticity, $\gamma_{te_l} = \gamma_{te_u} = 0$, $\frac{ns}{b} = 1$, t/c = 0.05

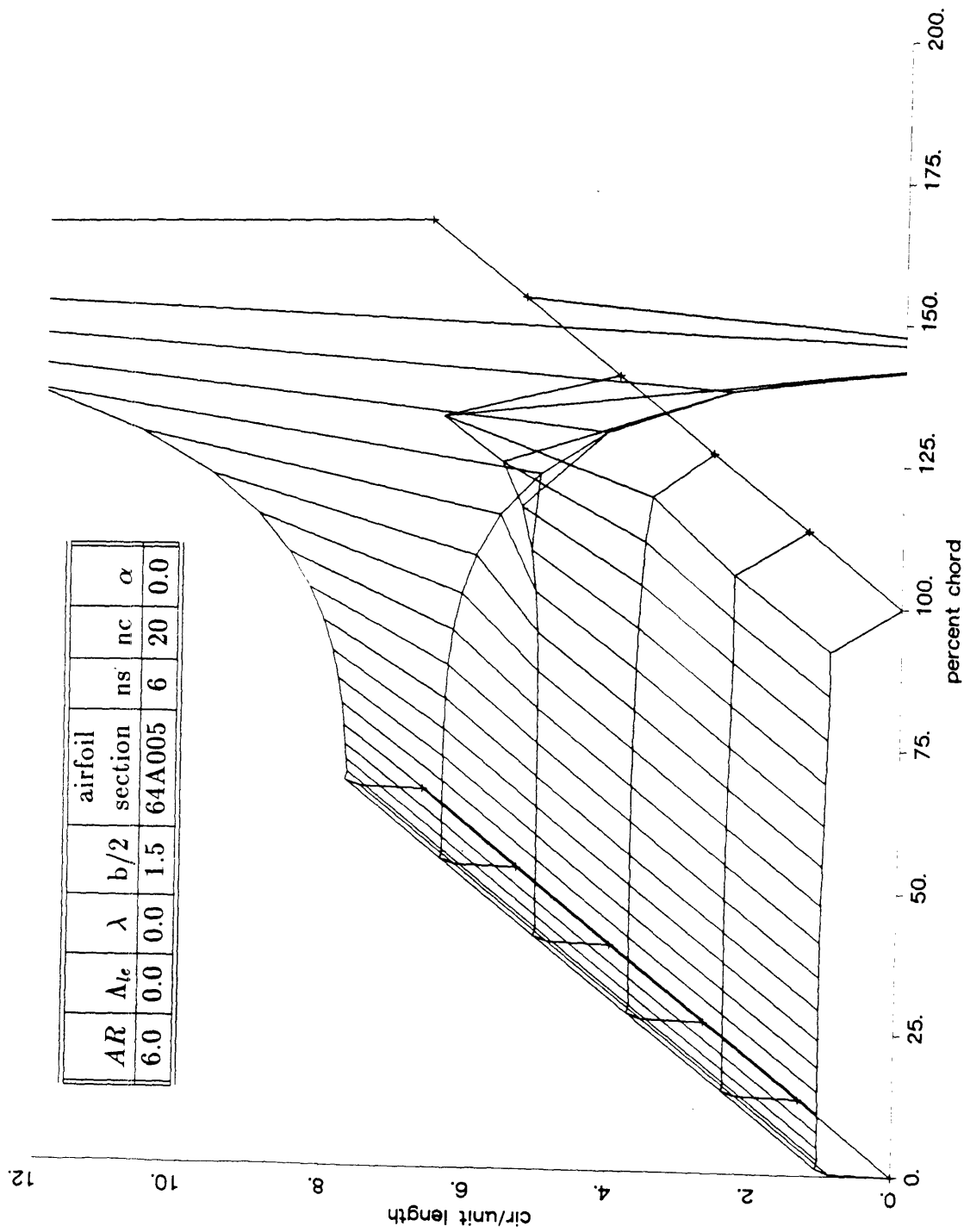

Figure 4.3: Wing surface vorticity, $\gamma_{te_l} = \gamma_{te_u} = 0$, $\frac{ns}{b} = 2$, t/c = 0.05

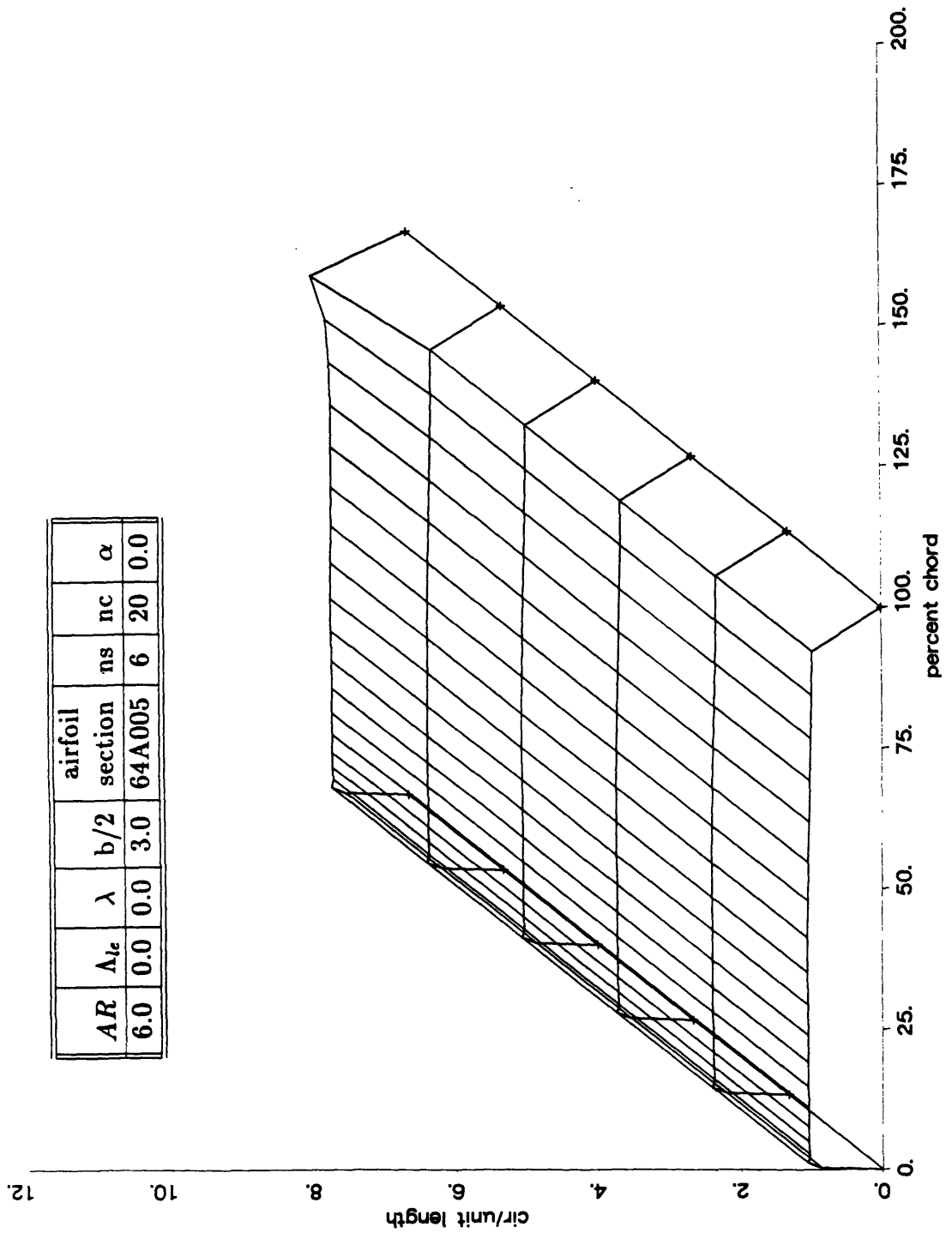

Figure 4.4: Wing surface vorticity, $\gamma_{te_l} = \gamma_{te_u} = 0$, $\frac{ns}{b} = 1$, t/c = 0.05, $\Gamma_U = \Gamma_L = 0$

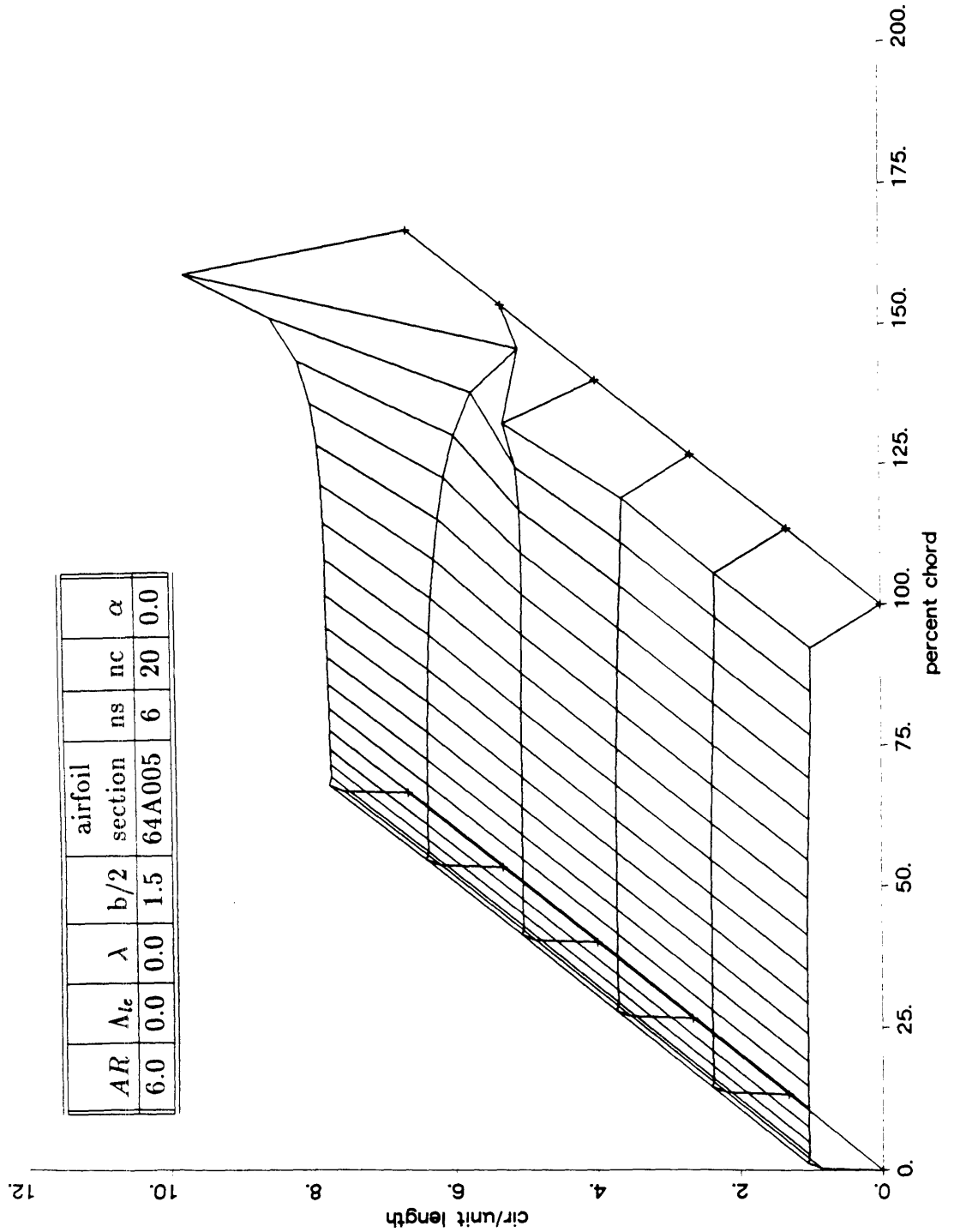

AR	Λ_{lc}	λ	b/2	airfoil section	ns	nc	α
6.0	0.0	0.0	1.5	64A005	6	20	0.0

Figure 4.5: Wing surface vorticity, $\gamma_{te_l} = \gamma_{te_u} = 0$, $\frac{ns}{b} = 2$, t/c = 0.05, $\Gamma_U = \Gamma_L = 0$

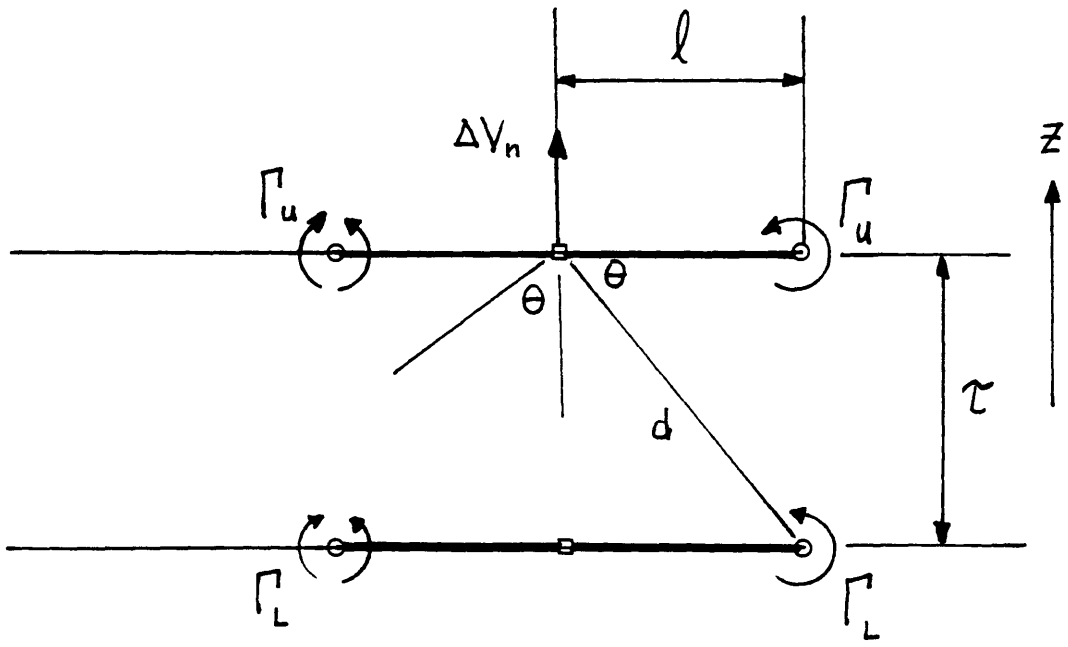

$$d^2 = l^2 + \tau^2$$

$$\cos\theta = \frac{l}{d}$$

$$\Delta V_{n_U} = -\frac{\Gamma_U}{4\pi l}$$

$$\Delta V_{n_L} = -\frac{\Gamma_L}{4\pi d}\cos\theta = -\frac{\Gamma_L}{4\pi l}\left(\frac{1}{1+(\frac{\tau}{l})^2}\right)$$

Figure 4.6: "tip effect" geometry and derivation

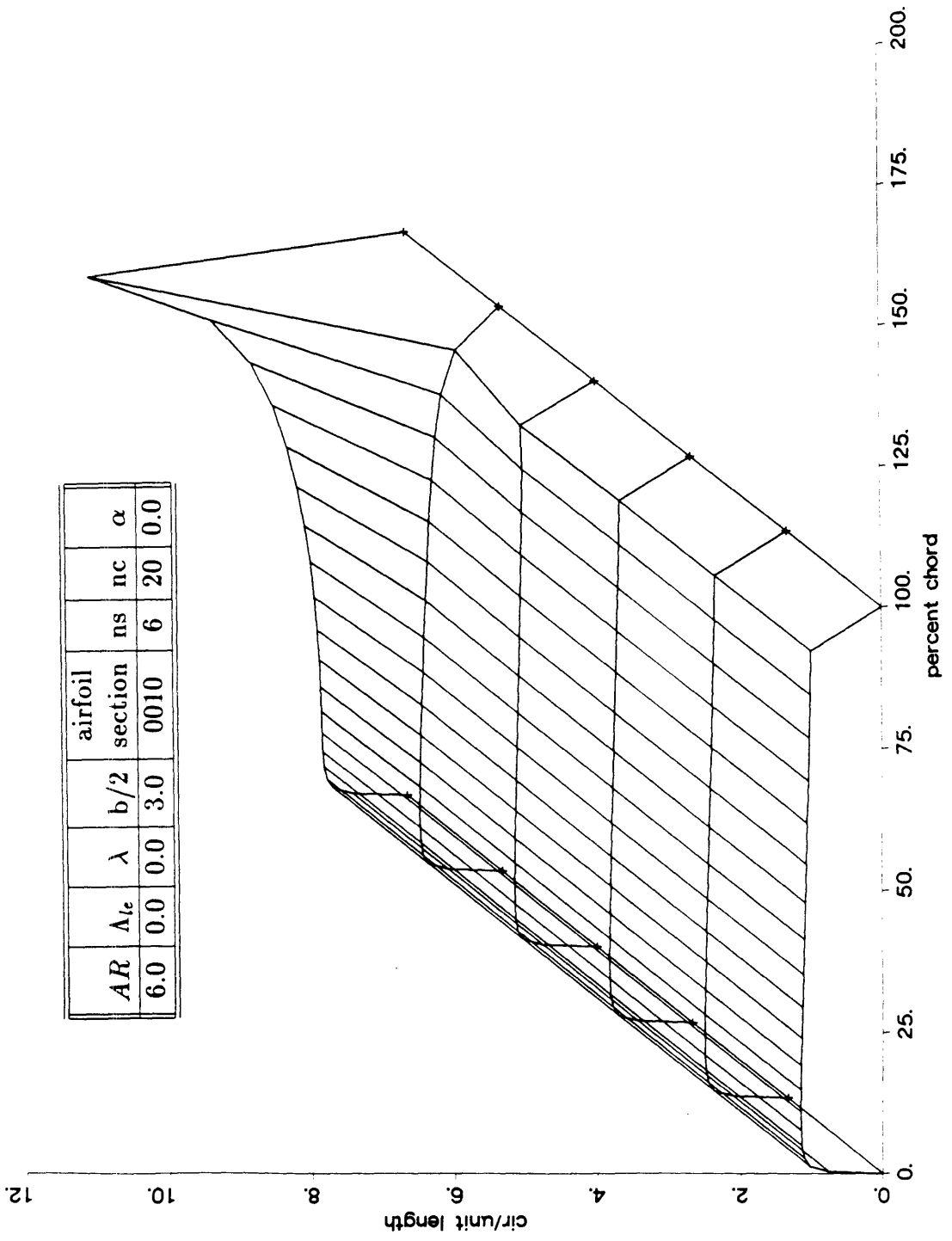

Figure 4.7: Wing surface vorticity, $\gamma_{te_l} = \gamma_{te_u} = 0$, $\frac{ns}{b} = 1$, t/c = 0.10

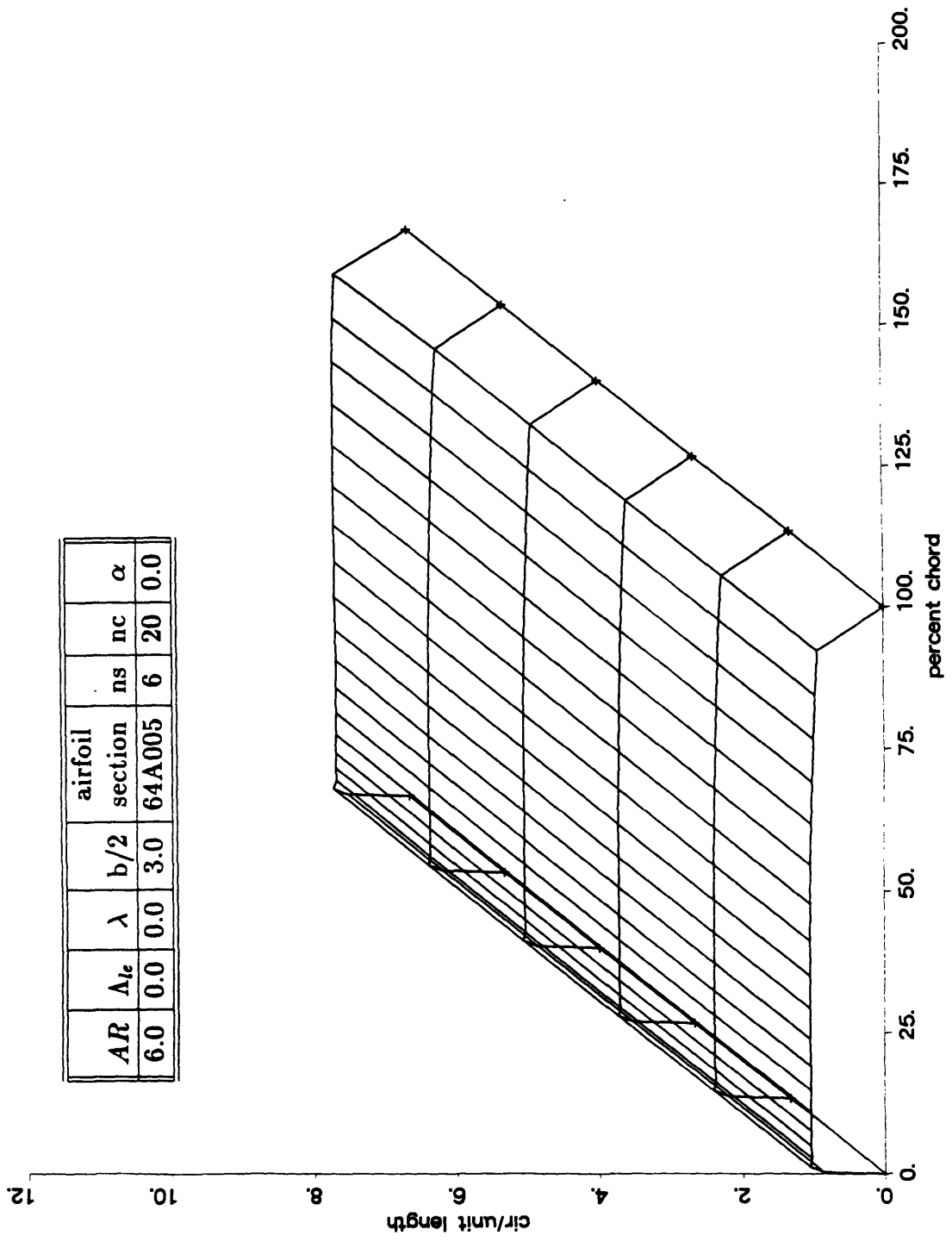

Figure 4.8: Wing surface vorticity, $\gamma_{te_l} = \gamma_{te_u} = 0$, $\frac{ns}{b} = 1$, t/c = 0.05, sheet source

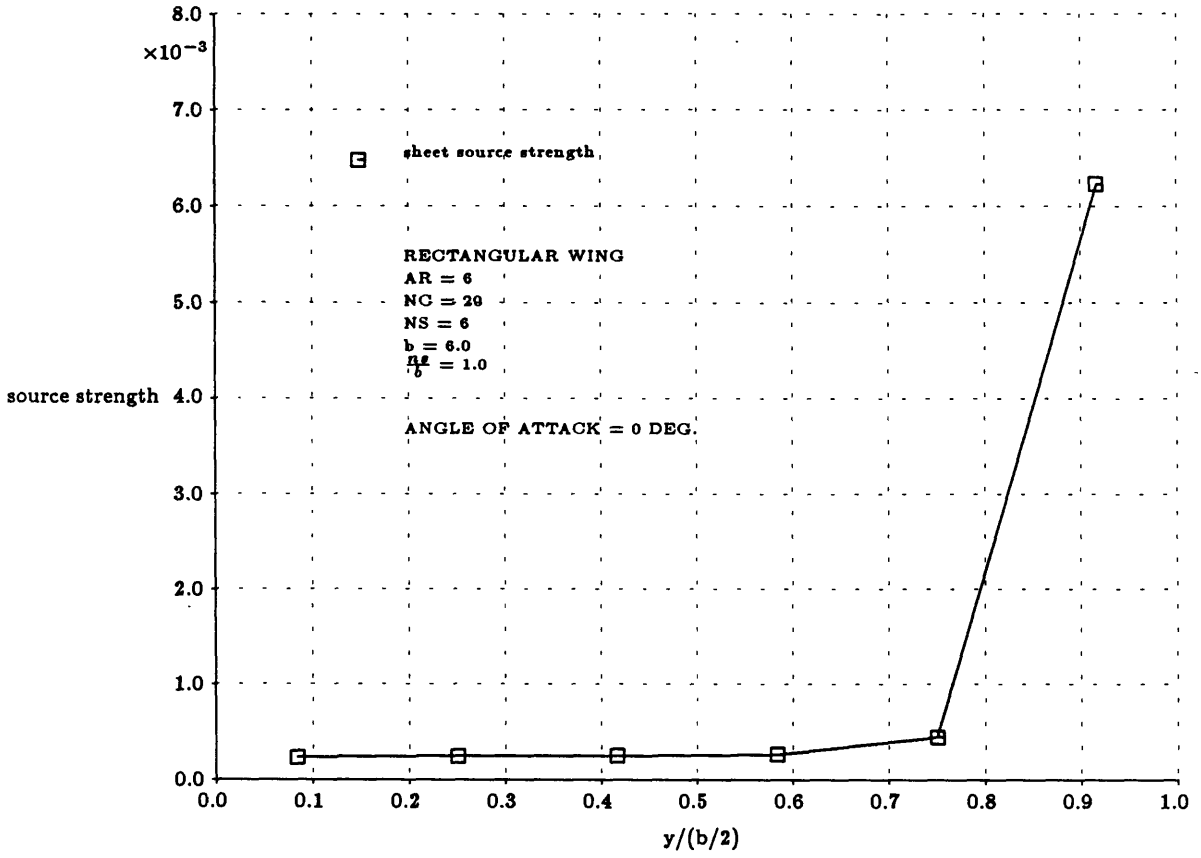

Figure 4.9: Variation of source strength vs. semi-span location

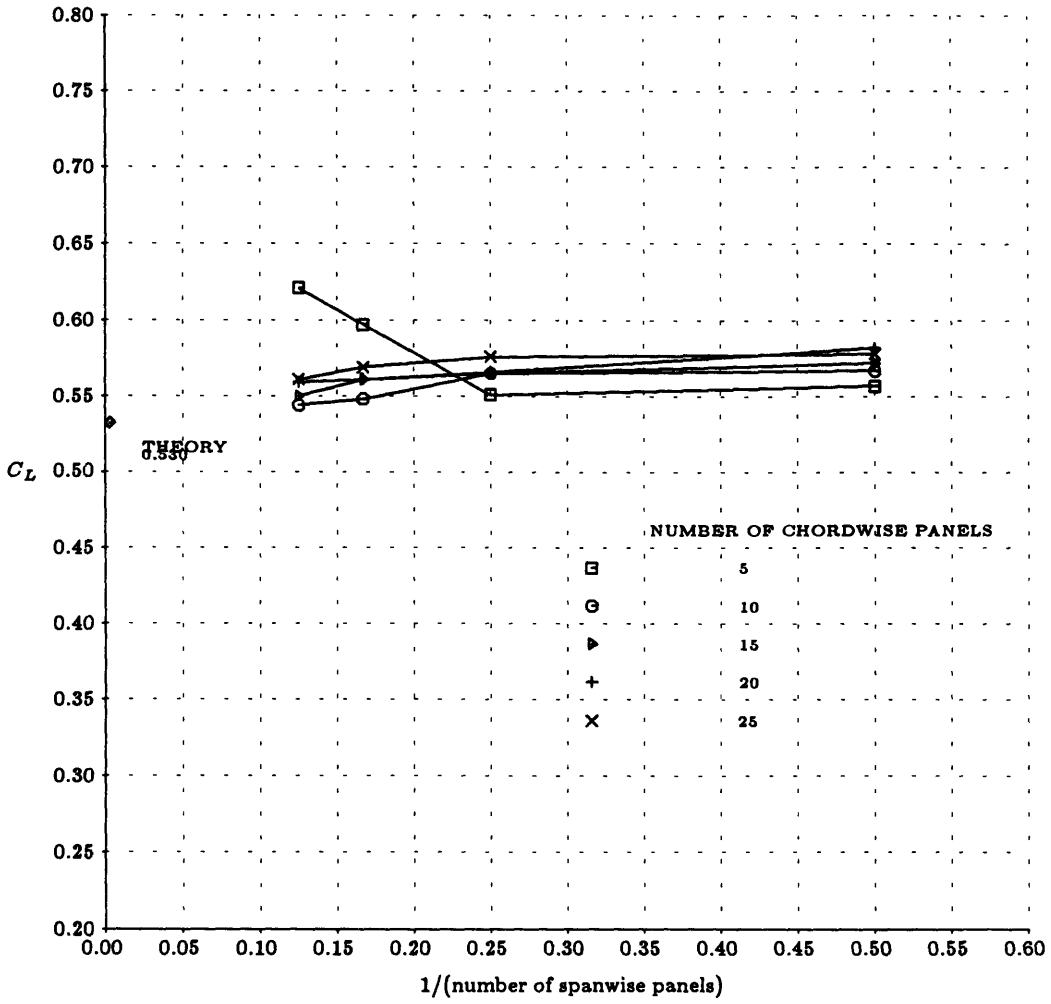

Figure 4.10: C_L vs. 1/ns for $\alpha = 10$ deg, nc = 5,10,15,20,25

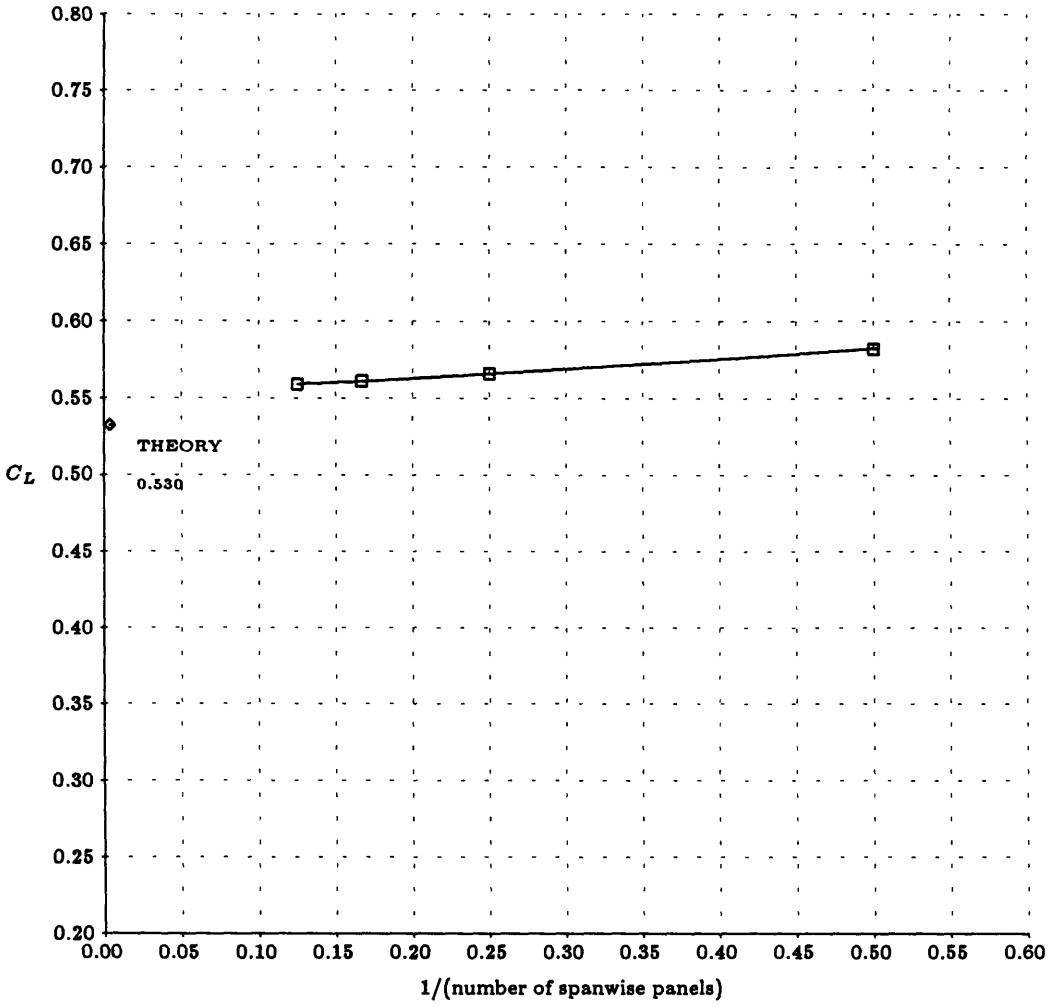

Figure 4.11: C_L vs. 1/ns for $\alpha = 10$ deg, nc = 20

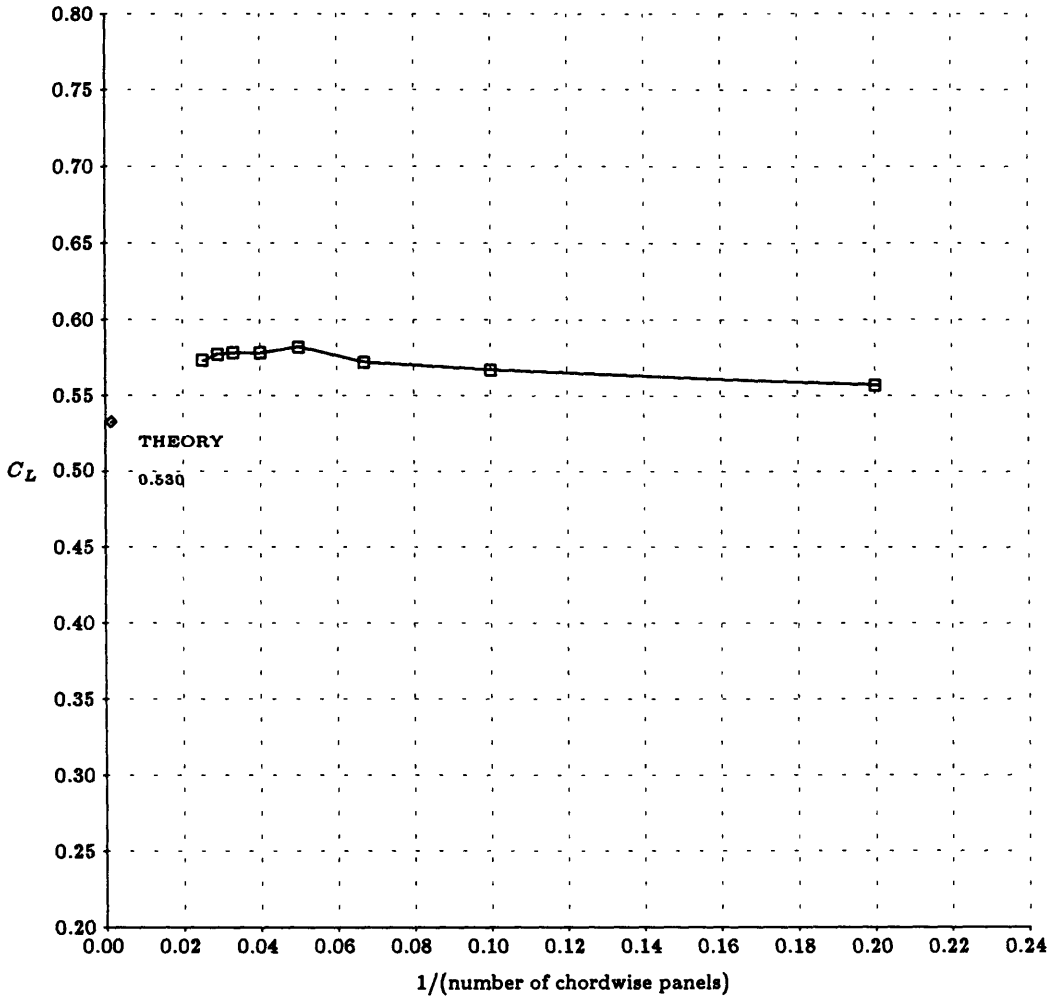

Figure 4.12: C_L vs. 1/nc for $\alpha = 10$ deg, ns = 2

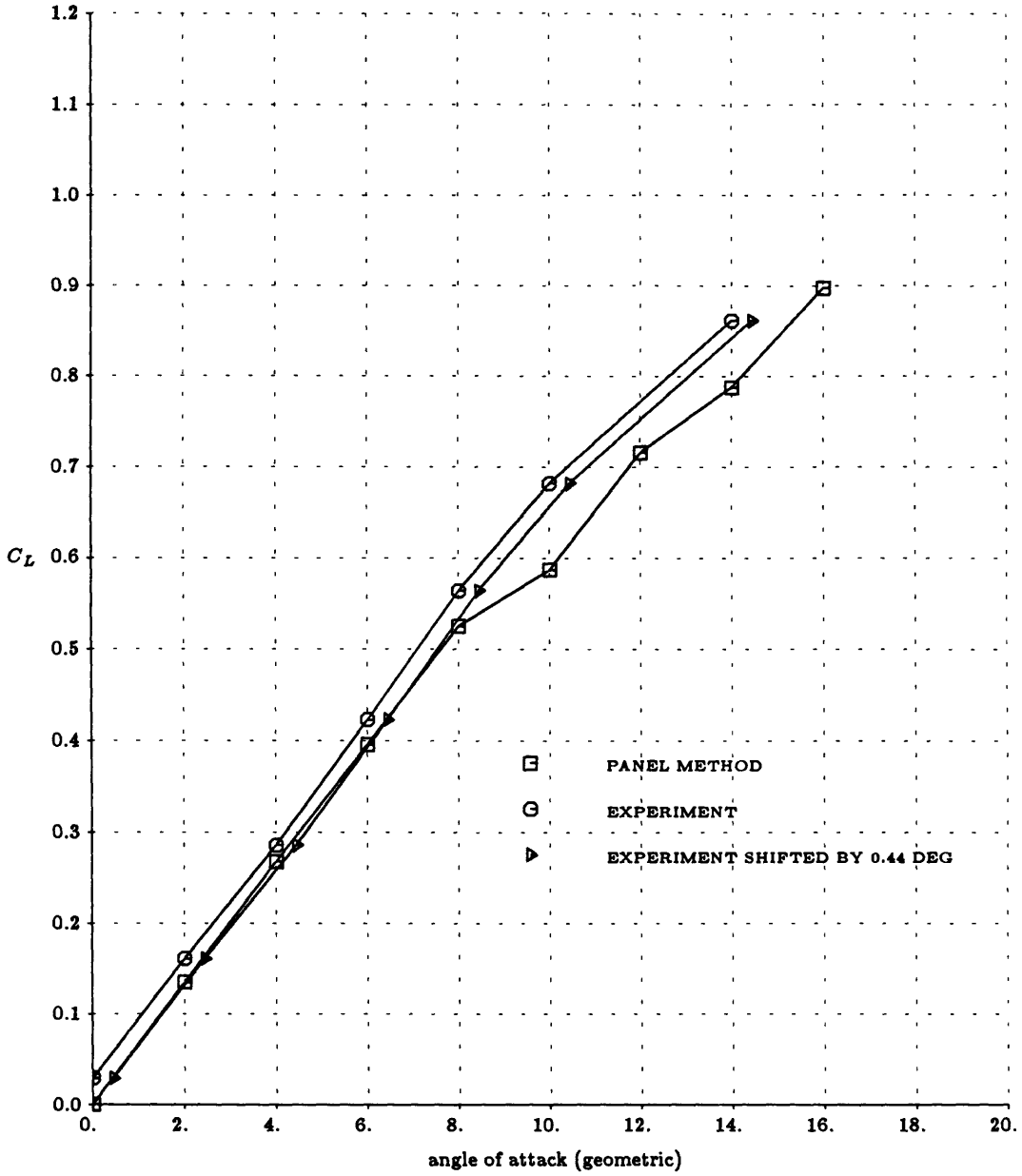

Figure 4.13: Experiment and panel method - C_L vs. α (b/B=0.73)

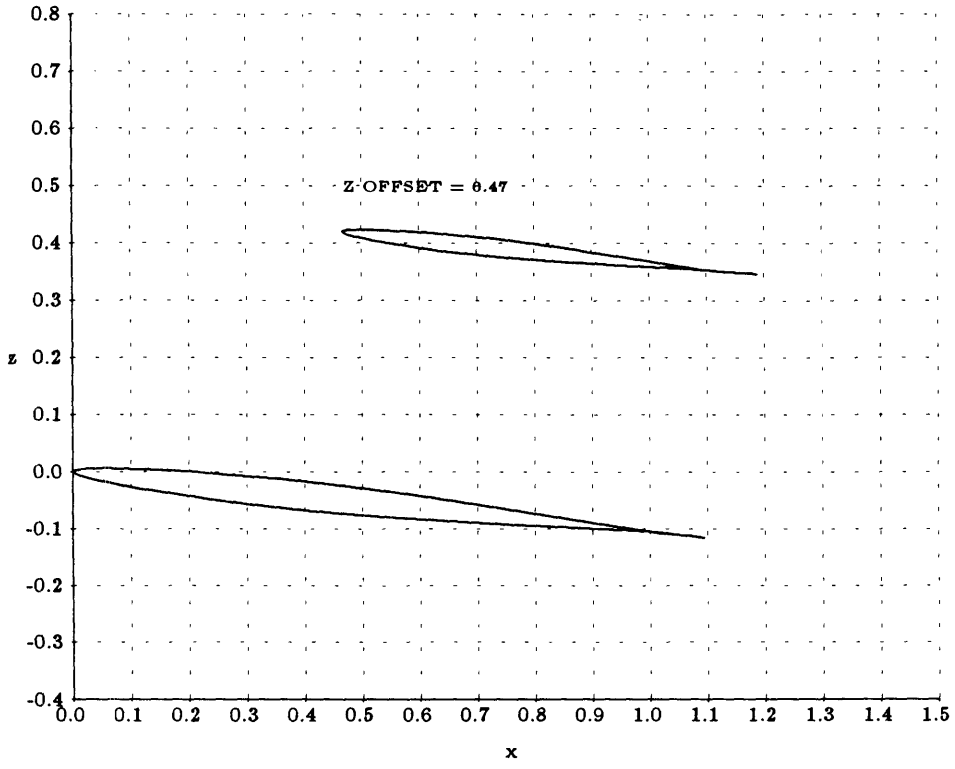

Figure 4.14: Wing and wake shape for $\alpha = 6$ deg, in tunnel (b/B=0.73)

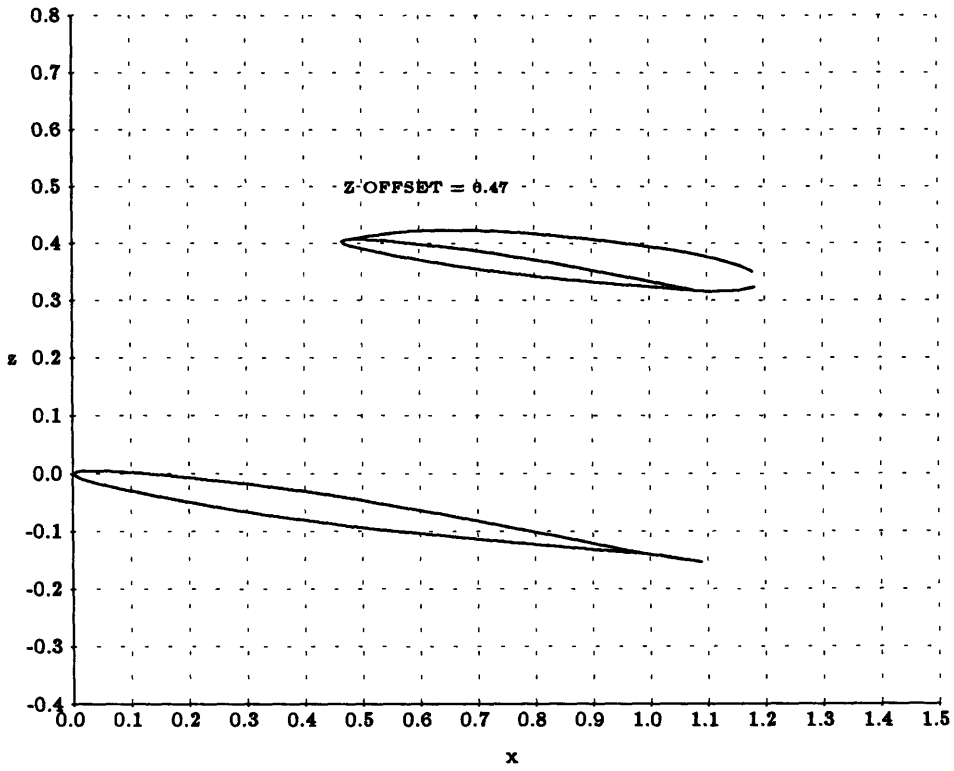

Figure 4.15: Wing and wake shape for $\alpha = 8$ deg, in tunnel (b/B=0.73)

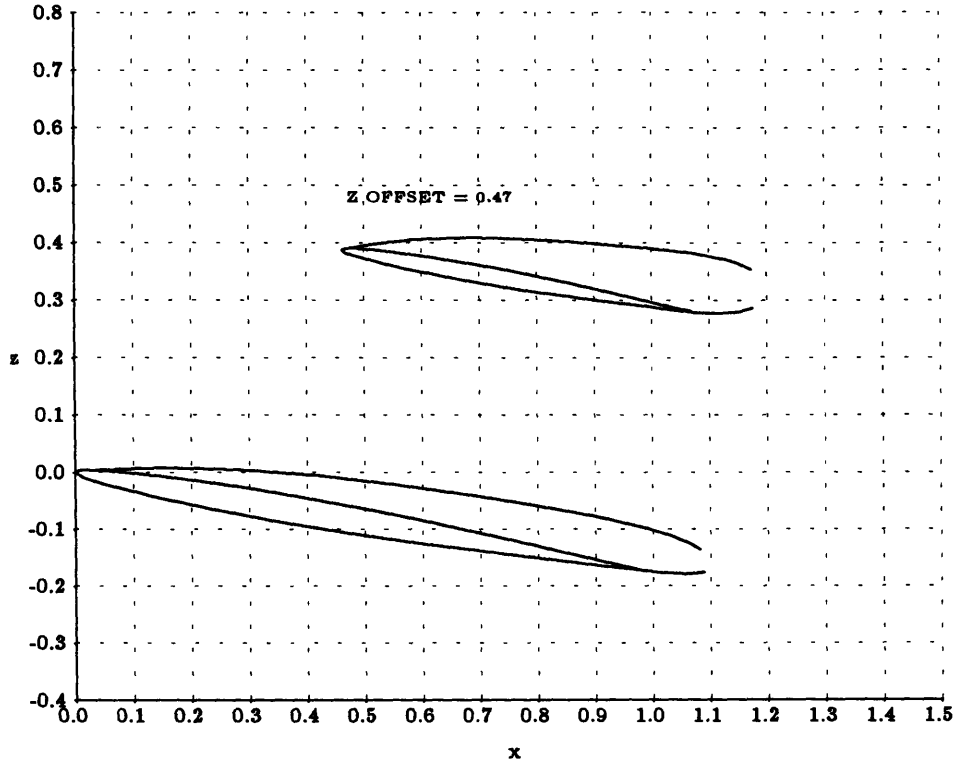

Figure 4.16: Wing and wake shape for $\alpha = 10$ deg, in tunnel (b/B=0.73)

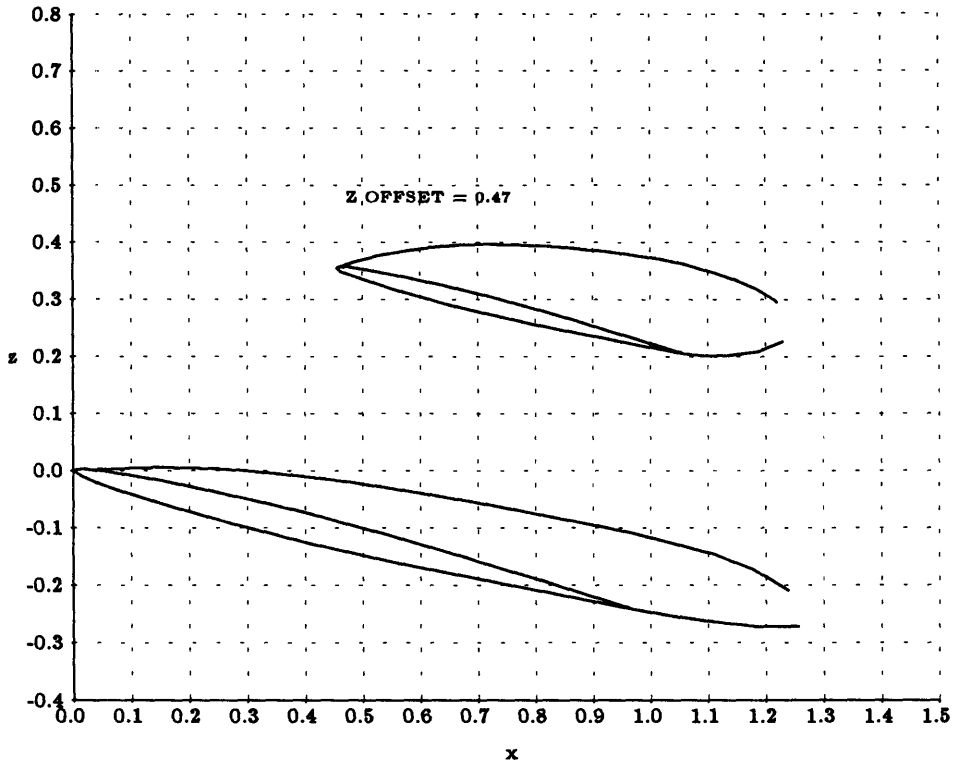

Figure 4.17: Wing and wake shape for $\alpha = 14$ deg, in tunnel (b/B=0.73)

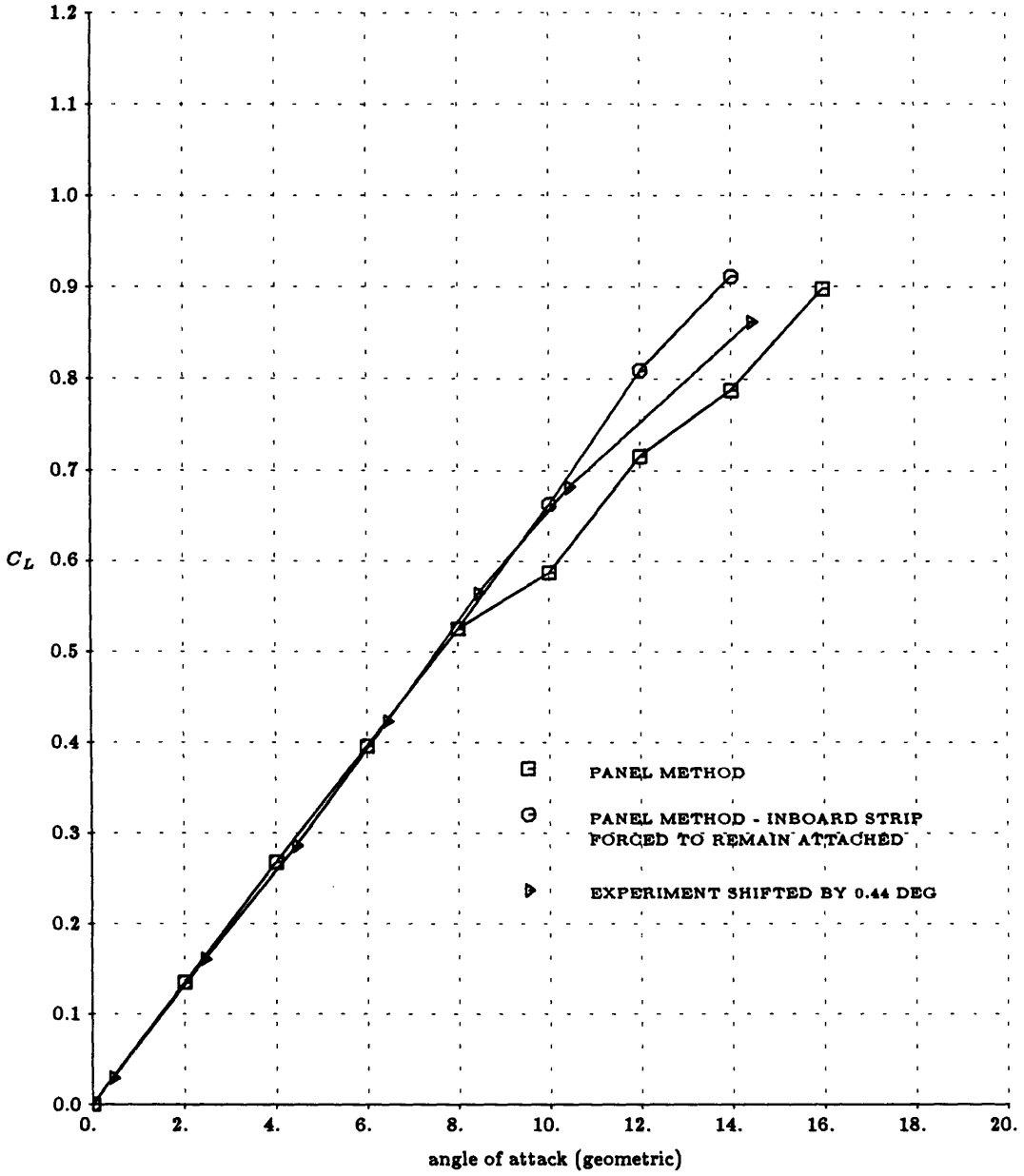

Figure 4.18: Experiment and panel method - C_L vs. α (b/B=0.73)

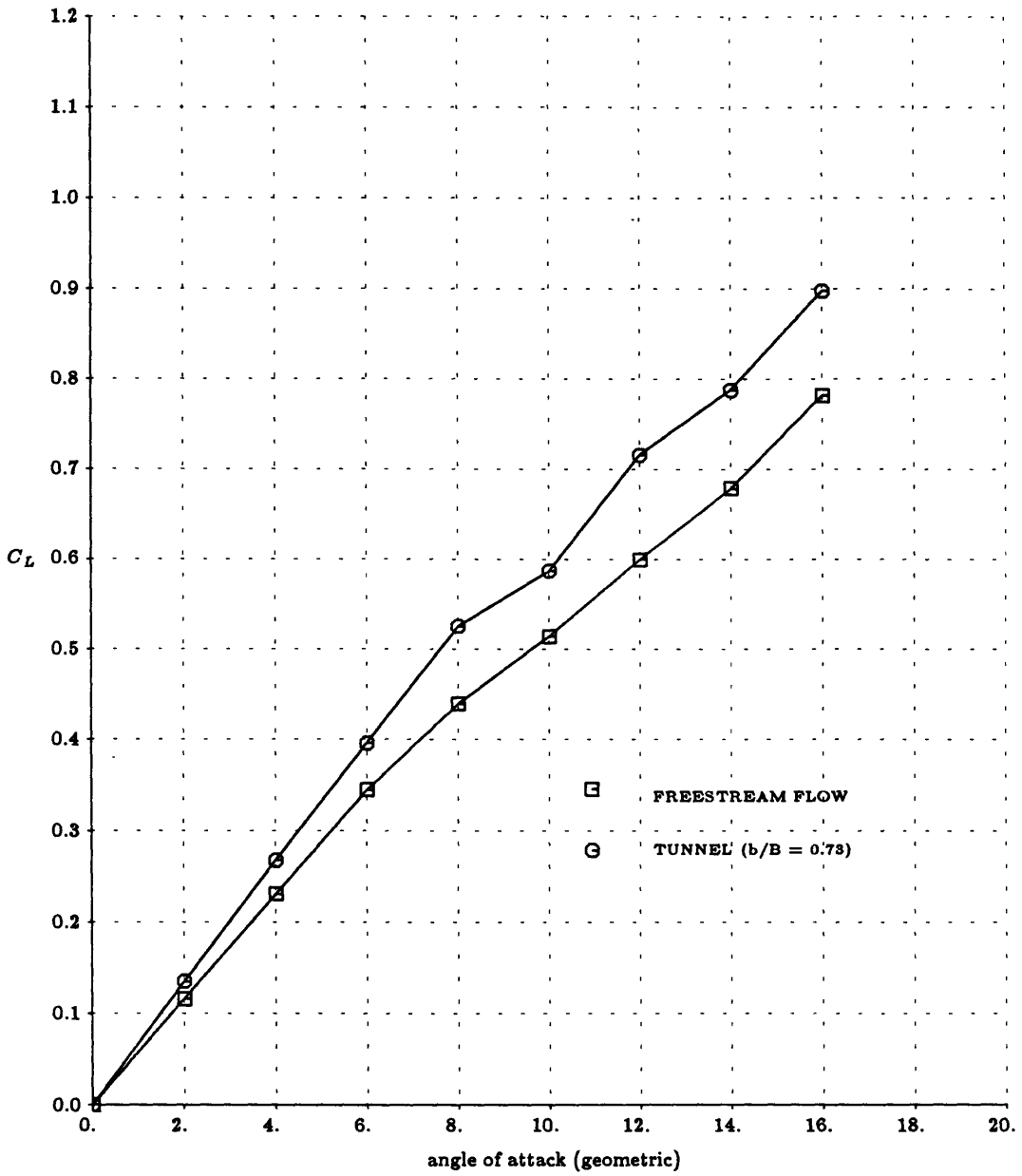

Figure 4.19: Free air and tunnel(b/B=0.73) - C_L vs. angle of attack

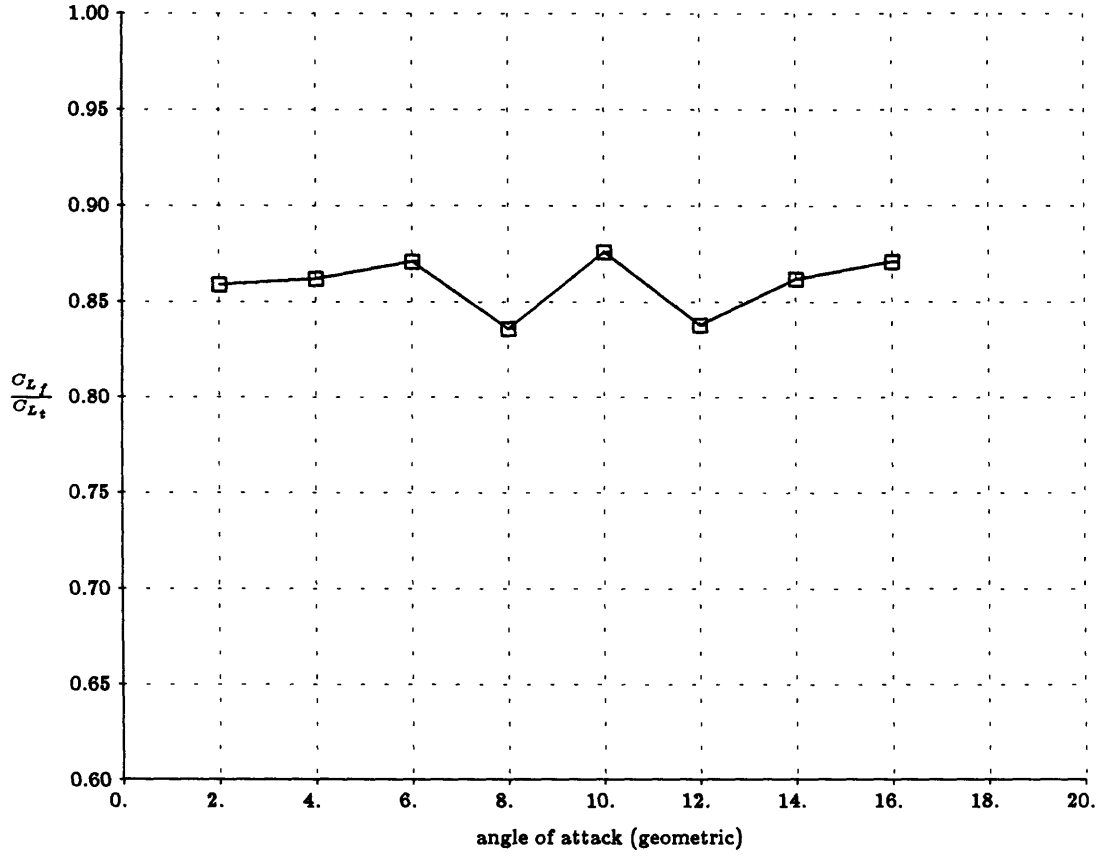

Figure 4.20: C_{L_f}/C_{L_t} vs. angle of attack (b/B=0.73)

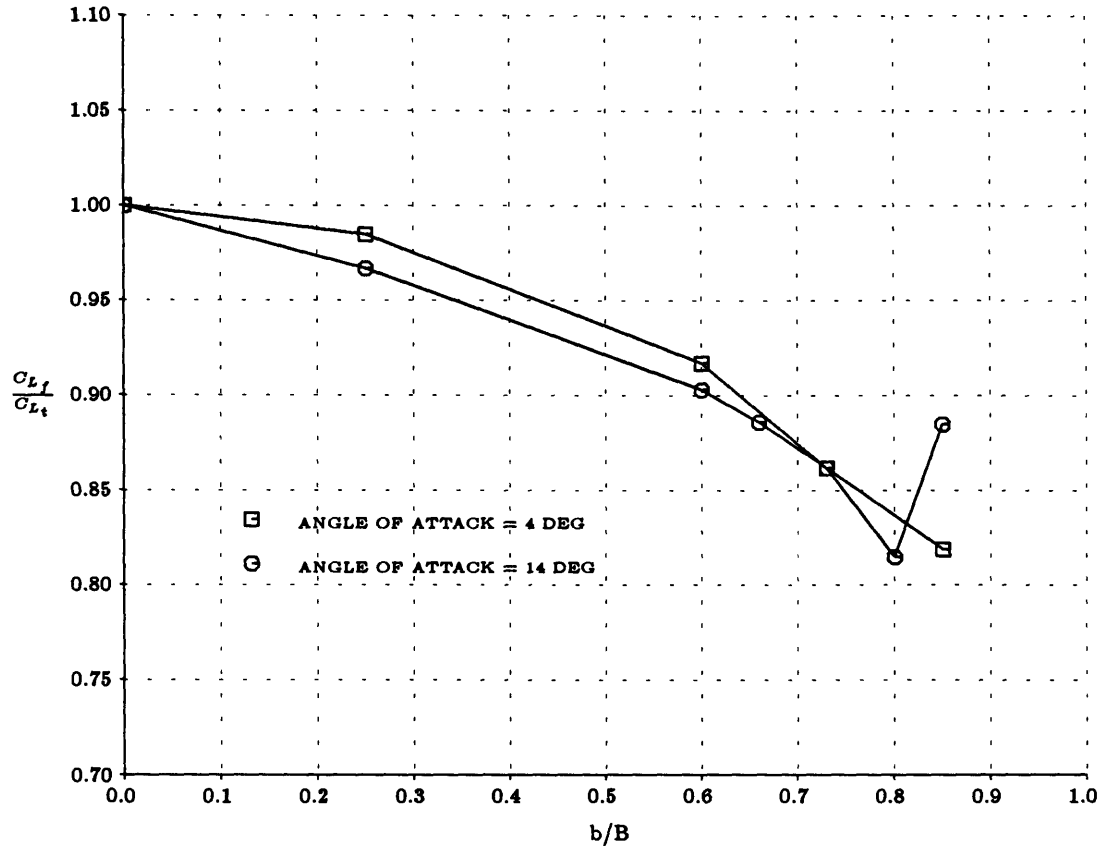

Figure 4.21: C_{L_f}/C_{L_t} vs. b/B, $\alpha = 4$ and 14 deg.

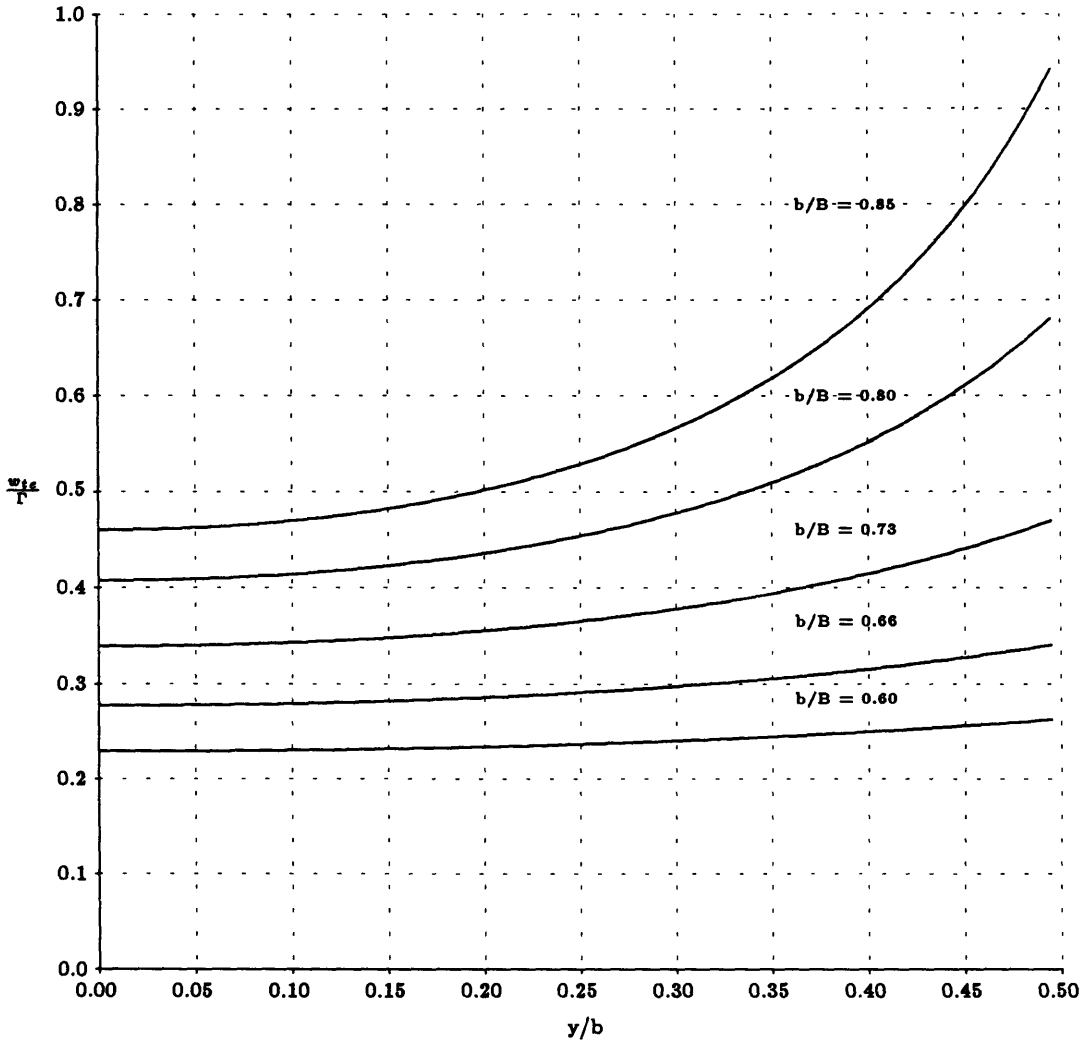

Figure 4.22: Classical wall correction, w_t/Γ vs. b/B